Dynamical correlations and order in magic-angle twisted bilayer graphene

Gautam Rai,[1, *] Lorenzo Crippa,[2, *] Dumitru Călugăru,[3] Haoyu Hu,[4] Luca de' Medici,[5] Antoine Georges,[6, 7, 8] B. Andrei Bernevig,[3, 4, 9] Roser Valentí,[10] Giorgio Sangiovanni,[2, †] and Tim Wehling[1, 11, ‡]

[1] *I. Institute of Theoretical Physics, University of Hamburg, Notkestrasse 9, 22607 Hamburg, Germany*
[2] *Institut für Theoretische Physik und Astrophysik and Würzburg-Dresden Cluster of Excellence ct.qmat,*
Universität Würzburg, 97074 Würzburg, Germany
[3] *Department of Physics, Princeton University, Princeton, New Jersey 08544, USA*
[4] *Donostia International Physics Center, P. Manuel de Lardizabal 4, 20018 Donostia-San Sebastian, Spain*
[5] *LPEM, ESPCI Paris, PSL Research University,*
CNRS, Sorbonne Université, 75005 Paris France
[6] *Center for Computational Quantum Physics, Flatiron Institute, 162 Fifth Avenue, New York, NY 10010, USA*
[7] *Collége de France, 11 Place Marcelin Berthelot, 75005 Paris, France*
[8] *PHT, CNRS, École Polytechnique, IP Paris, F-91128 Palaiseau, France*
[9] *IKERBASQUE, Basque Foundation for Science, Bilbao, Spain*
[10] *Institut für Theoretische Physik, Goethe Universität Frankfurt,*
Max-von-Laue-Strasse 1, 60438 Frankfurt am Main, Germany
[11] *The Hamburg Centre for Ultrafast Imaging, 22761 Hamburg, Germany*
(Dated: September 18, 2023)

The interplay of dynamical correlations and electronic ordering is pivotal in shaping phase diagrams of correlated quantum materials. In magic angle twisted bilayer graphene, transport, thermodynamic and spectroscopic experiments pinpoint at a competition between distinct low-energy states with and without electronic order, as well as a competition between localized and delocalized charge carriers. In this study, we utilize Dynamical Mean Field Theory (DMFT) on the topological heavy Fermion (THF) model of twisted bilayer graphene to investigate the emergence of electronic correlations and long-range order in the absence of strain. We explain the nature of emergent insulating and correlated metallic states, as well as transitions between them driven by three central phenomena: (i) the formation of local spin and valley isospin moments around 100K, (ii) the ordering of the local isospin moments around 10K, and (iii) a cascadic redistribution of charge between localized and delocalized electronic states upon doping. At integer fillings, we find that low energy spectral weight is depleted in the symmetric phase, while we find insulating states with gaps enhanced by exchange coupling in the zero-strain ordered phases. Doping away from integer filling results in distinct metallic states: a "bad metal" above the ordering temperature, where coherence of the low-energy electronic excitations is suppressed by scattering off the disordered local moments, and a "good metal" in the ordered states with coherence of quasiparticles facilitated by isospin order. Upon doping, there is charge transfer between the localized and delocalized orbitals of the THF model such that they get periodically filled and emptied in between integer fillings. This charge reshuffling manifests itself in cascades of doping-induced Lifshitz transitions, local spectral weight redistributions and periodic variations of the electronic compressibility ranging from nearly incompressible to negative. Our findings highlight the essential role of charge transfer, hybridization and ordering in shaping the electronic excitations and thermodynamic properties in twisted bilayer graphene and provide a unified understanding of the most puzzling aspects of scanning tunneling spectroscopy, transport, and compressibility experiments.

I. INTRODUCTION

When two layers of graphene are stacked on top of each other with a relative twist angle of 1.1 degrees (the magic angle), the emergent long-wavelength moiré pattern gives rise to a band structure with extremely flat bands at the charge neutrality point [1–3]. Electronic interaction effects are enhanced in the flat bands, leading to a rich low-temperature phase diagram where superconducting [4–7], insulating [8], correlated metallic [9, 10], and exotic

magnetic phases [5, 11–15] have been observed in experiment by manipulating the charge carrier density. There has been a large theoretical effort towards understanding the insulating [16–74] and superconducting [17–22, 75–102] phases, ferromagnetism [46, 69–72, 103, 104], the topological properties [101, 105–114], and on constructing suitable models [3, 16, 109, 111, 115–136]. Simultaneously, there has been extensive experimental work [137–164]. For integer fillings, static mean-field approaches such as Hartree-Fock [16, 37, 38, 55, 57, 58, 61] revealed a number of candidate ordered states related by the approximate symmetries of the system that are very close in energy. Depending on filling and the strain and relaxation properties of the sample, these include the time-reversal symmetry breaking Kramer's intervalley coherent (K-IVC) state, valley-polarized states

(VP) [16] and incommensurate Kekulé spiral (IKS) states [27, 58, 61] accompanied by a time-reversal symmetry preserving inter-valley coherent (T-IVC) order. The near-degeneracy of the ordered states suggests that the true state is sample-dependent owing to perturbations such as substrate effects, defects, and most importantly strain, in line with recent experiments [165, 166].

While the static mean-field approach is suitable for studying the integer-filled case deep in the ordered regime, understanding fractional doping and the transition to the symmetric state, made up of disordered fluctuating local moments, requires a dynamic treatment of local correlations. A suitable many-body method for this is dynamical mean-field theory (DMFT) [167, 168]. Previous applications of DMFT have successfully investigated the symmetric phase using the Wannier-construction–based multi-orbital projector models [169, 170] and the topological heavy Fermion model [171], shedding light on Kondo physics and Fermi-surface resetting cascade transitions [142]. These studies focused on fully symmetric states. Therefore, the interplay between dynamic correlations and spontaneous symmetry-breaking remains an outstanding question that needs to be addressed.

In this paper, we apply DMFT on a set of symmetry-broken states of unstrained magic-angle twisted bilayer graphene (TBLG)—treating static and dynamic effects on the same footing, and compare the resulting spectral and thermodynamic observables with calculations in the symmetric state. In the symmetric (or interchangeably disordered) state we explicitly suppress long-range order. Our calculations provide a unified understanding of scanning tunneling spectroscopy [142] and compressibility experiments [149, 150, 172, 173], and some puzzling aspects of transport [137, 150, 174] experiments based on three effects: (i) the formation of local isospin moments around 100 K, (ii) a cascadic charge reshuffling between localized and delocalized electronic states, and (iii) the ordering of local isospin moments around 10K.

At integer fillings in the symmetric state, there is hybridization-induced depletion of spectral weight at the Fermi level. In the zero-strain ordered state, there is a hard gap, and the spectral functions are comparable to Hartree-Fock calculations [16]. We find ordering temperatures of ∼15K at $\nu = 0, -1$, and ∼10K at $\nu = -2$ (where ν measures the number of charge carriers per moiré unit cell with respect to the charge neutrality point). These ordering temperatures are about an order of magnitude lower than the Hartree-Fock prediction, indicating strong suppression of long-range order by local dynamic fluctuations, and the existence of a local moment regime spanning a wide temperature range. We further extend our symmetry-broken calculations to fractional fillings. At small doping away from the insulator, we find a doping-induced insulator-to-metal transition involving the population of coherent light charge carriers. We characterize the Fermi surface across a range of fillings, and find that the topology, the orbital character, and the coherence of the Fermi surface depends on the filling, and the absence

or presence of long-range order. We identify the changes in the Fermi surface with a sequence of Lifshitz transitions associated with a redistribution of charge between localized and delocalized orbitals. These Lifshitz transitions manifest themselves as the filling-induced cascade transitions seen in compressibility [149, 150, 173, 175] and spectroscopic measurements [142].

Entropy and transport measurements have observed the isospin Pomeranchuk effect in TBLG [137, 149, 150, 174], in a phenomenological analogy to helium-3 [176]. The Pomeranchuk effect has previously been discussed in the solid state context in the Hubbard model [177, 178], and in cold atoms [179]. At certain fillings, raising the temperature induces a transition from a metallic state (resistivity $\approx 10^{-1}$ kΩ) to a near-insulating state (resistivity $\approx 10^{1}$ kΩ) at around 5–10 K [150, 174]. Our approach allows us to distinguish between two distinct metallic states in TBLG—an order-induced coherent good metal below the DMFT ordering temperature, and an incoherent bad metal. Our results therefore point to a microscopic mechanism underlying the observations of "Pomeranchuk physics" in transport and thermodynamics experiments, with good agreement of the temperature scale.

The doping dependencies of the electronic spectra and the existence of disordered moments at temperatures above ∼10 K is closely linked to the dependence of the chemical potential μ on doping ν in the symmetric phase. Our calculations unveil a balancing mechanism between the filling of the correlated and uncorrelated subspaces, by which the former is progressively occupied with increasing total filling, and the latter is cyclically filled and depleted. We discuss the correlated nature of the system at integer and fractional fillings, showing how, coherently with what is known about the physics of the periodic Anderson model, Mott-like behavior emerges at integer values of the *total* filling. We compare our DMFT results with the exact solution of the topological heavy Fermion model [16] (see also Sec. II) in the zero-hybridization limit [180] and explain the observed features in the experimentally measurable *charge compressibility*. This is found to exhibit a saw-tooth behavior and negative values in extended ranges of dopings, once the geometrical capacitance contribution is subtracted out analogously to experiments [181–183].

II. MODEL

We use the topological heavy Fermion (THF) model from Ref. [16] to describe the electronic structure of TBLG. This model, derived from the microscopic interacting Bistritzer-MacDonald model [3], connects a set of completely localized f-orbitals to highly dispersive c-orbitals that carry the topology. Per spin and valley ($s \in \{\uparrow, \downarrow\}$, $\eta \in \{+, -\}$ respectively), there are two f-orbitals ($\alpha \in \{1, 2\}$), and four c-orbitals (two of each forming the Γ_3 ($a \in \{1, 2\}$) and $\Gamma_1 \oplus \Gamma_2$ ($a \in \{3, 4\}$) rep-
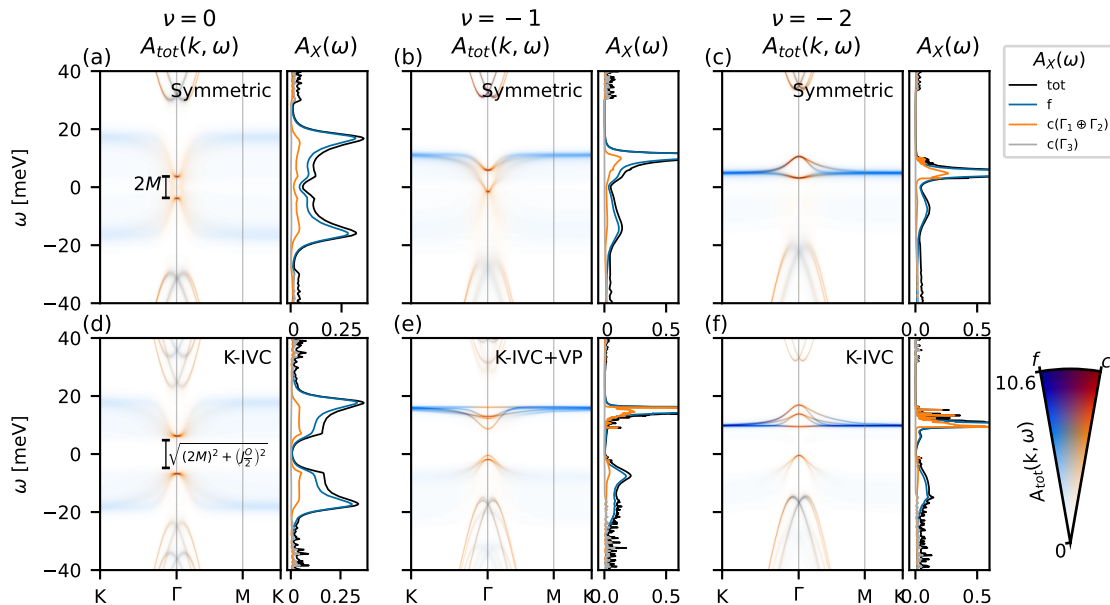
FIG. 1. The momentum-resolved $A(k, \omega)$ and momentum-integrated $A(\omega)$ spectral functions at integer filling in the symmetric (top panels) and symmetry-broken phases (bottom panels) at the fillings $\nu = 0, -1, -2$ (from left to right). In the color plot for $A_{tot}(k, w)$, the hue represents the orbital character (blue for f vs red for c) of the spectral weight. The different lines in the $A(\omega)$ plot denote total ($X = $ tot) or orbital-projected ($X = f, c(\ldots)$) spectral functions. The data is at 7.7 K.

resentations). The f-orbitals make up most of the flat bands; the exception is at the Γ point in the moiré Brillouin zone, where the flat band character changes to that of the $\Gamma_1 \oplus \Gamma_2$ c-orbitals through f-c hybridization. The THF Hamiltonian can be written as

$$\hat{H}_{THF} = \underbrace{\hat{H}_c + \hat{H}_{cf}}_{\hat{H}_0} + \hat{H}_U + \hat{H}_W + \hat{H}_V + \hat{H}_J. \quad (1)$$

The terms comprising the non-interacting Hamiltonian $\hat{H}_0$ are $\hat{H}_c$, which contains the dispersion of the c-orbitals, and $\hat{H}_{cf}$, which contains the hybridization between the two subspaces. $\hat{H}_0$ defines two important energy scales: the splitting of the $\Gamma_1 \oplus \Gamma_2$ c-subspace, $M = 3.7$ meV, which sets the bandwidth of the flat bands, and the f-c hybridization term at Γ, $\gamma = -24.8$ meV, which sets the gap between the flat bands and the high-energy bands. The four terms in the interacting part of the Hamiltonian are $\hat{H}_U$ ($\hat{H}_V$), the density-density interaction in the $f(c)$-subspace, $\hat{H}_W$, the density-density interaction between c- and f-states, and $\hat{H}_J$, the exchange interaction between the f- and c-subspaces. See App. B or [16] for the definition of each term. In our calculation, we treat $\hat{H}_U$ with DMFT, taking its local many-body effects into account, and the remaining interaction terms via static mean-field decoupling. We perform two sets of calculations: (a) allowing for symmetry-broken states where symmetry-breaking in the first iteration is guided by Hartree-Fock results from [16]; (b) in a fully symmetric state. For later convenience, we define n_f, n_c, and $n = n_f + n_c$ to be the number of f-, c-, and total electrons per moiré unit cell

in the system. The corresponding fillings with respect to the charge neutrality point are given by $\nu_f = n_f - 4$, $\nu_c = n_c - 8$, and $\nu = n - 12$. Due to the exact particle-hole symmetry of the THF model (which may be broken by additional terms not included in this study), the physics at positive and negative ν is related by a particle-hole transformation, and we will limit our discussions to $\nu \leq 0$. In this paper, isospin refers to a generalized spin consisting of electron spin, valley, and orbital degrees of freedom. The corresponding local moments are referred to interchangeably as isospin moments, local moments, and local isospin moments.

III. METHODS

We split the total Hamiltonian into a static and a dynamic part,

$$\hat{H}_{stat} = \hat{H}_c + \hat{H}_{fc} + \hat{H}_W^{MF} + \hat{H}_V^{MF} + \hat{H}_J^{MF} \\ - 3.5U \sum_{\alpha\eta\sigma} f^\dagger_{\alpha\eta\sigma} f_{\alpha\eta\sigma}, \quad (2)$$

$$\hat{H}_{dyn} = \frac{U}{2} \sum_{(\alpha\eta\sigma) \neq (\alpha'\eta'\sigma')} f^\dagger_{\alpha\eta\sigma} f_{\alpha\eta\sigma} f^\dagger_{\alpha'\eta'\sigma'} f_{\alpha'\eta'\sigma'}. \quad (3)$$

The superscript MF represents a static mean-field decoupled interaction term (Hartree+Fock for $\hat{H}_W^{MF}$ and $\hat{H}_J^{MF}$ and Hartree for $\hat{H}_V^{MF}$).

$\hat{H}_{stat}$ plays the role of the lattice Hamiltonian in the DMFT calculation. It must be self-consistently deter-

mined as the mean-field decoupled interaction terms depend on the system's density matrix ρ. $\hat{H}_{dyn}$ acts on the f-subspace only and induces a frequency-dependent self-energy in the f-subspace. We solve the impurity problem with two continuous-time quantum Monte Carlo (CT-QMC) hybridization expansion solvers (TRIQS-cthyb [184–186] and w2dynamics [187, 188]). We converge two self-consistency loops at once: the DMFT self-consistency condition for the self-energy Σ of the f-subspace, and the Hartree-Fock mean-field condition for the total density matrix ρ. Details of the calculations as well as the CT-QMC parameters are given in App. C.

The results shown in this paper are obtained for the lowest energy ordered phases predicted by a Hartree-Fock analysis [16] of the THF model in the absence of strain. That is, at the charge neutrality point ($\nu = 0$), both spin sectors are half-filled with K-IVC order, upon hole doping once ($\nu = -1$), one spin sector is K-IVC ordered, while the other spin sector is valley polarized, and at half-filling ($\nu = -2$), one spin sector has K-IVC order, while the other has no long-range order. We emphasize that these states and their flat- and chiral-$U(4)$ related counterparts valley-polarized (VP), and intervalley-coherent (T-IVC) states are very close in energy. The true ordered state is therefore sensitive to defects, substrate effects, strain, and other sample-dependent perturbations. These effects can be incorporated with DMFT on the THF model with additional terms, and will be the subject of a future publication. Our goal is to make universal statements about the interplay of correlations and ordering in this system, which likely does not depend on which of the several competing low-temperature ordered phases the system is in.

For the symmetry-broken calculations at integer fillings, we bias the system towards the chosen symmetry-broken solution by applying a weak polarizing field for the first few DMFT iterations, and then turning it off for the remainder until self-consistency is reached. (See Appendix D for the definition of the polarizing field). In the ordered phase, we approach fractional fillings around each integer filling by gradually doping the integer-filling self-consistent solution in small increments.

IV. RESULTS

A. (Nearly) insulating states at integer filling

Fig. 1 shows the DMFT spectral functions in the symmetric and the symmetry-broken phases at integer fillings $\nu = 0, -1, -2$. In all cases, the local Hubbard term in $\hat{H}_{dyn}$ shifts the flat-band spectral weight of the f-subspace away from the Fermi level to form lower and upper Hubbard bands. The remaining low-energy excitations have residual f- and $\Gamma_1 \oplus \Gamma_2$ c-orbital character, while the Γ_3 c-spectral weight remains pushed away to higher energies ($\sim \gamma = 24$ meV) by the f-c hybridization term. We point out two generic differences between the spectral functions in the symmetric ((a)-(c))
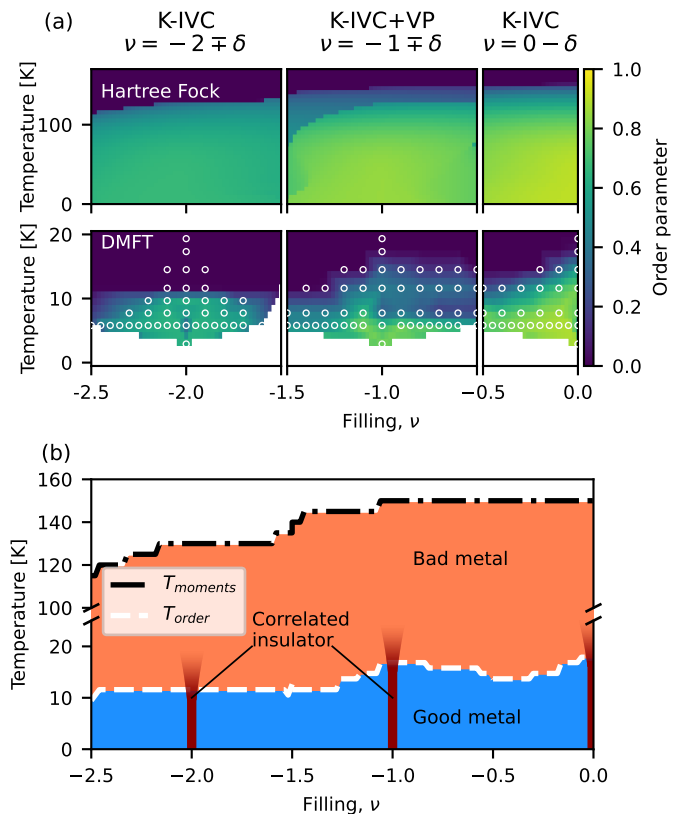

FIG. 2. (a) The magnitude of the symmetry-breaking order parameter at various fillings and temperatures. In the bottom panel, white circles represent numerical data points from DMFT simulations at and around the $\nu = -2$ (K-IVC), $\nu = -1$ (K-IVC+VP), and $\nu = 0$ (K-IVC) parent states in the left, middle, and right panels respectively. The space between circles is filled by linear interpolation. The top panel shows the same quantity from a Hartree-Fock simulation (note the different vertical scale). In the dark blue regions, the self-consistency loop flows to the symmetric state, indicating that the symmetry-broken solution does not exist. (b) A schematic filling-temperature phase diagram: local moments form below the Hartree-Fock ordering temperature (T_{moments}) in the orange region. These local moments order below the DMFT ordering temperature (T_{order}) in the blue region. The DMFT ordering temperature marks the boundary between a bad metal and a (order-facilitated) good metal at fractional fillings as discussed in Sec. IV E and Sec. IV G in the main text. The correlated insulators at integer fillings emerging below T_{order} (dark red) fades into the bad metal above T_{order} forming regions with most strongly suppressed quasiparticle weights, c.f. Fig. 5b).

and symmetry-broken ((d)-(f)) phases. First, the Hubbard bands are relatively sharp in the symmetry- broken phase compared to those in the symmetric phase, indicating that dynamic correlations are weaker in the symmetry-broken phases [189]. Second, while low-energy spectral weight is depleted also in the symmetric state, symmetry-breaking supports a robust insulating gap in

the absence of strain. This is best seen comparing the momentum-integrated spectral functions in the right panels of Fig. 1(a) and (d). In the symmetric case, spectral weight is reduced at the Fermi level but does not vanish. In the ordered case, the spectral weight vanishes and there is a robust gap. This can be understood in the language of the THF model. At the Γ point, the bare (with f-c hybridization turned off) dispersion of the THF model has two contributions at zero energy: per spin and valley, there is a pair of f-orbitals with completely flat bands at zero, and a pair of Γ_3 c-orbitals that contribute a pair of particle-hole related parabolic bands touching at zero. f-c hybridization moves both of these contributions away from zero to the high-energy bands at the Γ point. Precisely at the Γ point, the flat bands are entirely of $\Gamma_1 \oplus \Gamma_2$ c-character. Generically, the c-electron spectral weight is affected by interactions in the f-sector directly by the f-c exchange interaction (H_J), and indirectly through hybridization effects. The former directly gaps out the c-electron spectral weight near the Fermi level. This is evident in the energy difference between the bright spots in the spectral functions at the Γ point at the charge neutrality point (CNP) in Fig. 1(a) and Fig. 1(d). In the symmetric phase (a), the $\Gamma_1 \oplus \Gamma_2$ c-orbitals retain the $2M$ splitting of the non-interacting Hamiltonian. In the symmetry-broken case (d), the splitting gains an additional contribution from the f-c exchange term $\hat{H}_J$ and is given by $\sqrt{(2M)^2 + (OJ/2)^2}$, where O is the off-diagonal inter-valley term in the f-subspace density matrix.

What is the nature of the (nearly) insulating states at integer fillings? Given the close relation between the THF and the periodic Anderson model (PAM), we attempt a classification of insulating states of the THF model in terms of the phenomenology of the periodic Anderson model. In the PAM, different types of insulators including band insulators, Kondo insulators, Mott insulators, and charge transfer insulators have been established [190, 191].

At integer ν_f, the limit of $U \to \infty$ corresponds to removing all f-states from the THF Hamiltonian. However, without c-f coupling (and thus also without f-states at all) the THF model is metallic [16] and not gapped. Clearly, the absence of a gap at $U \to \infty$ in the symmetric state, rules out TBLG at integer filling being a genuine Mott insulator, in agreement with the interpretations of [169, 170]. At the experimentally relevant temperatures of a few K, a Kondo insulator at integer fillings is unlikely, since the f-electron moments are not yet fully screened down to $\sim$1 K [171].

The absence of a hard Mott gap can be traced back to a finite t_{fc} in our THF model, similarly to what has been discussed in Ref. [192]: even at strong interaction strengths, as long as the f-electrons can hop into a noninteracting band crossing the Fermi level, a Mott insulator with a clean gap is prevented. The heavy Fermi-liquid that replaces it has typically a very low coherence temperature. In accordance with these general expectations (and despite the differences between our model and those of Ref. [192]) we find (see section IV G) that the quasiparticle weight never vanishes in the symmetric state, even close to integer fillings where it is heavily suppressed, displaying the commensurability effects characteristic of incipient Mott phases. Still, in order to see a clean gap, long-range ordering is needed, as we find in our calculations for broken-symmetry states.

The presence of f- and c- spectral weight near the Fermi level is reminiscent of "p-metals" [191] or charge transfer (CT) insulators [190]. In typical transition metal oxide-based CT insulators like NiO or cuprates [190], the electronic gap is bounded by transition metal $3d$ and oxygen $2p$-spectral weight from above and below, respectively. The insulating states at $\nu = -2$ with dominantly c-spectral weight below the Fermi level and f-spectral weight above (c.f. Figs. 1 (c) and (f)) resemble this CT scenario. Also the insulating states $\nu = 0$ and $\nu = -1$ are similar to CT insulators, yet with one decisive difference to the usual CT and p-metal case: in TBLG at $\nu = 0$ and $\nu = -1$ we have delocalized c-bands dispersing in between the f-type Hubbard bands from above *and* below. Also differently from the transition metal oxide CT cases, the spectral depletion regions near the Fermi level of TBLG in the symmetric state rely on hybridization between delocalized (c) and localized (f) states. In the ordered states of TBLG, it is the exchange interaction between c and f orbitals leading to mass terms [180] which markedly enhance the gaps in the c-sector and thus also the total gaps.

B. Fluctuations and the stability of the ordered solution

Next, we study how doping or raising the temperature affects the ordered states at integer fillings. Fig. 2(a) shows the order parameter of the self-consistent solution in a doping-temperature plane generated by gradually doping a particular ordered state at an integer filling. We define the order parameter in the symmetry-broken phase at arbitrary filling by the matrix inner product with the traceless part of the corresponding parent state density matrix (see Appendix D). At high enough temperatures, the system flows to the disordered phase under the self-consistency loop. We find the threshold temperature to be $\sim$15 K at $\nu = 0, -1$, and $\sim$10 K at $\nu = -2$. The ordering temperature predicted by Hartree-Fock is an order of magnitude higher ($\sim$100-150 K; see upper panel of Fig. 2(a)). Our DMFT simulations show that long-range order is suppressed by local dynamic fluctuations down to about 10 K. Spatial fluctuations are expected to reduce the ordering temperature further. Just below the DMFT ordering temperature, doping away from an integer solution also leads to a disordered solution, resulting in dome-shaped ordered regions as seen in the lower panel of Fig. 2(a). At low enough temperatures, the ordered solution continued from either neighboring integer filling

may co-exist at a given fractional filling.

We interpret the Hartree-Fock ordering temperatures as the point at which local moments start to form. Anticipating the results of Sec. IV C and Sec. IV E, where we discuss the metallic states below and above the ordering temperature, we construct a schematic phase diagram in Fig. 2(b). Below the ordering temperature of $\sim$10 K, we find an insulator at integer fillings, and a good metal at fractional fillings. The state above the ordering temperature is discussed in Sec. IV E, where we will show that the spectral weight at the Fermi level is generically incoherent, indicating a bad metal. Our results point to a *coherence from order* at low temperatures, which we expand on in Sec. IV F.

C. Doping-induced insulator-to-metal transition

Away from integer filling, the normal state of TBLG is metallic. The nature of the metallic state depends on the filling and temperature. In fact, we find distinct behaviors upon doping with electron or holes away from the insulators at $\nu = 0$ or $\nu = -1$ on one hand and $\nu = -2$ on the other hand. In Fig. 3(a), we show how the spectral function changes as we slightly dope the system away from $\nu = -1$ at $T = 5.8$ K in the ordered state with electrons or holes. In this case, we find that the Fermi level moves into the dispersive part of the low-energy bands around the Γ point: the active bands are coherent with delocalized c-character. Here, we expect Fermi liquid-like behavior. Metallic behavior derived from c-orbitals on both sides of the insulator points back to the peculiar property of the charge-transfer insulator at $\nu = -1$ with c-bands dispersing both above and below. In contrast, the behavior at $\nu = -2$ is asymmetric with respect to doping. Consider the spectral function in Fig. 1 (f). The c-part of the upper band is flattened. While hole doping at $\nu = -2$ would lead to metallic behavior just like at $\nu = -1$, electron doping would start to immediately occupy the f-orbitals. This is much more reminiscent of a conventional charge transfer insulator, with localized carriers on one side and delocalized carriers on the other side of the gap.

Upon further doping away from $\nu = -1$ towards $\nu = 0$, the Fermi level eventually also hits the localized f-part of the flat bands. This occurs generically once between every two successive integer fillings, and is shown in Fig. 3(b) for $\nu = -0.6$. The supplementary material includes a movie showing the evolution of the spectral function as the filling is varied (https://youtu.be/cw3K0YEsPU0). The ordered phase (in the left panel) has a splitting in the f-subspace that is absent in the symmetric phase (in the right panel). This is a consequence of a feedback of the ferromagnetic exchange interaction $\hat{H}_J$, which is only active in the ordered phase. Due to the isospin order in the f-sector, $\hat{H}_J$ behaves like a polarizing field in the c-sector, inducing analogous isospin order in the c-sector. The induced isospin order in the

c-sector in turn causes a small polarizing field in the f-sector, resulting in the splitting seen in the left panel of Fig. 3(b).

In both the symmetric and ordered state, hitting the localized f part of the spectrum induces a charge reshuffling between the localized and delocalized subspaces, resulting in the sawtooth pattern of orbital-resolved filling seen in [171, 180, 193]. This is precisely the region of fillings where experiments see negative compressibilities [150, 175]. We discuss the orbital-resolved fillings along with the compressibility further in Sec. IV H. These filling regions are also associated with a sequence of Lifshitz transitions. We identify these Lifshitz transitions with the experimentally observed cascade transitions [142, 175] in Sec. IV E.

D. Cascade transitions and signatures of order

In Fig. 4(a), we show the momentum-integrated spectral function as a function of filling in the symmetric and symmetry-broken phases. In both cases, there is a reconstruction of the low-energy spectral features upon changing the doping by an integer value. These are the *cascade transitions* that have been seen experimentally with scanning tunnel spectroscopy (STS) [11, 142] and which have been similarly found in the DMFT study of Datta et al. [170] for the symmetric state. In the symmetric state, at integer fillings, the spectral function has a two-peak structure, with a lower and an upper peak that are similarly far away from zero, but with their relative spectral weight depending on which integer filling the system is tuned to (for instance, compare $\nu = -2$ and $\nu = -1$ in Fig. 4). Upon hole doping away from an integer filling, the two peak structure shifts to higher energies, the lower peak merges with a zero-energy resonance, and the upper peak fades away. Upon further hole doping, as the system approaches the next integer filling, the zero energy resonance shifts to higher energies becoming the new upper peak, and a new lower peak emerges.

The symmetry-broken state behaves the same way except that there is fine low-energy structure, owing to isospin order. The details of the fine structure will depend on the particular ordered state. In particular, the zero-energy peak at fractional fillings, made up primarily of f-spectral weight, is split by a feedback effect from the exchange interaction $\hat{H}_J$. This splitting is present as long as there is isospin order. See Fig. 2 for the sets of filling and temperature values where this fine structure may be present. Note that our calculation does not include spatial fluctuations, which might further suppress ordering temperatures.
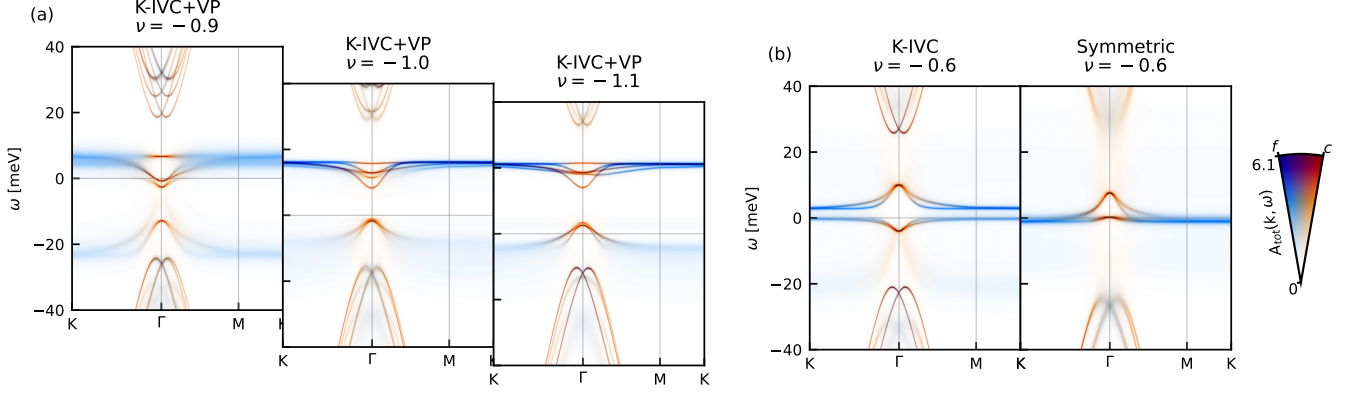
FIG. 3. Spectral functions at 5.8 K (a) at and close to $\nu = -1$ in the ordered phase (b) at $\nu = -0.6$ in the ordered and symmetric phases. In (a), the electron and hole doped panels are shifted such that the Hubbard bands match up with the middle panel. Lightly doping away from an integer-filled insulator moves the Fermi level into the coherent c-spectral weight around the Γ-point leading to a coherent metal. Upon further doping as in (b), the Fermi level hits the f-part of the flat bands, leading to coherent and incoherent spectral weight at the Fermi level.

E. Fermiology and Lifshitz transitions

We perform a quasiparticle analysis at the Fermi level to better understand the Fermi surface reconstruction and the Lifshitz transitions underlying the cascades. The exact shape of the Fermi surface will depend on perturbations such as strain, but some general features such as the existence and loose integer-periodic nature of the Lifshitz transitions will remain. We numerically find the zeros, $\hat{H}_{qp}(k)\left|\psi^i(k)\right\rangle = 0$, of the quasiparticle Hamiltonian

$$\hat{H}_{qp}(k) = \hat{Z}^{\frac{1}{2}}\mathfrak{Re}\left[G^{-1}(\omega + i\epsilon, k)\right]_{\omega \to 0}\hat{Z}^{\frac{1}{2}}, \qquad (4)$$

where $\hat{Z} = \left(1 - \partial_{i\omega}\mathfrak{Im}\hat{\Sigma}_{tot}(i\omega)\Big|_{i\omega \to 0}\right)^{-1}$ is the matrix quasiparticle weight. $\hat{\Sigma}_{tot}$ is the f-subspace self-energy promoted to the full $f \oplus c$ space by padding with zeros in the c-sector (the c-sector is treated on a mean-field level and the static contribution to the self-energy is included in the mean-field terms in $\hat{H}_{stat}$), the superscript i on $\left|\psi^i(k)\right\rangle$ labels the zeros in case there is degeneracy at any k-point. The zeros of $\hat{H}_{qp}$ point at potential quasiparticles at the Fermi level. In particular, the quasiparticle weight $\hat{Z}$ evaluated at the zeros gives information on the coherence of spectral weight at the Fermi level in the form of a k-dependent quasiparticle weight

$$\frac{1}{Z^i(k)} = \left\langle\psi^i(k)\right|\hat{Z}^{-1}\left|\psi^i(k)\right\rangle \qquad (5)$$

along a potential Fermi contour. For an uncorrelated Fermi liquid, $Z^i(k) = 1$, and $\left|\psi^i(k)\right\rangle$ would give the quasiparticle eigenstates at the Fermi surface. Technical details on the root-finding algorithm used to find $\left|\psi^i(k)\right\rangle$ and the rest of the quasiparticle analysis are provided in Appendix F.

The blue lines in Fig. 4(b)-(f), which we henceforth refer to as zero energy lines (ZEL), mark the location of

the zeros $\left|\psi^i(k)\right\rangle$ in k-space overlaid on the spectral function at the Fermi level in the first moiré Brillouin zone at select fillings. For clarity, the symmetric phase data in Fig. 4(b)-(d) projected to the K-valley only. The K' valley contribution is related by a C_2 rotation. We find that the topology of the ZEL changes with doping. In our zero-strain calculation, between the CNP and $\nu = -1$, we see three regimes. Upon lightly doping away from CNP, (b), The K-projected ZEL consists of two concentric contours. The three lobes of the outer contour jutting away from the Γ point have low quasiparticle weight, and correspondingly smeared out spectral weight. The inner ring and the inner sections of the outer ring are primarily of c-character and more coherent, and form a Fermi contour. Halfway to $\nu = -1$ (c), the Fermi level hits the flat f-part of the flat band (see also Fig. 3(b)). This coincides with the concentric ZEL connecting to form a trefoil knot. This ZEL has three points where it intersects itself corresponding to potential van Hove singularities at the Fermi level. As in the previous case, however, the outer lobes of the ZEL have low quasiparticle weight and are primarily f-character. Finally, approaching $\nu = -1$, the ZEL consists of a single closed contour, as seen in (d). We reiterate that the other valley contributes additional 60 degree rotated copies of these Fermi surfaces restoring C_6 symmetry.

In the ordered case Fig. 4(e)-(g), the zeros are not valley-decoupled as the charge carriers occupy intervalley coherent orbitals. The color map therefore shows the full spectral weight with both valleys included. Generically, away from integer fillings, the zeros are coherent with high quasiparticle weight. The symmetry and topology of the Fermi surface depends on the properties of the active orbital at the chosen filling. Doping with holes away from CNP, the Fermi surface consists of K-IVC orbitals getting depleted, resulting in a Fermi surface that is 6-fold symmetric. Near $\nu = -1$, there are
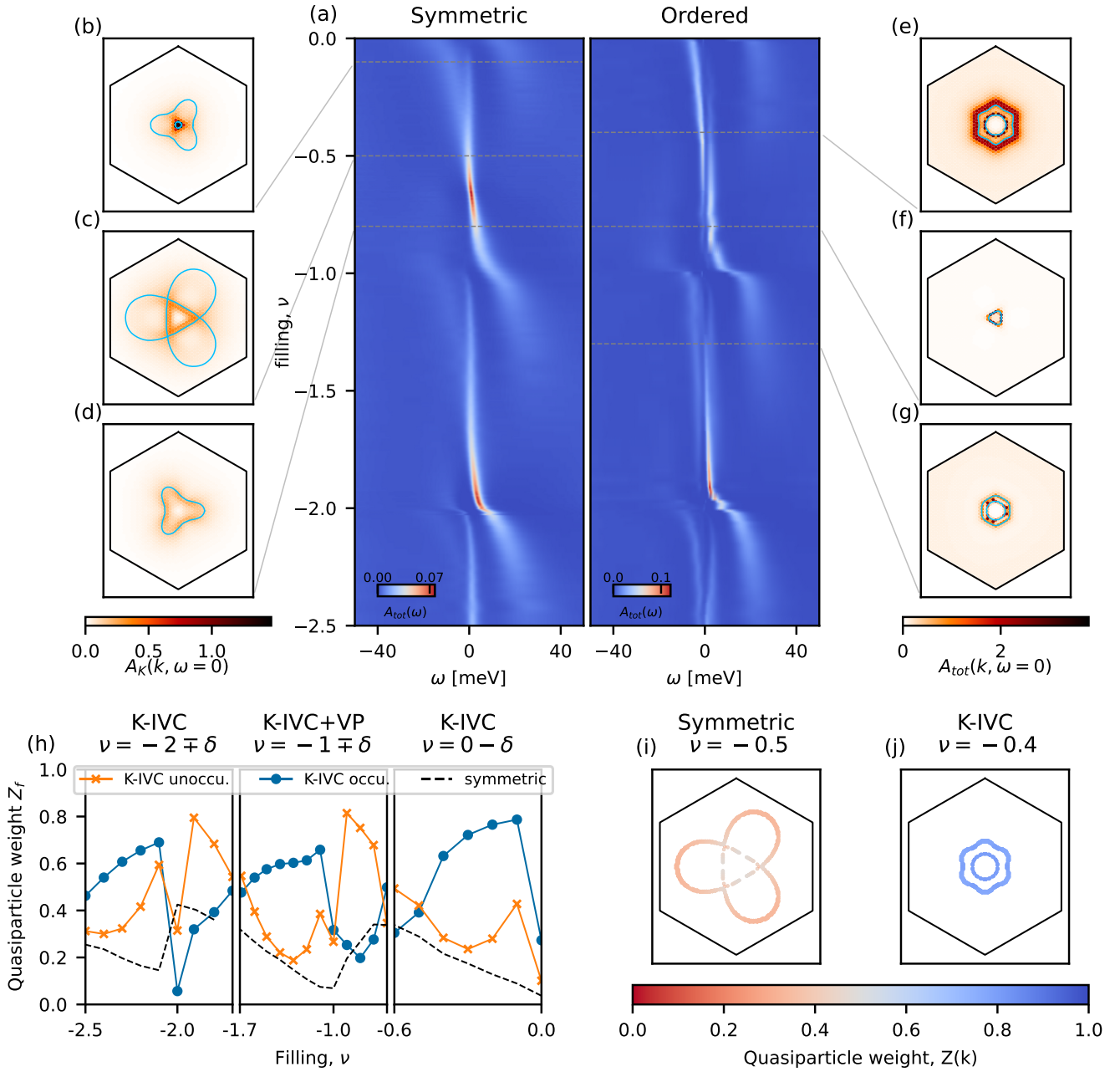
FIG. 4. (a) The momentum-integrated spectral function $A_{tot}(\omega)$ at 11.6 K in the symmetric phase (left) and 5.8 K in the ordered phase (right) as a function of hole doping. The electron-doped side (with respect to CNP) is related to the hole-doped side by a partice-hole transformation. (b)-(d) The K-valley–projected zero-energy spectral function in the first moiré Brillouin zone in the symmetric phase at select fillings. (e)-(g) The full zero-energy spectral function in the first moiré Brillouin zone in the ordered state at select fillings. The light blue lines mark the zeros of the effective Hamiltonian as identified by a quasiparticle analysis (see main text). (h) A comparison of the f-orbital quasiparticle weight Z_f in the symmetric and ordered states. In the ordered case, only the spin-up K-IVC occupied and unoccupied orbitals are shown for clarity. (i)-(j) The quasiparticle weight projected onto the quasiparticle basis along the zeros of the quasiparticle hamiltonian.

two occupied K-IVC orbitals in one spin sector, and an occupied valley-polarized orbital in the other spin sector. Electron (hole) doping corresponds to occupying (depleting) the unoccupied (occupied) valley-polarized orbital, resulting in a Fermi surface that is 3-fold symmetric. We

emphasize that perturbations such as strain will change the details of the ordered state and the shape and symmetries of the Fermi surface. However, there will still be Lifshitz transitions between integer fillings when the Fermi level hits the incoherent f-band.

F. Pomeranchuk physics and coherence from order

An important takeaway from Fig. 4 is the different nature of the metallic state in the symmetric and ordered phases. Generically, the spectral weight at the Fermi level in the ordered state originates from much more coherent excitations than in the disordered state. This can be seen from Fig. 4(h), where we show the quasiparticle weight in the orbital basis over a range of fillings, and from Fig. 4(i)-(j), where we show the quasiparticle weight in the quasiparticle basis $Z(k)$ from Eq. (5) at chosen fillings. Thus, generically at fractional fillings, we expect a good metal in the ordered state, and a bad metal in the disordered state. With an ordering temperature of about 10–15 K, this interpretation is consistent with transport experiments [137, 174], which observe a sharp drop in resistivity at temperatures below 5–10 K for a range of fillings around the correlated insulating phases. With this analysis, we are able to provide a microscopic explanation for the isospin Pomeranchuk effect in TBLG. The bad metal at high temperatures is the result of an incoherent metal stabilized by the isospin entropy of preformed local moments, in analogy to solid helium-3 in the original Pomeranchuk effect [176]. The low-temperature Fermi liquid is a coherent metal induced by spontaneous symmetry-breaking. The spectral function in the ordered phase is composed of bands of coherent quasiparticles, which become occupied upon doping away from the insulating states in the close vicinity of integer filling. In this regard, in contrast to the original Pomeranchuk effect, it is coherence facilitated by order that is responsible for the resistivity drop.

Taken together, our DMFT study reveals the following similarities and differences between the Pomeranchuk physics in He-3 and TBLG. In both systems, disordered fluctuating (iso)spin moments give rise to a high-entropy high temperature phase. Both, in He-3 and TBLG, the (iso)spin entropy is suppressed in the low-temperature state. Both, the low-temperature state of TBLG (at non-integer filling) and He-3, can have T-linear Fermi liquid derived contributions to the entropy. Yet, there is a decisive difference between the low-temperature states of TBLG and He-3: In TBLG, the entropy suppression is due to ordering of the (iso)spin moments, while in He-3 realizes a Fermi liquid without long range spin-order. In other words, there are no local moments in He-3 at low T, while the isospin moments still exist in TBLG albeit ordered.

G. Importance of integer total fillings

Fig. 5 reports the filling of the f- and c-orbitals, as a function of the total filling ν. It is instructive to compare the DMFT solution of the full model with hybridized f- and c-orbitals to the solution of the zero-hybridization model from [180]. This is illustrated in Fig. 5(a) where the solid lines refer to the solution with

finite hybridization solved with DMFT and the light circles to the zero-hybridization case. It is clear that the model with hybridization obeys a similar energetic balance to the one without hybridization. The c-orbitals are periodically filled up and emptied, upon increasing ν. In DMFT, this yields the characteristic, albeit smoothened out, sawtooth behavior. These overall trends displayed by ν_f and ν_c are a consequence of the strong correlations due to the f-f-Coulomb terms together with f-c and c-c interactions terms that are present both in the zero-hybridization solution of Ref. [180] and in our DMFT calculation.

There is a further, more fundamental difference between finite and zero hybridization, namely the special role played in the former—and not in the latter—by the integer values of the total filling ν. In the zero hybridization model, $\nu = -3$, $\nu = -2$, $\nu = -1$ and so on, have no special meaning apart from trivially imposing $\nu_c = 0$. On the contrary, the DMFT solution with finite hybridization bears a clear witness of the integer values of the total ν, as evident from Fig. 5(b)-(c). The quasiparticle weight of the f-orbitals displays particularly strong variations approaching integer values of ν. At the same time, the fluctuations of the f-occupation $\langle n_f^2 \rangle - \langle n_f \rangle^2$ are suppressed near integer values of ν, in contrast to the zero-hybridization case, for which this quantity is flat and vanishes. Everywhere apart from the precise fillings at which the cusps in these two quantities occur, the behavior evidenced by these two indicators of the many-body nature of the f-electrons reveals a crucial property of the THF model with its full heavy-light fermion hybridization.

Periodic Anderson models ubiquitously show Mott-like behaviors at integer values of the total filling, rather than at integer fillings of the correlated subspace [191, 194]. This is independent of whether or not Mott insulating phases are fully realized and is to some extent counterintuitive. One may indeed naively think that the strongest propensity to Mottness is present at integer values of ν_f, not of ν. This "commensurability" physics as a function of total filling is obviously possible only when the hybridization puts the correlated and itinerant subspaces in communication and is captured by DMFT. Indeed, there are two main features that render DMFT especially suited to the task at hand: first, being by construction in the thermodynamic limit it is able to treat integer and fractional fillings on an equal footing. Second, DMFT has been proven to be able to solve models possessing degrees of freedom with different correlation strength in the low-energy subspace (as are f- and c-orbitals in our case) taking the charge fluctuations occurring between the two fully into account.

H. Compressibility

In Fig. 6 we show the total, f- and c-fillings as a function of the *intrinsic* chemical potential μ. A discussion
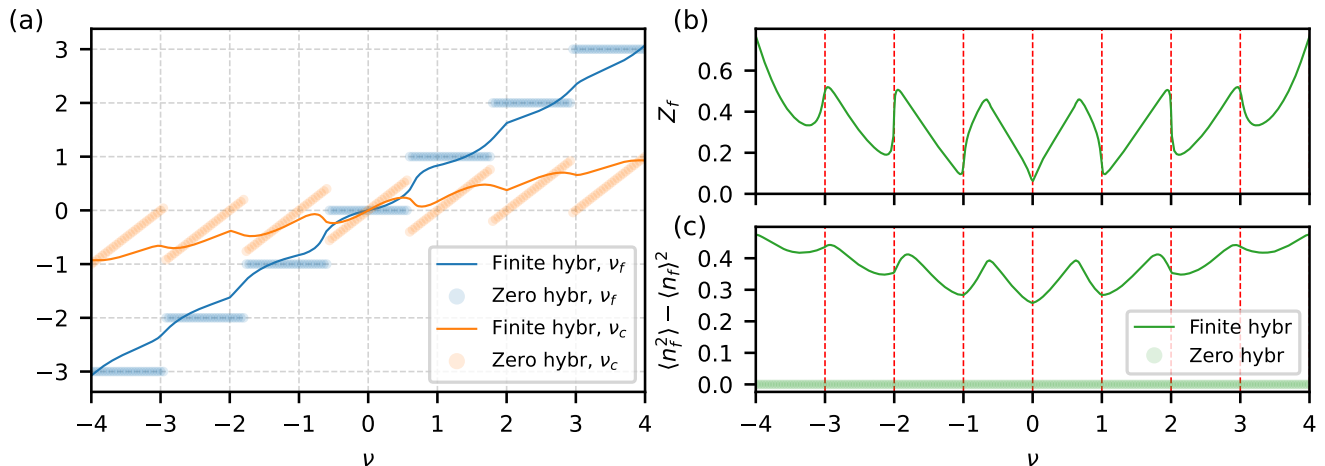
FIG. 5. (a) Partial filling of the f- and c-orbitals as a function of the total filling ν. The dark solid lines show the DMFT results of the full model with hybridization. The light dotted curves are results from the zero-hybridization model solved exactly in [180]. (b) Quasiparticle weight for the f-orbitals, calculated at 11.6 K. (c) Charge fluctuations of the f-orbitals $\langle n_f^2 \rangle - \langle n_f \rangle^2$, as a function of the total filling ν. Both quantities in (b) and (c) are indicators of the importance in DMFT of the integer values of ν, in contrast to the zero-hybridization solution.

on the precise definition of the *intrinsic* chemical potential and on how the mean-field interaction terms are operationally accounted for in our charge self-consistent DMFT calculation can be found in Appendix G; in short, this amounts to separating intrinsic from geometric contributions to the thermodynamic potential [195, 196] and to the chemical potential. What follows uses the *intrinsic* chemical potential μ unless otherwise stated.

The blue solid lines in Fig. 6 report the total and orbital-resolved fillings as a function of μ. These are to be compared with the black dots, which report the same for the zero-hybridization model. In both cases, the overall behavior of the filling is a consequence of an energetic balance between the orbital species. The f-c hybridization constitutes the additional feature captured by our DMFT study with respect to the zero-hybridization case described in [180], and causes a breakdown of the rigid-band picture. The role of the f-c hybridization is to provide a "smoothing" effect on the cross-talk between the two subspaces. Note that, differently from the standard periodic Anderson models considered in literature, the THF model [16] features a specific momentum, and hence real-space, dependence of the hybridization term $H^{fc}(\mathbf{k})$.

The capricious ups and downs of ν_c shown in Fig. 6(c) have to be contrasted to the progressive filling of the uncoupled reservoir of itinerant electrons in the zero-hybridization case: in both cases, when an additional flat f-electron band passes through the Fermi level, it provides a large, rapid increase in occupation, which is compensated by emptying the dispersive c-bands. This behavior is discontinuous in the decoupled case, with ν_c travelling multiple times from ≈ -0.85 to $\approx +0.85$ along the same path marked by the black dots in Fig. 6(c). By

contrast, the presence of f-c hybridization and broadening in the DMFT solution forces both ν_f and ν_c to vary continuously. This results in the behaviors highlighted by the blue curves in Fig. 6(b) and (c) respectively: the f-electron occupation monotonically increases with respect the total ν (see also Fig. 5(a)); when pictured upon varying μ, it shows a series of continuously connected plateaus. These occur trivially at integer values in the zero-hybridization model, while the DMFT solution with hybridization displays plateaux that are not pinned to integer ν_f, except obviously for $\nu_f = 0$ because of particle-hole symmetry. Due to the previously mentioned occupation balancing mechanism, ν_c has instead to necessarily decrease in some intervals upon increasing the total ν, resulting in the peculiar "loops" of Fig. 6(c). A movie showing the evolution of the momentum-resolved spectral function across the filling range is included in the supplementary information (https://youtu.be/cw3K0YEsPU0). It clearly shows the mutual transfer of low-energy spectral weight between f and c.

For comparison to experiments, we extract the electronic compressibility of the model and plot its inverse in Fig. 7(a). One can see how the full resets of μ in the zero-hybridization case result in extremely pronounced negative spikes. In DMFT, these negative regions are much less prominent and the intensity varies between the charge neutrality point and the full/empty fillings. However, the minima of the DMFT data coincide with the negative spikes of the zero-hybridization model, and the positive spikes at integer fillings are consistent between the two methods. While the maxima in the compressibilities found here and by the DMFT study of Datta et al. [170] are in qualitative agreement, there are no neg-
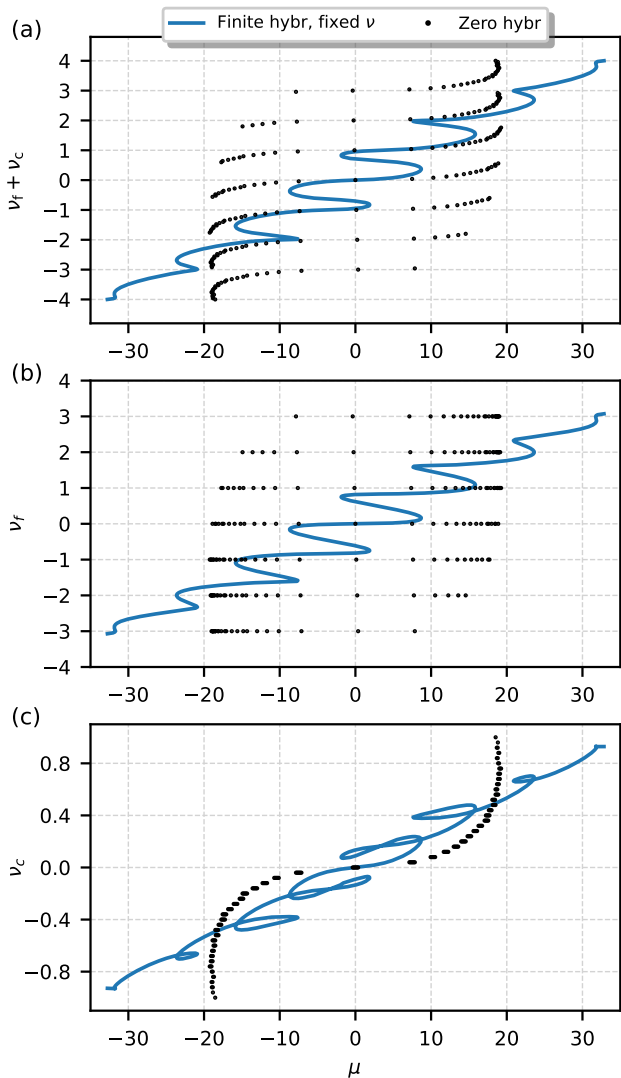
FIG. 6. Filling with respect to CNP as a function of the chemical potential: (a) total filling, (b) f-electron filling, and (c) c-electron filling at T=11.6 K. The solid blue curves refer to DMFT simulations tuning the chemical potential to obtain a target (total) filling. The black dots show results for the zero hybridization model solved in [180].

ative compressibilities reported in Ref. [170]. We assign this discrepancy to geometric capacitance terms, which may not have been fully subtracted in Ref. [170].

The comparison of our DMFT results to experiments, shown in both panels of Fig. 7 reveals an overall reasonable agreement between DMFT and experiments from [150, 173, 175]. Yet, even if DMFT suppresses the negative compressibilities with respect to zero hybridization, these regions are still overestimating the experimentally observed ones (compare the blue to the green, red NS purple curves in Fig. 7). Among the different experimental curves, showing some discrepancies between one another, it is interesting to notice how the position of the

DMFT positive peaks at integer fillings match rather well those of [173], while the negative peaks and the overall behavior of the chemical potential are more similar to that of [175]. Since the THF model is by design particle-hole symmetric it doesn't account for the asymmetries experimentally measured for electron and hole doping. Our results are a better match for positive doping than negative doping. A calculation including strain and additional particle-hole symmetry breaking terms will be the subject of a future study.

I. Significance and origin of the negative compressibilities.

All chemical potential terms discussed so far referred to the intrinsic chemical potential, while only the total thermodynamic potential determines instabilities of the system. The total thermodynamic potential has to include also the geometric contributions, which are present in both, the theoretical model [16] and all experimental realizations of TBLG [142, 149, 150, 175]: the charge required to dope TBLG away from charge neutrality is taken from gate electrodes. The geometric contribution to the total thermodynamic potential is the classical electrostatic energy that builds up upon charge transfer from the gate to TBLG. The intrinsic chemical potential does not involve the contribution from electrostatic potential associated with the charge transfer between gate and TBLG and thus, in turn, a negative compressibility referring only to a derivative involving the *intrinsic* chemical potential $dn/d\mu$ does neither imply necessarily an instability of the system nor a tendency to phase separate.

In the THF model of Ref [16], the TBLG system is supposed to sit in the middle of two gate electrodes, providing an electric potential dependent on the gate separation. As detailed in Appendix G, this entails a large geometric capacitance term, which has to be taken into account when determining the *total* TBLG compressibility. In Fig. G.2 and G.3 of the Appendix we show the same data of Figs. 6 and 7, plotted without the subtraction of the geometrical capacitance contribution, i.e. referring to the *full* TBLG system, which necessarily includes the gates where the doping charges are taken from. There, most of the negative compressibility regions are gone, though a small region survives close to $\nu \pm 0.6$. As detailed in the Appendix, this effect is related to the form of the double-gate screened Coulomb integrals considered in the original THF model, which sets an inter-gate distance $\xi = 10$nm [16]. The geometric contribution depends linearly on the distance between the capacitor plates, which suggests that an interaction term corresponding to a larger separation would have removed even the remaining $\nu \pm 0.6$ negative compressibility region. Similar geometric effects are also ubiquitously present in experimental realizations [142, 149, 150, 175], where TBLG is typically placed in single or multigate structures in order to achieve gate controlled charge doping. In the experi-
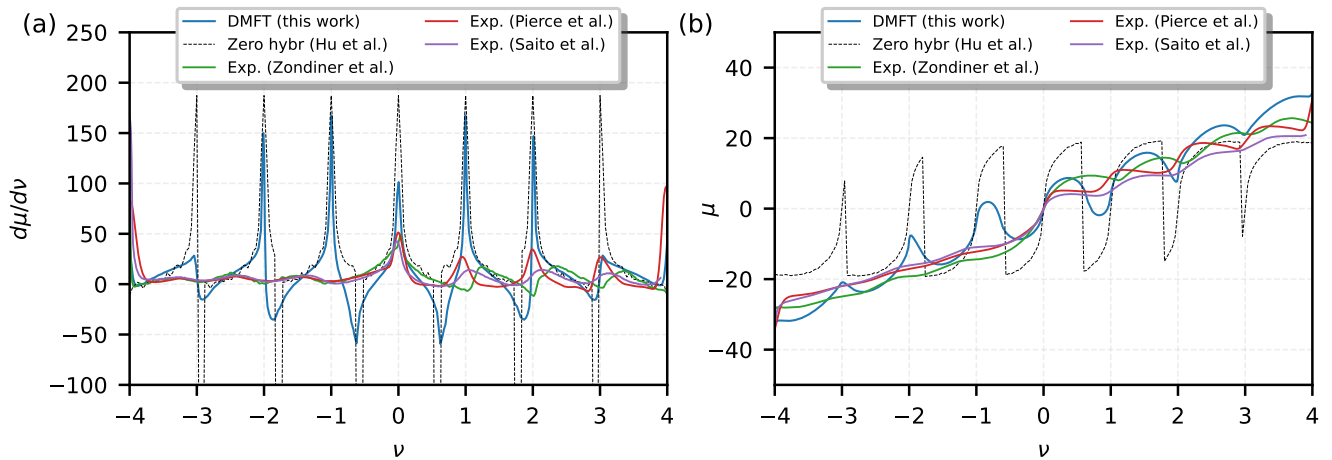
FIG. 7. (a) Inverse compressibility obtained from the fixed-occupation DMFT simulations for $T = 11.6K$, compared with the experimental data from Zondiner et al. [175] ($B_{||} = 0$, $T = 4K$, and $\theta = 1.13°$), Pierce et al. [173] ($B_{||} = 0$, $\theta = 1.06°$), and Saito et al. [150] ($B_{||} = 0$, $T = 12K$ and $\theta = 1.06°$), and the zero-hybridization model from [180]. (b) The chemical potential corresponding to the the inverse compressibilities in (a).

mentally realized setups, assuming the electrodes/back-gate to be ideal metals, which do not feature quantum capacitance effects, the only contribution to the negative compressibility comes from exchange/correlation contributions on the TBLG layer [197], which are accounted for in DMFT locally to all orders.

V. CONCLUSIONS

Our study provides a unified understanding of dynamic correlations and spontaneous symmetry-breaking in TBLG, allowing us to reconcile a set of complementary experiments spanning a wide range of temperatures. Strong electronic interactions in the material give rise to the formation of local isospin moments at temperatures on the order of ~ 100 K, which order around ~ 10 K.

Once the local moments have formed, regardless of whether they order or not, exchange-correlation effects in the localized f-states lead to "integer-periodic" variations in the compressibility ranging from nearly incompressible to negative values as found in capacitance experiments [150, 173, 175]. Concomitantly, there is a periodic redistribution of charge between the f- and the c-states upon doping. This charge reshuffling is responsible for the doping-induced cascade transitions seen in scanning tunneling spectroscopy [142] and explains why the cascades first appear at a temperature of $\sim$100 K [150].

Our study focuses on finite temperatures $T \gtrsim 5$ K and highlights the special role of total integer fillings and the appearence of (nearly) incompressible insulating states there. While there is a hybridization-induced depletion of low-energy spectral weight already in the symmetric phase, exchange interactions generically support a hard gap at integer fillings in the ordered phase in the absence of strain.

Regarding the nature of the metallic states in TBLG, we find disordered local moments which cause scattering and predominantly incoherent low-energy electronic spectral weight in the temperature range of approximately 10 K< T < 100 K. Ordering of the isospin moments leads to coherence and the appearance of well-defined quasiparticles for $T \lesssim 10$ K. This order-induced coherence stands behind the isospin Pomeranchuk effect observed in transport experiments. Above the ordering temperature but below the temperature of moment formation, the isospin entropy of the local moments stabilizes an incoherent "bad metal" phase, which manifests in incoherent spectral weight at the Fermi level. Below the ordering temperature, the Fermi surface is composed of delocalized coherent quasiparticle excitations implying Fermi liquid-like behavior. This change from incoherent to coherent spectral weight at the Fermi level can explain the generic resistivity drop seen in many experiments below ~ 10 K [5, 137, 147, 149, 150]. In contrast to the original Pomeranchuk effect discussed in He-3, suppression of entropy and the coherence in TBLG at low temperatures comes from the ordering of local moments and not from the fate of local moments. The coherence from order physics demonstrated here for TLBG reveals similarities between TBLG and materials such as metallic ferromagnets like $SrRuO_3$ [198] and compounds related to Fe-based superconductors [199].

Our results show that ordering affects electronic spectra and even Fermi surface topologies in metallic states. Thus, we expect that further symmetry-breaking, i.e. particularly superconductivity at lower temperatures $T \sim 1$ K, will be impacted by this order-facilitated coherence.

ACKNOWLEDGMENTS

[1] E. Suárez Morell, J. D. Correa, P. Vargas, M. Pacheco, and Z. Barticevic, Flat bands in slightly twisted bilayer graphene: Tight-binding calculations, Phys. Rev. B **82**, 121407 (2010).

[2] J. M. B. Lopes dos Santos, N. M. R. Peres, and A. H. Castro Neto, Graphene Bilayer with a Twist: Electronic Structure, Phys. Rev. Lett. **99**, 256802 (2007).

[3] R. Bistritzer and A. H. MacDonald, Moiré bands in twisted double-layer graphene, Proceedings of the National Academy of Sciences **108**, 12233 (2011).

[4] Y. Cao, V. Fatemi, S. Fang, K. Watanabe, T. Taniguchi, E. Kaxiras, and P. Jarillo-Herrero, Unconventional superconductivity in magic-angle graphene superlattices, Nature **556**, 43 (2018).

[5] X. Lu, P. Stepanov, W. Yang, M. Xie, M. A. Aamir, I. Das, C. Urgell, K. Watanabe, T. Taniguchi, G. Zhang, A. Bachtold, A. H. MacDonald, and D. K. Efetov, Superconductors, orbital magnets and correlated states in magic-angle bilayer graphene, Nature **574**, 653 (2019).

[6] M. Oh, K. P. Nuckolls, D. Wong, R. L. Lee, X. Liu, K. Watanabe, T. Taniguchi, and A. Yazdani, Evidence for unconventional superconductivity in twisted bilayer graphene, Nature **600**, 240 (2021).

[7] M. Yankowitz, S. Chen, H. Polshyn, Y. Zhang, K. Watanabe, T. Taniguchi, D. Graf, A. F. Young, and C. R. Dean, Tuning superconductivity in twisted bilayer graphene, Science **363**, 1059 (2019).

[8] Y. Cao, V. Fatemi, A. Demir, S. Fang, S. L. Tomarken, J. Y. Luo, J. D. Sanchez-Yamagishi, K. Watanabe, T. Taniguchi, E. Kaxiras, R. C. Ashoori, and P. Jarillo-Herrero, Correlated insulator behaviour at half-filling in magic-angle graphene superlattices, Nature **556**, 80 (2018).

[9] H. Polshyn, M. Yankowitz, S. Chen, Y. Zhang, K. Watanabe, T. Taniguchi, C. R. Dean, and A. F. Young, Large linear-in-temperature resistivity in twisted bilayer graphene, Nature Physics **15**, 1011 (2019).

[10] A. Jaoui, I. Das, G. Di Battista, J. Díez-Mérida, X. Lu, K. Watanabe, T. Taniguchi, H. Ishizuka, L. Levitov, and D. K. Efetov, Quantum critical behaviour in magic-angle twisted bilayer graphene, Nature Physics **18**, 633 (2022).

[11] K. P. Nuckolls, M. Oh, D. Wong, B. Lian, K. Watanabe, T. Taniguchi, B. A. Bernevig, and A. Yazdani, Strongly correlated Chern insulators in magic-angle twisted bilayer graphene, Nature **588**, 610 (2020).

[12] M. Serlin, C. L. Tschirhart, H. Polshyn, Y. Zhang, J. Zhu, K. Watanabe, T. Taniguchi, L. Balents, and A. F. Young, Intrinsic quantized anomalous Hall effect in a moiré heterostructure, Science **367**, 900 (2020).

[13] A. L. Sharpe, E. J. Fox, A. W. Barnard, J. Finney, K. Watanabe, T. Taniguchi, M. A. Kastner, and D. Goldhaber-Gordon, Emergent ferromagnetism near three-quarters filling in twisted bilayer graphene, Science **365**, 605 (2019).

[14] Y. Xie, A. T. Pierce, J. M. Park, D. E. Parker, E. Khalaf, P. Ledwith, Y. Cao, S. H. Lee, S. Chen, P. R. Forrester, K. Watanabe, T. Taniguchi, A. Vishwanath, P. Jarillo-Herrero, and A. Yacoby, Fractional Chern insulators in magic-angle twisted bilayer graphene, Nature **600**, 439 (2021).

[15] G. Chen, A. L. Sharpe, E. J. Fox, Y.-H. Zhang, S. Wang, L. Jiang, B. Lyu, H. Li, K. Watanabe, T. Taniguchi, Z. Shi, T. Senthil, D. Goldhaber-Gordon, Y. Zhang, and F. Wang, Tunable correlated Chern insulator and ferromagnetism in a moiré superlattice, Nature **579**, 56 (2020).

[16] Z.-D. Song and B. A. Bernevig, Magic-Angle Twisted Bilayer Graphene as a Topological Heavy Fermion Problem, Physical Review Letters , 10 (2022).

[17] D. M. Kennes, J. Lischner, and C. Karrasch, Strong correlations and $d+\mathit{id}$ superconductivity in twisted bilayer graphene, Phys. Rev. B **98**, 241407 (2018).

[18] X.-C. Wu, C.-M. Jian, and C. Xu, Coupled-wire description of the correlated physics in twisted bilayer graphene, Phys. Rev. B **99**, 161405 (2019).

[19] T. Huang, L. Zhang, and T. Ma, Antiferromagnetically ordered Mott insulator and d+id superconductivity in twisted bilayer graphene: A quantum Monte Carlo study, Science Bulletin **64**, 310 (2019).

[20] L. Classen, C. Honerkamp, and M. M. Scherer, Competing phases of interacting electrons on triangular lattices in moir\'e heterostructures, Phys. Rev. B **99**, 195120 (2019).

[21] M. Christos, S. Sachdev, and M. S. Scheurer, Superconductivity, correlated insulators, and Wess–Zumino–Witten terms in twisted bilayer graphene, PNAS **117**, 29543 (2020).

[22] Y. Saito, J. Ge, K. Watanabe, T. Taniguchi, and A. F. Young, Independent superconductors and correlated insulators in twisted bilayer graphene, Nat. Phys. **16**, 926 (2020).

[23] A. Thomson, S. Chatterjee, S. Sachdev, and M. S. Scheurer, Triangular antiferromagnetism on the honeycomb lattice of twisted bilayer graphene, Phys. Rev. B **98**, 075109 (2018).

[24] L. Rademaker and P. Mellado, Charge-transfer insulation in twisted bilayer graphene, Phys. Rev. B **98**, 235158 (2018).

[25] M. Ochi, M. Koshino, and K. Kuroki, Possible correlated insulating states in magic-angle twisted bilayer graphene under strongly competing interactions, Phys. Rev. B **98**, 081102 (2018).

[26] B. Padhi, C. Setty, and P. W. Phillips, Doped Twisted Bilayer Graphene near Magic Angles: Proximity to Wigner Crystallization, Not Mott Insulation, Nano Lett. **18**, 6175 (2018).

[27] X. Y. Xu, K. T. Law, and P. A. Lee, Kekul\'e valence bond order in an extended Hubbard model on the honeycomb lattice with possible applications to twisted bilayer graphene, Phys. Rev. B **98**, 121406 (2018).

[28] J. Liu, J. Liu, and X. Dai, Pseudo Landau level representation of twisted bilayer graphene: Band topology and implications on the correlated insulating phase, Phys. Rev. B **99**, 155415 (2019).

[29] L. Rademaker, D. A. Abanin, and P. Mellado, Charge smoothening and band flattening due to Hartree corrections in twisted bilayer graphene, Phys. Rev. B **100**, 205114 (2019).

[30] J. Kang and O. Vafek, Strong Coupling Phases of Par-

tially Filled Twisted Bilayer Graphene Narrow Bands, Physical Review Letters **122**, 246401 (2019).

[31] T. Cea and F. Guinea, Band structure and insulating states driven by Coulomb interaction in twisted bilayer graphene, Phys. Rev. B **102**, 045107 (2020).

[32] E. Khalaf, N. Bultinck, A. Vishwanath, and M. P. Zaletel, Soft modes in magic angle twisted bilayer graphene, arXiv:2009.14827 [cond-mat] (2020), arxiv:2009.14827 [cond-mat].

[33] O. Vafek and J. Kang, Renormalization Group Study of Hidden Symmetry in Twisted Bilayer Graphene with Coulomb Interactions, Phys. Rev. Lett. **125**, 257602 (2020).

[34] P. Eugenio and C. Dag, DMRG study of strongly interacting $\mathbb{Z}_2$ flatbands: A toy model inspired by twisted bilayer graphene, SciPost Physics Core **3**, 015 (2020).

[35] Y. Zhang, K. Jiang, Z. Wang, and F. Zhang, Correlated insulating phases of twisted bilayer graphene at commensurate filling fractions: A Hartree-Fock study, Phys. Rev. B **102**, 035136 (2020).

[36] T. Soejima, D. E. Parker, N. Bultinck, J. Hauschild, and M. P. Zaletel, Efficient simulation of moir\'e materials using the density matrix renormalization group, Phys. Rev. B **102**, 205111 (2020).

[37] N. Bultinck, E. Khalaf, S. Liu, S. Chatterjee, A. Vishwanath, and M. P. Zaletel, Ground State and Hidden Symmetry of Magic-Angle Graphene at Even Integer Filling, Phys. Rev. X **10**, 031034 (2020).

[38] M. Xie and A. H. MacDonald, Nature of the Correlated Insulator States in Twisted Bilayer Graphene, Phys. Rev. Lett. **124**, 097601 (2020).

[39] E. Brillaux, D. Carpentier, A. A. Fedorenko, and L. Savary, Nematic insulator at charge neutrality in twisted bilayer graphene, arXiv:2008.05041 [cond-mat] 10.48550/arXiv.2008.05041 (2020), arxiv:2008.05041 [cond-mat].

[40] J. Kang and O. Vafek, Non-Abelian Dirac node braiding and near-degeneracy of correlated phases at odd integer filling in magic-angle twisted bilayer graphene, Phys. Rev. B **102**, 035161 (2020).

[41] S. Chatterjee, N. Bultinck, and M. P. Zaletel, Symmetry breaking and skyrmionic transport in twisted bilayer graphene, Phys. Rev. B **101**, 165141 (2020).

[42] P. J. Ledwith, G. Tarnopolsky, E. Khalaf, and A. Vishwanath, Fractional Chern insulator states in twisted bilayer graphene: An analytical approach, Phys. Rev. Research **2**, 023237 (2020).

[43] D. V. Chichinadze, L. Classen, and A. V. Chubukov, Valley magnetism, nematicity, and density wave orders in twisted bilayer graphene, Phys. Rev. B **102**, 125120 (2020).

[44] A. Abouelkomsan, Z. Liu, and E. J. Bergholtz, Particle-Hole Duality, Emergent Fermi Liquids, and Fractional Chern Insulators in Moir\'e Flatbands, Phys. Rev. Lett. **124**, 106803 (2020).

[45] D. E. Parker, T. Soejima, J. Hauschild, M. P. Zaletel, and N. Bultinck, Strain-Induced Quantum Phase Transitions in Magic-Angle Graphene, Phys. Rev. Lett. **127**, 027601 (2021).

[46] Y. H. Kwan, G. Wagner, N. Chakraborty, S. H. Simon, and S. A. Parameswaran, Domain wall competition in the Chern insulating regime of twisted bilayer graphene, Physical Review B **104**, 115404 (2021).

[47] Y. H. Kwan, Y. Hu, S. H. Simon, and S. A. Parameswaran, Exciton Band Topology in Spontaneous Quantum Anomalous Hall Insulators: Applications to Twisted Bilayer Graphene, Physical Review Letters **126**, 137601 (2021).

[48] B.-B. Chen, Y. D. Liao, Z. Chen, O. Vafek, J. Kang, W. Li, and Z. Y. Meng, Realization of topological Mott insulator in a twisted bilayer graphene lattice model, Nature Communications **12**, 5480 (2021).

[49] X. Zhang, G. Pan, Y. Zhang, J. Kang, and Z. Y. Meng, Momentum Space Quantum Monte Carlo on Twisted Bilayer Graphene, Chinese Phys. Lett. **38**, 077305 (2021).

[50] J. Kang, B. A. Bernevig, and O. Vafek, Cascades between Light and Heavy Fermions in the Normal State of Magic-Angle Twisted Bilayer Graphene, Phys. Rev. Lett. **127**, 266402 (2021).

[51] A. Kumar, M. Xie, and A. H. MacDonald, Lattice collective modes from a continuum model of magic-angle twisted bilayer graphene, Phys. Rev. B **104**, 035119 (2021).

[52] Y. Da Liao, J. Kang, C. N. Breiø, X. Y. Xu, H.-Q. Wu, B. M. Andersen, R. M. Fernandes, and Z. Y. Meng, Correlation-Induced Insulating Topological Phases at Charge Neutrality in Twisted Bilayer Graphene, Phys. Rev. X **11**, 011014 (2021).

[53] S. Wu, Z. Zhang, K. Watanabe, T. Taniguchi, and E. Y. Andrei, Chern insulators, van Hove singularities and topological flat bands in magic-angle twisted bilayer graphene, Nat. Mater. **20**, 488 (2021).

[54] B. Lian, Z.-D. Song, N. Regnault, D. K. Efetov, A. Yazdani, and B. A. Bernevig, Twisted bilayer graphene. IV. Exact insulator ground states and phase diagram, Phys. Rev. B **103**, 205414 (2021).

[55] J. Liu and X. Dai, Theories for the correlated insulating states and quantum anomalous Hall effect phenomena in twisted bilayer graphene, Phys. Rev. B **103**, 035427 (2021).

[56] F. Xie, A. Cowsik, Z.-D. Song, B. Lian, B. A. Bernevig, and N. Regnault, Twisted bilayer graphene. VI. An exact diagonalization study at nonzero integer filling, Phys. Rev. B **103**, 205416 (2021).

[57] S. Liu, E. Khalaf, J. Y. Lee, and A. Vishwanath, Nematic topological semimetal and insulator in magic-angle bilayer graphene at charge neutrality, Phys. Rev. Research **3**, 013033 (2021).

[58] Y. H. Kwan, G. Wagner, T. Soejima, M. P. Zaletel, S. H. Simon, S. A. Parameswaran, and N. Bultinck, Kekulé Spiral Order at All Nonzero Integer Fillings in Twisted Bilayer Graphene, Physical Review X **11**, 041063 (2021).

[59] J. S. Hofmann, E. Khalaf, A. Vishwanath, E. Berg, and J. Y. Lee, Fermionic Monte Carlo Study of a Realistic Model of Twisted Bilayer Graphene, Phys. Rev. X **12**, 011061 (2022).

[60] F. Xie, J. Kang, B. A. Bernevig, O. Vafek, and N. Regnault, Phase diagram of twisted bilayer graphene at filling factor $\nu=-3$ (2022), arxiv:2209.14322 [cond-mat].

[61] G. Wagner, Y. H. Kwan, N. Bultinck, S. H. Simon, and S. A. Parameswaran, Global Phase Diagram of the Normal State of Twisted Bilayer Graphene, Physical Review Letters **128**, 156401 (2022).

[62] X. Zhang, G. Pan, B.-B. Chen, H. Li, K. Sun, and Z. Y.

Meng, Quantum Monte Carlo sign bounds, topological Mott insulator and thermodynamic transitions in twisted bilayer graphene model (2022), arxiv:2210.11733 [cond-mat].

[63] M. Christos, S. Sachdev, and M. S. Scheurer, Correlated Insulators, Semimetals, and Superconductivity in Twisted Trilayer Graphene, Phys. Rev. X **12**, 021018 (2022).

[64] Y. Da Liao, Z. Y. Meng, and X. Y. Xu, Valence Bond Orders at Charge Neutrality in a Possible Two-Orbital Extended Hubbard Model for Twisted Bilayer Graphene, Phys. Rev. Lett. **123**, 157601 (2019).

[65] P. Cha, A. A. Patel, and E.-A. Kim, Strange Metals from Melting Correlated Insulators in Twisted Bilayer Graphene, Phys. Rev. Lett. **127**, 266601 (2021).

[66] Y. Sheffer and A. Stern, Chiral magic-angle twisted bilayer graphene in a magnetic field: Landau level correspondence, exact wave functions, and fractional Chern insulators, Phys. Rev. B **104**, L121405 (2021).

[67] P. Potasz, M. Xie, and A. H. MacDonald, Exact Diagonalization for Magic-Angle Twisted Bilayer Graphene, Phys. Rev. Lett. **127**, 147203 (2021).

[68] D. Călugăru, N. Regnault, M. Oh, K. P. Nuckolls, D. Wong, R. L. Lee, A. Yazdani, O. Vafek, and B. A. Bernevig, Spectroscopy of Twisted Bilayer Graphene Correlated Insulators, arXiv:2110.1530 (2021), arxiv:2110.1530.

[69] F. Wu and S. Das Sarma, Collective Excitations of Quantum Anomalous Hall Ferromagnets in Twisted Bilayer Graphene, Phys. Rev. Lett. **124**, 046403 (2020).

[70] K. Seo, V. N. Kotov, and B. Uchoa, Ferromagnetic Mott state in Twisted Graphene Bilayers at the Magic Angle, Phys. Rev. Lett. **122**, 246402 (2019).

[71] C. Repellin, Z. Dong, Y.-H. Zhang, and T. Senthil, Ferromagnetism in Narrow Bands of Moir\'e Superlattices, Phys. Rev. Lett. **124**, 187601 (2020).

[72] N. Bultinck, S. Chatterjee, and M. P. Zaletel, Mechanism for Anomalous Hall Ferromagnetism in Twisted Bilayer Graphene, Phys. Rev. Lett. **124**, 166601 (2020).

[73] J. Herzog-Arbeitman, A. Chew, D. K. Efetov, and B. A. Bernevig, Reentrant correlated insulators in twisted bilayer graphene at 25 t (2π flux), Phys. Rev. Lett. **129**, 076401 (2022).

[74] C. Huang, X. Zhang, G. Pan, H. Li, K. Sun, X. Dai, and Z. Meng, Evolution from quantum anomalous Hall insulator to heavy-fermion semimetal in magic-angle twisted bilayer graphene (2023), arxiv:2304.14064 [cond-mat].

[75] F. Guinea and N. R. Walet, Electrostatic effects, band distortions, and superconductivity in twisted graphene bilayers, PNAS **115**, 13174 (2018).

[76] F. Wu, A. H. MacDonald, and I. Martin, Theory of Phonon-Mediated Superconductivity in Twisted Bilayer Graphene, Phys. Rev. Lett. **121**, 257001 (2018).

[77] H. Guo, X. Zhu, S. Feng, and R. T. Scalettar, Pairing symmetry of interacting fermions on a twisted bilayer graphene superlattice, Phys. Rev. B **97**, 235453 (2018).

[78] C.-C. Liu, L.-D. Zhang, W.-Q. Chen, and F. Yang, Chiral Spin Density Wave and $d+id$ Superconductivity in the Magic-Angle-Twisted Bilayer Graphene, Phys. Rev. Lett. **121**, 217001 (2018).

[79] T. J. Peltonen, R. Ojajärvi, and T. T. Heikkilä, Mean-field theory for superconductivity in twisted bilayer graphene, Phys. Rev. B **98**, 220504 (2018).

[80] C. Xu and L. Balents, Topological Superconductivity in Twisted Multilayer Graphene, Phys. Rev. Lett. **121**, 087001 (2018).

[81] H. Isobe, N. F. Q. Yuan, and L. Fu, Unconventional Superconductivity and Density Waves in Twisted Bilayer Graphene, Phys. Rev. X **8**, 041041 (2018).

[82] Y.-Z. You and A. Vishwanath, Superconductivity from valley fluctuations and approximate SO(4) symmetry in a weak coupling theory of twisted bilayer graphene, npj Quantum Mater. **4**, 1 (2019).

[83] B. Lian, Z. Wang, and B. A. Bernevig, Twisted Bilayer Graphene: A Phonon-Driven Superconductor, Phys. Rev. Lett. **122**, 257002 (2019).

[84] J. González and T. Stauber, Kohn-Luttinger Superconductivity in Twisted Bilayer Graphene, Phys. Rev. Lett. **122**, 026801 (2019).

[85] B. Roy and V. Juričić, Unconventional superconductivity in nearly flat bands in twisted bilayer graphene, Phys. Rev. B **99**, 121407 (2019).

[86] A. Julku, T. J. Peltonen, L. Liang, T. T. Heikkilä, and P. Törmä, Superfluid weight and Berezinskii-Kosterlitz-Thouless transition temperature of twisted bilayer graphene, Phys. Rev. B **101**, 060505 (2020).

[87] E. J. König, P. Coleman, and A. M. Tsvelik, Spin magnetometry as a probe of stripe superconductivity in twisted bilayer graphene, Phys. Rev. B **102**, 104514 (2020).

[88] S. Chatterjee, M. Ippoliti, and M. P. Zaletel, Skyrmion Superconductivity: DMRG evidence for a topological route to superconductivity, arXiv:2010.01144 [cond-mat] (2020), arxiv:2010.01144 [cond-mat].

[89] D. V. Chichinadze, L. Classen, and A. V. Chubukov, Nematic superconductivity in twisted bilayer graphene, Phys. Rev. B **101**, 224513 (2020).

[90] E. Khalaf, S. Chatterjee, N. Bultinck, M. P. Zaletel, and A. Vishwanath, Charged skyrmions and topological origin of superconductivity in magic-angle graphene, Science Advances **7**, eabf5299 (2021).

[91] C. Lewandowski, D. Chowdhury, and J. Ruhman, Pairing in magic-angle twisted bilayer graphene: Role of phonon and plasmon umklapp, Phys. Rev. B **103**, 235401 (2021).

[92] Y. Wang, J. Kang, and R. M. Fernandes, Topological and nematic superconductivity mediated by ferro-SU(4) fluctuations in twisted bilayer graphene, Phys. Rev. B **103**, 024506 (2021).

[93] J. M. Park, Y. Cao, K. Watanabe, T. Taniguchi, and P. Jarillo-Herrero, Tunable strongly coupled superconductivity in magic-angle twisted trilayer graphene, Nature **590**, 249 (2021).

[94] J. W. F. Venderbos and R. M. Fernandes, Correlations and electronic order in a two-orbital honeycomb lattice model for twisted bilayer graphene, Phys. Rev. B **98**, 245103 (2018).

[95] J. F. Dodaro, S. A. Kivelson, Y. Schattner, X. Q. Sun, and C. Wang, Phases of a phenomenological model of twisted bilayer graphene, Phys. Rev. B **98**, 075154 (2018).

[96] H. C. Po, L. Zou, A. Vishwanath, and T. Senthil, Origin of Mott Insulating Behavior and Superconductivity in Twisted Bilayer Graphene, Phys. Rev. X **8**, 031089 (2018).

[97] N. F. Q. Yuan and L. Fu, Model for the metal-insulator transition in graphene superlattices and beyond, Phys. Rev. B **98**, 045103 (2018).

[98] L. Balents, C. R. Dean, D. K. Efetov, and A. F. Young, Superconductivity and strong correlations in moiré flat bands, Nat. Phys. **16**, 725 (2020).

[99] B. A. Bernevig, B. Lian, A. Cowsik, F. Xie, N. Regnault, and Z.-D. Song, Twisted bilayer graphene. V. Exact analytic many-body excitations in Coulomb Hamiltonians: Charge gap, Goldstone modes, and absence of Cooper pairing, Phys. Rev. B **103**, 205415 (2021).

[100] F. Wu, E. Hwang, and S. Das Sarma, Phonon-induced giant linear-in-T resistivity in magic angle twisted bilayer graphene: Ordinary strangeness and exotic superconductivity, Phys. Rev. B **99**, 165112 (2019).

[101] F. Xie, Z. Song, B. Lian, and B. A. Bernevig, Topology-Bounded Superfluid Weight in Twisted Bilayer Graphene, Phys. Rev. Lett. **124**, 167002 (2020).

[102] R. M. Fernandes and J. W. F. Venderbos, Nematicity with a twist: Rotational symmetry breaking in a moiré superlattice, Science Advances **6**, eaba8834 (2020).

[103] J. H. Pixley and E. Y. Andrei, Ferromagnetism in magic-angle graphene, Science **365**, 543 (2019).

[104] J. Liu and X. Dai, Anomalous Hall effect, magneto-optical properties, and nonlinear optical properties of twisted graphene systems, npj Computational Materials **6**, 1 (2020).

[105] L. Zou, H. C. Po, A. Vishwanath, and T. Senthil, Band structure of twisted bilayer graphene: Emergent symmetries, commensurate approximants, and Wannier obstructions, Phys. Rev. B **98**, 085435 (2018).

[106] H. C. Po, H. Watanabe, and A. Vishwanath, Fragile Topology and Wannier Obstructions, Phys. Rev. Lett. **121**, 126402 (2018).

[107] K. Hejazi, C. Liu, and L. Balents, Landau levels in twisted bilayer graphene and semiclassical orbits, Phys. Rev. B **100**, 035115 (2019).

[108] J. Ahn, S. Park, and B.-J. Yang, Failure of Nielsen-Ninomiya Theorem and Fragile Topology in Two-Dimensional Systems with Space-Time Inversion Symmetry: Application to Twisted Bilayer Graphene at Magic Angle, Phys. Rev. X **9**, 021013 (2019).

[109] H. C. Po, L. Zou, T. Senthil, and A. Vishwanath, Faithful tight-binding models and fragile topology of magic-angle bilayer graphene, Phys. Rev. B **99**, 195455 (2019).

[110] Z. Song, Z. Wang, W. Shi, G. Li, C. Fang, and B. A. Bernevig, All Magic Angles in Twisted Bilayer Graphene are Topological, Phys. Rev. Lett. **123**, 036401 (2019).

[111] J. Liu, Z. Ma, J. Gao, and X. Dai, Quantum Valley Hall Effect, Orbital Magnetism, and Anomalous Hall Effect in Twisted Multilayer Graphene Systems, Phys. Rev. X **9**, 031021 (2019).

[112] Z.-D. Song, B. Lian, N. Regnault, and B. A. Bernevig, Twisted bilayer graphene. II. Stable symmetry anomaly, Phys. Rev. B **103**, 205412 (2021).

[113] J. Herzog-Arbeitman, Z.-D. Song, N. Regnault, and B. A. Bernevig, Hofstadter topology: Noncrystalline topological materials at high flux, Phys. Rev. Lett. **125**, 236804 (2020).

[114] J. Wang, Y. Zheng, A. J. Millis, and J. Cano, Chiral approximation to twisted bilayer graphene: Exact intravalley inversion symmetry, nodal structure, and implications for higher magic angles, Phys. Rev. Research **3**, 023155 (2021).

[115] S. Dai, Y. Xiang, and D. J. Srolovitz, Twisted Bilayer Graphene: Moiré with a Twist, Nano Lett. **16**, 5923 (2016).

[116] S. K. Jain, V. Juričić, and G. T. Barkema, Structure of twisted and buckled bilayer graphene, 2D Mater. **4**, 015018 (2016).

[117] K. Uchida, S. Furuya, J.-I. Iwata, and A. Oshiyama, Atomic corrugation and electron localization due to Moir\'e patterns in twisted bilayer graphenes, Phys. Rev. B **90**, 155451 (2014).

[118] M. M. van Wijk, A. Schuring, M. I. Katsnelson, and A. Fasolino, Relaxation of moiré patterns for slightly misaligned identical lattices: Graphene on graphite, 2D Mater. **2**, 034010 (2015).

[119] P. Moon and M. Koshino, Optical absorption in twisted bilayer graphene, Physical Review B **87**, 205404 (2013).

[120] S. Carr, S. Fang, Z. Zhu, and E. Kaxiras, Exact continuum model for low-energy electronic states of twisted bilayer graphene, Physical Review Research **1**, 013001 (2019).

[121] S. Fang, S. Carr, Z. Zhu, D. Massatt, and E. Kaxiras, Angle-Dependent Ab initio Low-Energy Hamiltonians for a Relaxed Twisted Bilayer Graphene Heterostructure, arXiv:1908.00058 [cond-mat] (2019), arxiv:1908.00058 [cond-mat].

[122] G. Tarnopolsky, A. J. Kruchkov, and A. Vishwanath, Origin of Magic Angles in Twisted Bilayer Graphene, Phys. Rev. Lett. **122**, 106405 (2019).

[123] D. K. Efimkin and A. H. MacDonald, Helical network model for twisted bilayer graphene, Phys. Rev. B **98**, 035404 (2018).

[124] M. Koshino, N. F. Q. Yuan, T. Koretsune, M. Ochi, K. Kuroki, and L. Fu, Maximally Localized Wannier Orbitals and the Extended Hubbard Model for Twisted Bilayer Graphene, Physical Review X **8**, 031087 (2018).

[125] Y. Huang, P. Hosur, and H. K. Pal, Quasi-flat-band physics in a two-leg ladder model and its relation to magic-angle twisted bilayer graphene, Phys. Rev. B **102**, 155429 (2020).

[126] J. H. Wilson, Y. Fu, S. Das Sarma, and J. H. Pixley, Disorder in twisted bilayer graphene, Phys. Rev. Research **2**, 023325 (2020).

[127] O. Vafek and J. Kang, Lattice model for the Coulomb interacting chiral limit of magic-angle twisted bilayer graphene: Symmetries, obstructions, and excitations, Phys. Rev. B **104**, 075143 (2021).

[128] B. A. Bernevig, Z.-D. Song, N. Regnault, and B. Lian, Twisted bilayer graphene. I. Matrix elements, approximations, perturbation theory, and a $k\ifmmode\cdot\else\textperiodcentered\fi{}p$ two-band model, Phys. Rev. B **103**, 205411 (2021).

[129] B. A. Bernevig, Z.-D. Song, N. Regnault, and B. Lian, Twisted bilayer graphene. III. Interacting Hamiltonian and exact symmetries, Phys. Rev. B **103**, 205413 (2021).

[130] K. Hejazi, X. Chen, and L. Balents, Hybrid Wannier Chern bands in magic angle twisted bilayer graphene and the quantized anomalous Hall effect, Phys. Rev. Research **3**, 013242 (2021).

[131] J. Cao, M. Wang, S.-F. Qian, C.-C. Liu, and Y. Yao, Ab initio four-band Wannier tight-binding model for generic twisted graphene systems, Phys. Rev. B **104**, L081403 (2021).

[132] Y.-Z. Chou and S. D. Sarma, Kondo lattice model in magic-angle twisted bilayer graphene (2022), arxiv:2211.15682 [cond-mat].

[133] A. Davydov, K. Choo, M. H. Fischer, and T. Neu-

pert, Construction of low-energy symmetric Hamiltonians and Hubbard parameters for twisted multilayer systems using ab initio input, Phys. Rev. B **105**, 165153 (2022).

[134] H. Shi and X. Dai, Heavy-fermion representation for twisted bilayer graphene systems, Phys. Rev. B **106**, 245129 (2022).

[135] X. Wang, J. Finney, A. L. Sharpe, L. K. Rodenbach, C. L. Hsueh, K. Watanabe, T. Taniguchi, M. A. Kastner, O. Vafek, and D. Goldhaber-Gordon, Unusual magnetotransport in twisted bilayer graphene from strain-induced open Fermi surfaces, Proceedings of the National Academy of Sciences **120**, e2307151120 (2023).

[136] L. L. H. Lau and P. Coleman, Topological Mixed Valence Model for Twisted Bilayer Graphene (2023), arxiv:2303.02670 [cond-mat].

[137] Y. Cao, D. Chowdhury, D. Rodan-Legrain, O. Rubies-Bigorda, K. Watanabe, T. Taniguchi, T. Senthil, and P. Jarillo-Herrero, Strange Metal in Magic-Angle Graphene with near Planckian Dissipation, Physical Review Letters **124**, 076801 (2020).

[138] P. Stepanov, I. Das, X. Lu, A. Fahimniya, K. Watanabe, T. Taniguchi, F. H. L. Koppens, J. Lischner, L. Levitov, and D. K. Efetov, Untying the insulating and superconducting orders in magic-angle graphene, Nature **583**, 375 (2020).

[139] M. Xie and A. H. MacDonald, Weak-Field Hall Resistivity and Spin-Valley Flavor Symmetry Breaking in Magic-Angle Twisted Bilayer Graphene, Phys. Rev. Lett. **127**, 196401 (2021).

[140] A. Kerelsky, L. J. McGilly, D. M. Kennes, L. Xian, M. Yankowitz, S. Chen, K. Watanabe, T. Taniguchi, J. Hone, C. Dean, A. Rubio, and A. N. Pasupathy, Maximized electron interactions at the magic angle in twisted bilayer graphene, Nature **572**, 95 (2019).

[141] Y. Jiang, X. Lai, K. Watanabe, T. Taniguchi, K. Haule, J. Mao, and E. Y. Andrei, Charge order and broken rotational symmetry in magic-angle twisted bilayer graphene, Nature **573**, 91 (2019).

[142] D. Wong, K. P. Nuckolls, M. Oh, B. Lian, Y. Xie, S. Jeon, K. Watanabe, T. Taniguchi, B. A. Bernevig, and A. Yazdani, Cascade of electronic transitions in magic-angle twisted bilayer graphene, Nature **582**, 198 (2020).

[143] I. Das, X. Lu, J. Herzog-Arbeitman, Z.-D. Song, K. Watanabe, T. Taniguchi, B. A. Bernevig, and D. K. Efetov, Symmetry-broken Chern insulators and Rashba-like Landau-level crossings in magic-angle bilayer graphene, Nature Physics **17**, 710 (2021).

[144] Y. Choi, H. Kim, Y. Peng, A. Thomson, C. Lewandowski, R. Polski, Y. Zhang, H. S. Arora, K. Watanabe, T. Taniguchi, J. Alicea, and S. Nadj-Perge, Tracing out Correlated Chern Insulators in Magic Angle Twisted Bilayer Graphene, arXiv:2008.11746 [cond-mat] (2020), arxiv:2008.11746 [cond-mat].

[145] Y. Choi, H. Kim, C. Lewandowski, Y. Peng, A. Thomson, R. Polski, Y. Zhang, K. Watanabe, T. Taniguchi, J. Alicea, and S. Nadj-Perge, Interaction-driven band flattening and correlated phases in twisted bilayer graphene, Nat. Phys. **17**, 1375 (2021).

[146] Y. Choi, H. Kim, Y. Peng, A. Thomson, C. Lewandowski, R. Polski, Y. Zhang, H. S. Arora, K. Watanabe, T. Taniguchi, J. Alicea, and S. Nadj-Perge, Correlation-driven topological phases in

magic-angle twisted bilayer graphene, Nature **589**, 536 (2021).

[147] J. M. Park, Y. Cao, K. Watanabe, T. Taniguchi, and P. Jarillo-Herrero, Flavour Hund's coupling, Chern gaps and charge diffusivity in moiré graphene, Nature **592**, 43 (2021).

[148] X. Lu, B. Lian, G. Chaudhary, B. A. Piot, G. Romagnoli, K. Watanabe, T. Taniguchi, M. Poggio, A. H. MacDonald, B. A. Bernevig, and D. K. Efetov, Multiple flat bands and topological Hofstadter butterfly in twisted bilayer graphene close to the second magic angle, PNAS **118**, e2100006118 (2021).

[149] A. Rozen, J. M. Park, U. Zondiner, Y. Cao, D. Rodan-Legrain, T. Taniguchi, K. Watanabe, Y. Oreg, A. Stern, E. Berg, P. Jarillo-Herrero, and S. Ilani, Entropic evidence for a Pomeranchuk effect in magic-angle graphene, Nature **592**, 214 (2021).

[150] Y. Saito, F. Yang, J. Ge, X. Liu, T. Taniguchi, K. Watanabe, J. I. A. Li, E. Berg, and A. F. Young, Isospin Pomeranchuk effect in twisted bilayer graphene, Nature **592**, 220 (2021).

[151] I. Das, C. Shen, A. Jaoui, J. Herzog-Arbeitman, A. Chew, C.-W. Cho, K. Watanabe, T. Taniguchi, B. A. Piot, B. A. Bernevig, and D. K. Efetov, Observation of Reentrant Correlated Insulators and Interaction-Driven Fermi-Surface Reconstructions at One Magnetic Flux Quantum per Moir\'e Unit Cell in Magic-Angle Twisted Bilayer Graphene, Phys. Rev. Lett. **128**, 217701 (2022).

[152] P. Seifert, X. Lu, P. Stepanov, J. R. Durán Retamal, J. N. Moore, K.-C. Fong, A. Principi, and D. K. Efetov, Magic-angle bilayer graphene nanocalorimeters: Toward broadband, energy-resolving single photon detection, Nano Letters **20**, 3459 (2020).

[153] M. Otteneder, S. Hubmann, X. Lu, D. A. Kozlov, L. E. Golub, K. Watanabe, T. Taniguchi, D. K. Efetov, and S. D. Ganichev, Terahertz photogalvanics in twisted bilayer graphene close to the second magic angle, Nano Letters **20**, 7152 (2020).

[154] S. Lisi, X. Lu, T. Benschop, T. A. de Jong, P. Stepanov, J. R. Duran, F. Margot, I. Cucchi, E. Cappelli, A. Hunter, A. Tamai, V. Kandyba, A. Giampietri, A. Barinov, J. Jobst, V. Stalman, M. Leeuwenhoek, K. Watanabe, T. Taniguchi, L. Rademaker, S. J. van der Molen, M. P. Allan, D. K. Efetov, and F. Baumberger, Observation of flat bands in twisted bilayer graphene, Nat. Phys. **17**, 189 (2021).

[155] T. Benschop, T. A. de Jong, P. Stepanov, X. Lu, V. Stalman, S. J. van der Molen, D. K. Efetov, and M. P. Allan, Measuring local moiré lattice heterogeneity of twisted bilayer graphene, Phys. Rev. Res. **3**, 013153 (2021).

[156] N. C. H. Hesp, I. Torre, D. Rodan-Legrain, P. Novelli, Y. Cao, S. Carr, S. Fang, P. Stepanov, D. Barcons-Ruiz, H. Herzig Sheinfux, K. Watanabe, T. Taniguchi, D. K. Efetov, E. Kaxiras, P. Jarillo-Herrero, M. Polini, and F. H. L. Koppens, Observation of interband collective excitations in twisted bilayer graphene, Nat. Phys. **17**, 1162 (2021).

[157] S. Hubmann, P. Soul, G. Di Battista, M. Hild, K. Watanabe, T. Taniguchi, D. K. Efetov, and S. D. Ganichev, Nonlinear intensity dependence of photogalvanics and photoconductance induced by terahertz laser radiation in twisted bilayer graphene close to magic angle, Phys. Rev. Mater. **6**, 024003 (2022).

[158] S. Grover, M. Bocarsly, A. Uri, P. Stepanov, G. Di Bat-

tista, I. Roy, J. Xiao, A. Y. Meltzer, Y. Myasoedov, K. Pareek, K. Watanabe, T. Taniguchi, B. Yan, A. Stern, E. Berg, D. K. Efetov, and E. Zeldov, Chern mosaic and Berry-curvature magnetism in magic-angle graphene, Nat. Phys. **18**, 885 (2022).

[159] Y. Choi, J. Kemmer, Y. Peng, A. Thomson, H. Arora, R. Polski, Y. Zhang, H. Ren, J. Alicea, G. Refael, F. von Oppen, K. Watanabe, T. Taniguchi, and S. Nadj-Perge, Electronic correlations in twisted bilayer graphene near the magic angle, Nat. Phys. **15**, 1174 (2019).

[160] C. L. Tschirhart, M. Serlin, H. Polshyn, A. Shragai, Z. Xia, J. Zhu, Y. Zhang, K. Watanabe, T. Taniguchi, M. E. Huber, and A. F. Young, Imaging orbital ferromagnetism in a moiré Chern insulator, Science **372**, 1323 (2021).

[161] Y. Xie, B. Lian, B. Jäck, X. Liu, C.-L. Chiu, K. Watanabe, T. Taniguchi, B. A. Bernevig, and A. Yazdani, Spectroscopic signatures of many-body correlations in magic-angle twisted bilayer graphene, Nature **572**, 101 (2019).

[162] D. Călugăru, M. Borovkov, L. L. H. Lau, P. Coleman, Z.-D. Song, and B. A. Bernevig, Twisted bilayer graphene as topological heavy fermion: II. Analytical approximations of the model parameters, Low Temperature Physics **49**, 640 (2023).

[163] X. Liu, Z. Wang, K. Watanabe, T. Taniguchi, O. Vafek, and J. I. A. Li, Tuning electron correlation in magic-angle twisted bilayer graphene using Coulomb screening, Science **371**, 1261 (2021).

[164] J. Yu, B. A. Foutty, Z. Han, M. E. Barber, Y. Schattner, K. Watanabe, T. Taniguchi, P. Phillips, Z.-X. Shen, S. A. Kivelson, and B. E. Feldman, Correlated hofstadter spectrum and flavour phase diagram in magic-angle twisted bilayer graphene, Nature Physics **18**, 825 (2022).

[165] K. P. Nuckolls, R. L. Lee, M. Oh, D. Wong, T. Soejima, J. P. Hong, D. Călugăru, J. Herzog-Arbeitman, B. A. Bernevig, K. Watanabe, T. Taniguchi, N. Regnault, M. P. Zaletel, and A. Yazdani, Quantum textures of the many-body wavefunctions in magic-angle graphene, Nature **620**, 525 (2023).

[166] D. Călugăru, N. Regnault, M. Oh, K. P. Nuckolls, D. Wong, R. L. Lee, A. Yazdani, O. Vafek, and B. A. Bernevig, Spectroscopy of Twisted Bilayer Graphene Correlated Insulators, Physical Review Letters **129**, 117602 (2022).

[167] A. Georges, G. Kotliar, W. Krauth, and M. J. Rozenberg, Dynamical mean-field theory of strongly correlated fermion systems and the limit of infinite dimensions, Reviews of Modern Physics **68**, 13 (1996).

[168] W. Metzner and D. Vollhardt, Correlated lattice fermions in $d=\infty$ dimensions, Physical review letters **62**, 324 (1989).

[169] M. Haule, E. Y. Andrei, and K. Haule, The Mott-semiconducting state in the magic angle bilayer graphene (2019), arXiv:1901.09852.

[170] A. Datta, M. J. Calderón, A. Camjayi, and E. Bascones, Heavy quasiparticles and cascades without symmetry breaking in twisted bilayer graphene, Nature Communications **14**, 5036 (2023).

[171] H. Hu, G. Rai, L. Crippa, J. Herzog-Arbeitman, D. Călugăru, T. Wehling, G. Sangiovanni, R. Valenti, A. M. Tsvelik, and B. A. Bernevig, Symmetric Kondo Lattice States in Doped Strained Twisted Bilayer Graphene (2023), arxiv:2301.04673 [cond-mat].

[172] S. L. Tomarken, Y. Cao, A. Demir, K. Watanabe, T. Taniguchi, P. Jarillo-Herrero, and R. C. Ashoori, Electronic Compressibility of Magic-Angle Graphene Superlattices, Phys. Rev. Lett. **123**, 046601 (2019).

[173] A. T. Pierce, Y. Xie, J. M. Park, E. Khalaf, S. H. Lee, Y. Cao, D. E. Parker, P. R. Forrester, S. Chen, K. Watanabe, T. Taniguchi, A. Vishwanath, P. Jarillo-Herrero, and A. Yacoby, Unconventional sequence of correlated Chern insulators in magic-angle twisted bilayer graphene, Nature Physics **17**, 1210 (2021).

[174] C. Shen, Y. Chu, Q. Wu, N. Li, S. Wang, Y. Zhao, J. Tang, J. Liu, J. Tian, K. Watanabe, T. Taniguchi, R. Yang, Z. Y. Meng, D. Shi, O. V. Yazyev, and G. Zhang, Correlated states in twisted double bilayer graphene, Nature Physics **16**, 520 (2020).

[175] U. Zondiner, A. Rozen, D. Rodan-Legrain, Y. Cao, R. Queiroz, T. Taniguchi, K. Watanabe, Y. Oreg, F. von Oppen, A. Stern, E. Berg, P. Jarillo-Herrero, and S. Ilani, Cascade of phase transitions and Dirac revivals in magic-angle graphene, Nature **582**, 203 (2020).

[176] I. Pomeranchuk, On the theory of liquid 3-He, Zhurnal Eksperimental'noi i Teoreticheskoi Fiziki **20**, 919 (1950).

[177] A. Georges and W. Krauth, Numerical solution of the $d = \infty$ Hubbard model: Evidence for a Mott transition, Physical Review Letters **69**, 1240 (1992).

[178] A. Georges and W. Krauth, Physical properties of the half-filled Hubbard model in infinite dimensions, Physical Review B **48**, 7167 (1993).

[179] F. Werner, O. Parcollet, A. Georges, and S. R. Hassan, Interaction-Induced Adiabatic Cooling and Antiferromagnetism of Cold Fermions in Optical Lattices, Physical Review Letters **95**, 056401 (2005).

[180] H. Hu, B. A. Bernevig, and A. M. Tsvelik, Kondo Lattice Model of Magic-Angle Twisted-Bilayer Graphene: Hund's Rule, Local-Moment Fluctuations, and Low-Energy Effective Theory (2023), arxiv:2301.04669 [cond-mat].

[181] J. P. Eisenstein, L. N. Pfeiffer, and K. W. West, Negative compressibility of interacting two-dimensional electron and quasiparticle gases, Phys. Rev. Lett. **68**, 674 (1992).

[182] J. M. Riley, W. Meevasana, L. Bawden, M. Asakawa, T. Takayama, T. Eknapakul, T. K. Kim, M. Hoesch, S.-K. Mo, H. Takagi, T. Sasagawa, M. S. Bahramy, and P. D. C. King, Negative electronic compressibility and tunable spin splitting in wse2, Nature Nanotechnology **10**, 1043 (2015).

[183] A. M. J. Schakel, Ground state of electron gases at negative compressibility, Physical Review B **64**, 10.1103/physrevb.64.245101 (2001).

[184] O. Parcollet, M. Ferrero, T. Ayral, H. Hafermann, I. Krivenko, L. Messio, and P. Seth, TRIQS: A Toolbox for Research on Interacting Quantum Systems, Computer Physics Communications **196**, 398 (2015), arxiv:1504.01952 [cond-mat, physics:physics].

[185] P. Seth, I. Krivenko, M. Ferrero, and O. Parcollet, TRIQS/CTHYB: A Continuous-Time Quantum Monte Carlo Hybridization Expansion Solver for Quantum Impurity Problems, Computer Physics Communications **200**, 274 (2016), arxiv:1507.00175 [cond-mat].

[186] M. Aichhorn, L. Pourovskii, P. Seth, V. Vildosola, M. Zingl, O. E. Peil, X. Deng, J. Mravlje, G. J.

Kraberger, C. Martins, M. Ferrero, and O. Parcollet, TRIQS/DFTTools: A TRIQS application for ab initio calculations of correlated materials, Computer Physics Communications **204**, 200 (2016).

[187] N. Parragh, A. Toschi, K. Held, and G. Sangiovanni, Conserved quantities of S U (2) -invariant interactions for correlated fermions and the advantages for quantum Monte Carlo simulations, Physical Review B **86**, 155158 (2012).

[188] M. Wallerberger, A. Hausoel, P. Gunacker, A. Kowalski, N. Parragh, F. Goth, K. Held, and G. Sangiovanni, W2dynamics: Local one- and two-particle quantities from dynamical mean field theory, Computer Physics Communications **235**, 388 (2019).

[189] G. Sangiovanni, A. Toschi, E. Koch, K. Held, M. Capone, C. Castellani, O. Gunnarsson, S.-K. Mo, J. W. Allen, H.-D. Kim, A. Sekiyama, A. Yamasaki, S. Suga, and P. Metcalf, Static versus dynamical mean-field theory of Mott antiferromagnets, Physical Review B **73**, 205121 (2006).

[190] M. Imada, A. Fujimori, and Y. Tokura, Metal-insulator transitions, Rev. Mod. Phys. **70**, 1039 (1998).

[191] A. Amaricci, L. de'Medici, and M. Capone, Mott transitions with partially filled correlated orbitals, Europhysics Letters **118**, 17004 (2017).

[192] L. De' Medici, A. Georges, G. Kotliar, and S. Biermann, Mott Transition and Kondo Screening in f -Electron Metals, Physical Review Letters **95**, 066402 (2005).

[193] J. Kang, B. A. Bernevig, and O. Vafek, Cascades between light and heavy fermions in the normal state of magic angle twisted bilayer graphene, Physical Review Letters **127**, 266402 (2021), arxiv:2104.01145 [cond-mat].

[194] A. Georges, G. Kotliar, and W. Krauth, Superconductivity in the two-band hubbard model in infinite dimensions, Zeitschrift für Physik B Condensed Matter **92**, 313 (1993).

[195] T. Kopp and J. Mannhart, Calculation of the capacitances of conductors: Perspectives for the optimization of electronic devices, Journal of Applied Physics **106**, 064504 (2009).

[196] L. Li, C. Richter, S. Paetel, T. Kopp, J. Mannhart, and R. C. Ashoori, Very Large Capacitance Enhancement in a Two-Dimensional Electron System, Science **332**, 825 (2011).

[197] T. Kopp and J. Mannhart, Calculation of the capacitances of conductors: Perspectives for the optimization of electronic devices, Journal of Applied Physics **106**, 064504 (2009).

[198] P. B. Allen, H. Berger, O. Chauvet, L. Forro, T. Jarlborg, A. Junod, B. Revaz, and G. Santi, Transport properties, thermodynamic properties, and electronic structure of $srruo_3$, Phys. Rev. B **53**, 4393 (1996).

[199] M. Edelmann, G. Sangiovanni, M. Capone, and L. de' Medici, Chromium analogs of iron-based superconductors, Phys. Rev. B **95**, 205118 (2017).

[200] J. E. Gubernatis, M. Jarrell, R. N. Silver, and D. S. Sivia, Quantum Monte Carlo simulations and maximum entropy: Dynamics from imaginary-time data, Physical Review B **44**, 6011 (1991).

[201] G. J. Kraberger and M. Zingl, MaxEnt, TRIQS (2023).

[202] J. Kaufmann and K. Held, ana_cont: Python package for analytic continuation (2021), arXiv:2105.11211 [cond-mat.str-el].

[203] D. Călugăru *et al.*, To appear.

[204] P. Pulay, Convergence acceleration of iterative sequences. the case of scf iteration, Chemical Physics Letters **73**, 393 (1980).

[205] V. I. Anisimov, J. Zaanen, and O. K. Andersen, Band theory and mott insulators: Hubbard u instead of stoner i, Phys. Rev. B **44**, 943 (1991).

[206] I. V. Solovyev, P. H. Dederichs, and V. I. Anisimov, Corrected atomic limit in the local-density approximation and the electronic structure of d impurities in rb, Phys. Rev. B **50**, 16861 (1994).

[207] M. T. Czyżyk and G. A. Sawatzky, Local-density functional and on-site correlations: The electronic structure of la_2cuo_4 and $lacuo_3$, Phys. Rev. B **49**, 14211 (1994).

Appendix A: Non-interacting Hamiltonian

The topological heavy Fermion model is derived and described in [16]. For completeness, we rewrite the single particle Hamiltonian:

$$
\hat{H}_0 = \overbrace{\sum_{|\mathbf{k}|<\Lambda_c} \sum_{aa'\eta\sigma} H_{aa'}^{(c,\eta)}(\mathbf{k}) c_{\mathbf{k}a\eta\sigma}^\dagger c_{\mathbf{k}a'\eta\sigma}}^{\hat{H}_c}
$$
$$
+ \underbrace{\frac{1}{\sqrt{N_M}} \sum_{|\mathbf{k}|<\Lambda_c,\mathbf{R}} \sum_{a\alpha\eta\sigma} \left[e^{i\mathbf{k}\cdot\mathbf{R} - \frac{|\mathbf{k}|^2\lambda^2}{2}} H_{a\alpha}^{(fc,\eta)}(\mathbf{k}) f_{\mathbf{R}\alpha\eta\sigma}^\dagger c_{\mathbf{k}\alpha\eta\sigma} + h.c. \right]}_{\hat{H}_{cf}}. \tag{A1}
$$

The fist term is the dispersion of the c-sector, and Λ_c is a momentum cutoff. The second term is the coupling of the dispersionless f-sector with the c-sector. N_M is the number of moiré unit cells, $\mathbf{R}$ labels the moiré lattice vectors, $\lambda = 0.3375 a_M$ is a damping factor where a_M is the moiré lattice constant. The spin and valley degrees of freedom are decoupled, and at each momentum vector $\mathbf{k}$, the Hamiltonian takes the form of 6×6 matrix per spin and per valley. It can be represented compactly by $H^{(c,\eta)}(\mathbf{k})$ and $H^{(fc,\eta)}(\mathbf{k})$ as shown below

$$
H^{(c,\eta)}(\mathbf{k}) = \begin{pmatrix} 0_{2\times2} & v_\star(\eta k_x \sigma_0 + i k_y \sigma_z) \\ v_\star(\eta k_x \sigma_0 - i k_y \sigma_z) & M\sigma_x \end{pmatrix}, \tag{A2}
$$

$\sigma_{0,x,y,z}$ are Pauli matrices in orbital space, $M = 3.697$ meV defines the bandwidth of the flat bands, $v_\star = -4.303$ eV Å is a fitting parameter.

$$
H^{(fc,\eta)}(\mathbf{k}) = \left(\gamma\sigma_0 + v'_\star(\eta k_x \sigma_x + k_y \sigma_y) \ \ 0_{2\times2} \right), \tag{A3}
$$

$\gamma = -24.75$ meV sets the gap between the flat band and the high energy bands, and $v'_\star = 1.622$ eV Å is a fitting parameter.

Appendix B: Interaction Hamiltonian

The interaction Hamiltonian of the THF model is derived in detail in the SI of [16]. We summarize their calculation here and bring their result to the form we use for our DMFT calculations. The interaction Hamiltonian is computed by performing the Coulomb integrals in the Bistritzer-Macdonald basis

$$
\hat{H}_I = \frac{1}{2} \int d^2\mathbf{r}_1 d^2\mathbf{r}_2 V(\mathbf{r}_1 - \mathbf{r}_2) : \hat{\rho}(\mathbf{r}_1) :: \hat{\rho}(\mathbf{r}_2) :, \tag{B1}
$$

where $V(\mathbf{r}_1 - \mathbf{r}_2)$ is the double-gate-screened Coulomb interaction, and $: \hat{\rho} :$ is the normal-ordered density operator. Of all the terms generated, the most important ones are identified to be the density-density interaction in the $f(c)$-subspace, $\hat{H}_U(\hat{H}_V)$, the density-density interaction mixing c- and f-subspaces, $\hat{H}_W$, and the exchange interaction between the f- and c-subspaces $\hat{H}_J$

$$
\hat{H}_I \approx \hat{H}_U + \hat{H}_W + \hat{H}_V + \hat{H}_J. \tag{B2}
$$

We treat $\hat{H}_U$ with DMFT, $\hat{H}_W$ and $\hat{H}_J$ with Hartree+Fock, and $\hat{H}_V$ with Hartree. Importantly, we treat every term, including the ones in the delocalized c-subspace, on at least a Hartree level. This means that we capture any relative static energy shifts between the different orbitals upon doping. We calculate the Hartree+Fock mean-fields self-consistently making this essentially a charge self-consistent DMFT calculation.

In the following, it is convenient to define the normal-ordered operator with the colon symbol

$$
: f_{\mathbf{R}\alpha_1\eta_1\sigma_1}^\dagger f_{\mathbf{R}\alpha_2\eta_2\sigma_2} := f_{\mathbf{R}\alpha_1\eta_1\sigma_1}^\dagger f_{\mathbf{R}\alpha_2\eta_2\sigma_2} - \frac{1}{2}\delta_{\alpha_1\eta_1\sigma_1;\alpha_2\eta_2\sigma_2}, \tag{B3}
$$

$$
: c_{\mathbf{k}_1 a_1\eta_1\sigma_1}^\dagger c_{\mathbf{k}_2 a_2\eta_2\sigma_2} := c_{\mathbf{k}_1 a_1\eta_1\sigma_1}^\dagger c_{\mathbf{k}_2 a_2\eta_2\sigma_2} - \frac{1}{2}\delta_{\mathbf{k}_1\alpha_1\eta_1\sigma_1;\mathbf{k}_2\alpha_2\eta_2\sigma_2}, \tag{B4}
$$

and the following density matrices

$$O^f_{\alpha_1\eta_1\sigma_1;\alpha_2\eta_2\sigma_2} = \frac{1}{N_M}\sum_{\mathbf{R}}\langle\Psi|:f^\dagger_{\mathbf{R}\alpha_1\eta_1\sigma_1}f_{\mathbf{R}\alpha_2\eta_2\sigma_2}:|\Psi\rangle, \tag{B5}$$

$$O^{c''}_{\alpha_1\eta_1\sigma_1;\alpha_2\eta_2\sigma_2} = \frac{1}{N_M}\sum_{|\mathbf{k}|<|\Lambda_c}\langle\Psi|:c^\dagger_{\mathbf{k}_1 a_1\eta_1\sigma_1}c_{\mathbf{k}_2 a_2\eta_2\sigma_2}:|\Psi\rangle, \quad a_1, a_2 \in [3,4] \tag{B6}$$

$$O^{cf}_{a\eta_1\sigma_1;\alpha_2\eta_2\sigma_2} = \frac{1}{\sqrt{N_M}}\sum_{|\mathbf{k}|<|\Lambda_c}e^{-i\mathbf{k}\cdot\mathbf{R}}\langle\Psi|c^\dagger_{\mathbf{k}a\eta_1\sigma_1}f_{\mathbf{R}\alpha\eta_2\sigma_2}|\Psi\rangle. \tag{B7}$$

O_f is the density matrix in the f-sector, $O^{c''}$ is the density matrix in the $\Gamma_1 \oplus \Gamma_2$ c-sector, and O^{cf} is the c-f off-diagonal block.

1. $\hat{H}_U$: f-f density-density term (on-site)

$$\hat{H}_U = \frac{U}{2}\sum_{\mathbf{R}}\sum_{(\alpha\eta\sigma)\neq(\alpha'\eta'\sigma')}\left(f^\dagger_{\mathbf{R}\alpha\eta\sigma}f_{\mathbf{R}\alpha\eta\sigma}-\frac{1}{2}\right)\left(f^\dagger_{\mathbf{R}\alpha'\eta'\sigma'}f_{\mathbf{R}\alpha'\eta'\sigma'}-\frac{1}{2}\right), \tag{B8}$$

with $U = 57.95$ meV. We treat this term dynamically. In order to perform our charge self-consistent DMFT simulations, it is useful to separate out the bilinear term that enforces charge neutrality. Collecting the bilinear terms in $\hat{H}_U$ and collapsing the sum we obtain

$$\hat{H}_U = \frac{U}{2}\sum_{\mathbf{R}}\sum_{(\alpha\eta\sigma)\neq(\alpha'\eta'\sigma')}f^\dagger_{\mathbf{R}\alpha\eta\sigma}f_{\mathbf{R}\alpha\eta\sigma}f^\dagger_{\mathbf{R}\alpha'\eta'\sigma'}f_{\mathbf{R}\alpha'\eta'\sigma'} - 3.5U\sum_{\mathbf{R}}\sum_{\alpha\eta\sigma}f^\dagger_{\mathbf{R}\alpha\eta\sigma}f_{\mathbf{R}\alpha\eta\sigma} + \mathcal{O}(1). \tag{B9}$$

We call the first term $\hat{H}_{dyn}$, and it enters the DMFT calculation as the interaction Hamiltonian of the impurity problem. The second term forms part of the static Hamiltonian $\hat{H}_{stat}$ along with the remaining three interaction terms decoupled via static mean fields, and the non-interacting terms.

2. $\hat{H}_V$: c-c density-density term

We treat the density-density term within the c-subspace on the Hartree level. Since the primary effect of $\hat{H}_V$ is to shift the relative energies of the c- and f-subspaces, and all the symmetry-breaking happens in the f-subspace, we neglect the Fock contribution (in accordance with [16]). The Hartree contribution is a static shift in the c-subspace depending only on the c-electron filling ν_c

$$\hat{H}_V^{MF} = V\nu_c\sum_{|\mathbf{k}|<\Lambda,a\eta\sigma}c^\dagger_{\mathbf{k}a\eta\sigma}c_{\mathbf{k}a\eta\sigma} + \mathcal{O}(1), \tag{B10}$$

where $V = 48.33$ meV and ν_c is the filling of the c-electrons with respect to charge neutrality. Refer to SI of [16] for derivation.

3. $\hat{H}_W$: c-f density-density term

The Hartree term involves only the orbital-resolved occupations, contributing a static shift in the f-(c-)sector depending on the occupation of the c-(f-)sector:

$$\sum_{|\mathbf{k}|<\Lambda_c}\sum_{a\eta\sigma}W_a\nu_f:c^\dagger_{\mathbf{k}a\eta\sigma}c_{\mathbf{k}a\eta\sigma}:+\sum_{\mathbf{R}}\sum_{a\alpha\eta\sigma}W_a\nu_{c,a}:f^\dagger_{\mathbf{R}\alpha\eta\sigma}f_{\mathbf{R}\alpha\eta\sigma}:+\mathcal{O}(1). \tag{B11}$$

The Fock term involves the c-f density matrix:

$$-\frac{1}{\sqrt{N_M}}\sum_{\mathbf{R}}\sum_{|\mathbf{k}|<\Lambda_c}\sum_{\alpha\alpha'\eta\eta'\sigma\sigma'}W_a(O^{cf}_{a\eta'\sigma',\alpha\eta\sigma}e^{i\mathbf{k}\cdot\mathbf{R}}f^\dagger_{\mathbf{R}\alpha\eta\sigma}c_{\mathbf{k}a\eta'\sigma'}+h.c.)+\mathcal{O}(1). \tag{B12}$$

Thee coupling to the Γ_3 c-sector is $W_1 = W_2 = 44.03$ meV, and the coupling to the $\Gamma_1 \oplus \Gamma_2$ sector is $W_3 = W_4 = 50.20$ meV. See SI of [171] for derivation.

4. $\hat{H}_J$: c-f exchange term

$\hat{H}_J$ is a ferromagnetic exchange coupling with $J = 16.38$ meV. The Hartree term takes the form

$$\frac{J}{2} \sum_{\mathbf{R}} \sum_{\alpha\alpha'\eta\eta'\sigma\sigma'} : f^\dagger_{\mathbf{R},\alpha\eta\sigma} f_{\mathbf{R},\alpha'\eta'\sigma'} : O^{c''}_{\alpha'\eta'\sigma',\alpha\eta\sigma}$$

$$+ \frac{J}{2} \sum_{|\mathbf{k}|<\mathbf{\Lambda_c}} \sum_{\alpha\alpha'\eta\eta'\sigma\sigma'} : c^\dagger_{\mathbf{k},\alpha\eta\sigma} c_{\mathbf{k}',\alpha'\eta'\sigma'} : O^f_{\alpha'\eta'\sigma',\alpha\eta\sigma} + \mathcal{O}(1) \tag{B13}$$

For the Fock term, it is useful to define the mean fields V_3, V_4 (following the nomenclature in [171])

$$V_3 = \sum_{\mathbf{R}} \sum_{|\mathbf{k}|<\Lambda_c} \sum_{\alpha\eta\sigma} \frac{e^{i\mathbf{k}\cdot\mathbf{R}} \delta_{1,\eta(-1)^{\alpha+1}}}{N_M \sqrt{N_M}} \langle\psi| f^\dagger_{\mathbf{R}\alpha\eta\sigma} c_{\mathbf{k}\alpha+2\eta\sigma} |\psi\rangle \tag{B14}$$

$$V_4 = \sum_{\mathbf{R}} \sum_{|\mathbf{k}|<\Lambda_c} \sum_{\alpha\eta\sigma} \frac{e^{i\mathbf{k}\cdot\mathbf{R}} \delta_{-1,\eta(-1)^{\alpha+1}}}{N_M \sqrt{N_M}} \langle\psi| f^\dagger_{\mathbf{R}\alpha\eta\sigma} c_{\mathbf{k}\alpha+2\eta\sigma} |\psi\rangle \tag{B15}$$

The Fock term is

$$J \sum_{\mathbf{R}} \sum_{|\mathbf{k}|<\Lambda_c} \sum_{\alpha\eta\sigma} \left\{ \frac{e^{-i\mathbf{k}\cdot\mathbf{R}}}{\sqrt{N_M}} \left[\delta_{1,\eta(-1)^{\alpha+1}} f^\dagger_{\mathbf{R}\alpha\eta\sigma} c_{\mathbf{k}\alpha+2\eta\sigma} V_3^* + \delta_{-1,\eta(-1)^{\alpha+1}} f^\dagger_{\mathbf{R}\alpha\eta\sigma} c_{\mathbf{k}\alpha+2\eta\sigma} V_4^* \right] + h.c. \right\} + \mathcal{O}(1) \tag{B16}$$

5. Summary

All together, we arrive at the Hamiltonian $\hat{H}_{stat} + \hat{H}_{dyn}$ for the "charge self-consistent" DMFT calculation with

$$\hat{H}_{dyn} = \frac{U}{2} \sum_{\mathbf{R}} \sum_{(\alpha\eta\sigma)\neq(\alpha'\eta'\sigma')} f^\dagger_{\mathbf{R}\alpha\eta\sigma} f_{\mathbf{R}\alpha\eta\sigma} f^\dagger_{\mathbf{R}\alpha'\eta'\sigma'} f_{\mathbf{R}\alpha'\eta'\sigma'} \tag{B17}$$

$$\hat{H}_{stat} = \hat{H}_0 - 3.5U \sum_{\mathbf{R}} \sum_{\alpha\eta\sigma} f^\dagger_{\mathbf{R}\alpha\eta\sigma} f_{\mathbf{R}\alpha\eta\sigma} + V\nu_c \sum_{|\mathbf{k}|<\Lambda, a\eta\sigma} c^\dagger_{\mathbf{k}a\eta\sigma} c_{\mathbf{k}a\eta\sigma}$$

$$+ \sum_{|\mathbf{k}|<\Lambda_c} \sum_{a\eta\sigma} W_a \nu_f : c^\dagger_{\mathbf{k}a\eta\sigma} c_{\mathbf{k}a\eta\sigma} : + \sum_{\mathbf{R}} \sum_{a\alpha\eta\sigma} W_a \nu_{c,a} : f^\dagger_{\mathbf{R}\alpha\eta\sigma} f_{\mathbf{R}\alpha\eta\sigma} :$$

$$+ -\frac{1}{\sqrt{N_M}} \sum_{\mathbf{R}} \sum_{|\mathbf{k}|<\mathbf{\Lambda_c}} \sum_{\alpha\alpha'\eta\eta'\sigma\sigma'} W_a (O^{cf}_{a\eta'\sigma',\alpha\eta\sigma} e^{i\mathbf{k}\cdot\mathbf{R}} f^\dagger_{\mathbf{R}\alpha\eta\sigma} c_{\mathbf{k}a\eta'\sigma'} + h.c.)$$

$$+ \frac{J}{2} \sum_{\mathbf{R}} \sum_{\alpha\alpha'\eta\eta'\sigma\sigma'} (\eta\eta' + (-1)^{\alpha+\alpha'}) : f^\dagger_{\mathbf{R},\alpha\eta\sigma} f_{\mathbf{R},\alpha'\eta'\sigma'} : O^{c''}_{\alpha'\eta'\sigma',\alpha\eta\sigma}$$

$$+ \frac{J}{2} \sum_{|\mathbf{k}|<\mathbf{\Lambda_c}} \sum_{\alpha\alpha'\eta\eta'\sigma\sigma'} (\eta\eta' + (-1)^{\alpha+\alpha'}) : c^\dagger_{\mathbf{k},\alpha\eta\sigma} c_{\mathbf{k}',\alpha'\eta'\sigma'} : O^f_{\alpha'\eta'\sigma',\alpha\eta\sigma}$$

$$+ J \sum_{\mathbf{R}} \sum_{|\mathbf{k}|<\Lambda_c} \sum_{\alpha\eta\sigma} \left\{ \frac{e^{-i\mathbf{k}\cdot\mathbf{R}}}{\sqrt{N_M}} \left[\delta_{1,\eta(-1)^{\alpha+1}} f^\dagger_{\mathbf{R}\alpha\eta\sigma} c_{\mathbf{k}\alpha+2\eta\sigma} V_3^* + \delta_{-1,\eta(-1)^{\alpha+1}} f^\dagger_{\mathbf{R}\alpha\eta\sigma} c_{\mathbf{k}\alpha+2\eta\sigma} V_4^* \right] + h.c. \right\}$$

$$+ \mathcal{O}(1). \tag{B18}$$

In addition to the self-energy Σ, we have a second self-consistently computed quantity—the full $f \oplus c$ density matrix of the system ρ. They are both needed to fix $\hat{H}_{stat}$.

Appendix C: DMFT Implementation

In practice, we have two iteration-dependent quantities: the density matrix of the system ρ^i and the f-projected self-energy Σ^i, where the label i refers to the iteration number. The dynamic self-energy is zero in the c-subspace, so
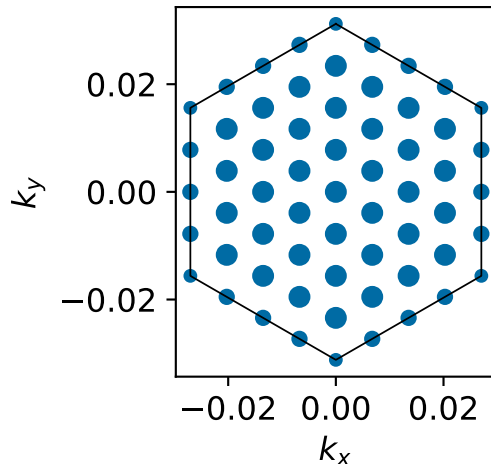
FIG. C.1. Regular centered sampling of the first moiré Brillouin zone. Edges and corners are weighted $1/2$ and $1/3$ respectively. In this example `sample_len=4`.

we can always promote Σ^i to the full $c \oplus f$ space by padding with zeros. The static part of the c-sector self-energy is already included in the mean-field terms in $\hat{H}_{stat}$ and we assume that there is no frequency-dependent component. In each iteration, ρ^i fixes $\hat{H}_{stat}$, which together with Σ^i gives us the local lattice Green function. We project the local lattice Green function to the f-subspace and compute the Weiss field, which we then input to the CT-QMC impurity solver in addition to $\hat{H}_{dyn}$. The impurity solver gives us a new self-energy Σ^{i+1} and a new interacting impurity Green function from which we compute the new density matrix ρ^{i+1}. This step is repeated until the density matrix and the self-energy converge. We choose a static self-energy for the initial guess. The exact value is inconsequential as long as it is reasonable, i.e. as long as the f-bands lie close to the Fermi level between the upper and lower c-bands. We use the initial choice of the density matrix to specify a particular symmetry-broken phase or the symmetric phase.

In DMFT, we consider the local Hamiltonian. We consider a single moiré lattice site labelled by $\mathbf{R} = (0, 0)$, so that $N_M = 1$. We sum momenta over the first moiré Brillouin zone (FMBZ), meaning that all references to $|\mathbf{k}| < \Lambda_c$ are rather $\mathbf{k} \in FMBZ$. We sample the FMBZ with a regular centered grid. The resolution is parametrized by a number `sample_len`, which counts the number of steps between Γ and K. Points on the edges and corners are degenerate, and therefore weighted $1/2$ and $1/3$ respectively. See Fig. C.1 for an example grid.

Note that for calculations in the symmetric phase, we simplified the interaction Hamiltonian further by neglecting the Fock part of $\hat{H}_W$ and setting the W-coupling with both c-sectors to be equivalent $W_a \to \frac{W_1 + W_3}{2} = 47.12$ meV. The $\hat{H}_J$ contribution to the symmetric state is zero. This allows the static self-consistency loop to be absorbed into a double counting term as described in the SI of [171] which is relatively seamless to incorporate in DMFT codes. We have checked for a range of parameter values that the differences with the full calculation are solely quantitative and small.

As an extra check to ensure the accuracy of our calculations, we implemented our model twice with two different DMFT codes independently, and compared test cases. GR worked with the TRIQS suite of packages, and LC worked with w2dynamics.

1. TRIQS runs

a. DMFT parameters

For summation within the DMFT runs, we used a grid with `sample_len=9`, which has 271 points. We considered our system converged when the maximum element of the difference of the current and previous density matrix reached order 10^{-3}. This took between 50-200 iterations. At most fillings and temperatures, we used a mixing factor of 0.9, i.e. the new self energy and density matrix were nine parts the output of the impurity solver and one part the previous self-energy or density matrix. In regions where convergence was difficult (where the Fermi level hits the flat band, and negative compressibility is seen), we used lower mixing factors. For most fillings and temperatures, we updated the self-energy and density matrix every iteration. In regions of difficult convergence, we updated the density matrix

only every 2, 3, or 5 iterations.

b. QMC parameters

In the convergence runs, we used the QMC solver with 1.2×10^7 total cycles (measurements) distributed on 192 cores, with 5000 warmup cycles. Each cycle consisted of 1000 QMC moves. We measured in the imaginary time basis, and performed a tail fit with 4 moments. The tail fitting window, defined by the lower (`fit_min_n`) and upper Matsubara frequency index (`fit_max_n`), depends strongly on temperature and we chose it heuristically to be `fit_min_n` $= \lfloor 160T^{-0.9577746167096538}) \rfloor$ and `fit_max_n` $= \lfloor 209T^{-0.767031728744396} \rfloor$

c. Analytic continuation

We use the maximum entropy method [200] as implemented in triqs_maxent package [201] to obtain the spectral functions on the real axis. We first analytically continue the imaginary-frequency self-energy obtained from the CT-QMC solver to a real-frequency self-energy. Then, we use the real-frequency self-energy to compute the Green functions, spectral functions, etc on the real axis. We always perform the analytic continuation step in the natural basis defined by the chosen symmetry-broken phase (see App. D). In this basis, the self-energy is diagonal, which allows us to avoid the complications inherent in analytically continuing matrix quantities.

The self-energy continuation method uses an intermediate auxiliary object $G_{aux}(\omega)$. We use a hyperbolic mesh for the auxiliary spectral function $A_{aux}(\omega)$, such that we have an energy resolution of about 0.01, 0.2, and 1 meV at $\omega = 0, 1$ and 20 meV respectively.

2. w2dynamics runs

The k-space Hamiltonian grid for the *w2dynamics* runs was independently generated following the same weighting philosophy described above. To account for the larger weight of the bulk points with respect to the edges and corners of the BZ, an oversampling strategy was adopted considering duplicated k-points in the number of 6 for the bulk, 3 for the edges and 2 for the corners, for a total of 2071 k-points.

a. DMFT parameters

As a criterion for convergence of the DMFT simulations we considered the step-by-step variation of local observables such as orbital/spin/valley - resolved occupations with a threshold of 10^{-4}. Since the compressibility runs were obtained at high temperature ($\approx 11K$), i.e. in the disordered phase, convergence was rather quick and never required more than 50 DMFT loops. In order to properly follow the compressibility curve in the negative slope branches, we run every simulation at increasing values of ν starting from the converged self-energy of the previous step. For the same reason, the mixing factor was set at 0.5. The spacing between doping values was in general 0.025, but it was decreased in more challenging intervals such as the negative slope branches of the compressibility curves and around the divergence points of the inverse compressibility. The total number of points for the fixed-ν simulations is 325, and for the fixed-μ simulations it is 218.

b. QMC parameters

For the QMC runs with $T = 11.6K$ we used 144 CPU cores. At each DMFT loop a sufficient number of measurements was found to be `Nmeas` $= 7.5 \cdot 10^4$ per core, with a number of steps `Ncorr` $= 2000$ per core between successive measurements to avoid autocorrelation effects. `Nwarmup` $= 2 \cdot 10^6$ steps per core were run before each measurement begun. We measured in imaginary time domain and used the Legendre polynomial basis, with maximum order `NLegMax` $= 35$.

c. Analytic continuation

Analytical continuation was performed starting from the last DMFT run using the MaxEnt method from the *ana_cont* software suite [202]. For the local spectral function $A(\omega)$ plots, we performed analytic continuation of the Matsubara-summed local Green's function, extracted from the last DMFT loop of each simulation. For the momentum-resolved spectral function plots, we analytically continue the self-energy, and use the resulting real-frequency $\Sigma(\omega)$ in the calculation of $A(\mathbf{k}, \omega)$. The self-energy has no off-diagonal components in the symmetric phase. We used a regular mesh of 1001 real-axis frequency points in the interval $[-250 : +250]$ meV for $A(\omega)$ and $[-300 : +300]$ meV for $\Sigma(\omega)$ and no preblur.

Appendix D: Breaking symmetries

We specify a chosen symmetry-broken state through the *parent state* density matrix, ρ^0. In the parent states, all doped charge goes to the f-subspace, i.e. the c-subspace is always half-filled. In the f-subspace, we choose the up spin sector to be in the K-IVC phase, and the down spin sector to be in the K-IVC, valley-polarized, or disordered phases at fillings $\nu = 0, -1, -2$.

$$\rho_{f,\uparrow}^0(\nu) = \frac{1}{2}\sigma_0\tau_0 - \frac{1}{2}\sigma_y\tau_y$$

$$\rho_{f,\downarrow}^0(\nu) = \begin{cases} \frac{1}{2}\sigma_0\tau_0 - \frac{1}{2}\sigma_y\tau_y & \text{for } \nu = 0 \\ \text{diag}([1,0,0,0]) & \text{for } \nu = -1 \\ \text{diag}([0,0,0,0]) & \text{for } \nu = -2 \end{cases} \quad (D1)$$

$$\rho_{c(\Gamma_3)}^0(\nu) = \rho_{c(\Gamma_1\oplus\Gamma_2)}^0(\nu) = \frac{1}{2}\sigma_0\tau_0\zeta_0$$

where $\sigma_\mu, \tau_\mu, \zeta_\mu$, are Pauli matrices in orbital, valley and spin space, with $\mu = 0, x, y, z$, and the subscripts $(f, c(\ldots))$, $(\uparrow, \downarrow)$ signify projections to the electron species or spin sector.

The polarizing field $\hat{H}_{pol}$ used to bias the system towards a given ordered state is defined by the parent state density matrices

$$\hat{H}_{pol} = -\lambda_{pol}\Psi^\dagger \left(\rho^0 - \rho^{0,symm}\right)\Psi \quad (D2)$$

where Ψ is a vector of c and f operators in the same order as in ρ_0, and $\rho^{0,symm}$ are the analog of the parent state density matrices for the symmetric phase:

$$\rho_{c(\Gamma_3)}^{0,symm} = \rho_{c(\Gamma_1\oplus\Gamma_2)}^{0,symm} = \frac{1}{2}\sigma_0\tau_0\zeta_0, \quad (D3)$$

$$\rho_f^{0,symm} = \left(\frac{1}{2} + \frac{\nu}{8}\right)\sigma_0\tau_0\zeta_0, \quad (D4)$$

where $\nu = 0, -1, -2$.

We chose the strength of the polarizing field λ_{pol} to be 3 meV. We found it sufficient to turn off the polarizing field after 10 iterations.

1. Basis rotation and symmetrization

In order to minimize the sign problem in the QMC simulations, we specify the impurity problem in the natural basis of the parent state density matrix, in which the hybridization function (the dynamical mean-field that describes electrons hopping in and out of the bath) is (almost diagonal) diagonal in the (ordered) symmetric phases. In the symmetric phase or when a spin sector is valley-polarized, the natural basis coincides with the original heavy Fermion basis, so no rotation is needed. When a spin sector has K-IVC order, a basis rotation is required. For instance, in the K-IVC+VP parent state at $\nu = -1$ described by the density matrix in (D1), the corresponding wave function is written as

$$\begin{aligned} \left| \text{K-IVC+VP}_0^{\nu=-1} \right\rangle = &\frac{1}{2} f_{1+\downarrow}^\dagger (f_{1+\uparrow}^\dagger + f_{2-\uparrow}^\dagger) \\ &\times (-f_{1-\uparrow}^\dagger + f_{2+\uparrow}^\dagger) \left| FS \right\rangle, \end{aligned} \quad (D5)$$

where $|FS\rangle$ is the Fermi sea of all the lower c bands occupied. In this case, the natural basis in the up spin sector corresponds to the operators $\tilde{f}_{\tilde{\alpha}\tilde{\eta}\uparrow}$ defined by

$$\tilde{f}_{1\pm s} = \frac{1}{\sqrt{2}}(f^\dagger_{1+s} \pm f^\dagger_{2-s}) \tag{D6}$$

$$\tilde{f}_{2\pm s} = \frac{1}{\sqrt{2}}(\mp f^\dagger_{1-s} + f^\dagger_{2+s}) \tag{D7}$$

In the natural basis, the self-energy is diagonal. We symmetrize the self-energy output by the QMC solver after every iteration. For calculations in the symmetric phase, this takes the form $\Sigma_{x'x'} \to \frac{1}{8}\sum_x \Sigma_{xx}$, where the index x represents combined orbital, valley, and spin indices. In the symmetry-broken phase, a reduced symmetrization is applicable. Based on the parent states in (D1), the sets of degenerate elements are

$$
\begin{array}{ll}
\{\tilde{f}_{1+\uparrow}, \tilde{f}_{2+\uparrow}, \tilde{f}_{1+\downarrow}, \tilde{f}_{2+\downarrow}\}, \{\tilde{f}_{1-\uparrow}, \tilde{f}_{2-\uparrow}, \tilde{f}_{1-\downarrow}, \tilde{f}_{2-\downarrow}\} & \text{K-IVC at } \nu = 0 - \delta \\
\{\tilde{f}_{1+\uparrow}, \tilde{f}_{2+\uparrow}\}, \{\tilde{f}_{1-\uparrow}, \tilde{f}_{2-\uparrow}\}, \{f_{1-\downarrow}, f_{2-\downarrow}\}, \{f_{1+\downarrow}\}, \{f_{2+\downarrow}\} & \text{K-IVC+VP at } \nu = -1 \mp \delta \\
\{\tilde{f}_{1+\uparrow}, \tilde{f}_{2+\uparrow}\}, \{\tilde{f}_{1-\uparrow}, \tilde{f}_{2-\uparrow}\}, \{f_{1+\downarrow}, f_{2+\downarrow}, f_{1-\downarrow}, f_{2-\downarrow}\} & \text{K-IVC at } \nu = -2 \mp \delta
\end{array}
\tag{D8}
$$

The self-energy is symmetrized within each set of degenerate orbitals. This symmetrization procedure is connected to the symmetries of the THF in App. E.

2. Order parameter

In the ordered state, we find the solution at an arbitrary filling ν and temperature T by gradually doping the solution away from a reference integer fillings $\nu_{ref} = 0, -1$ or -2 and temperature T. As we dope away from the integer filling, the system may or may not stay in the ordered state. We quantify this using the order parameter defined as follows. For an f-projected density matrix $\rho_f^{\nu_{ref}}(\nu, T)$ corresponding to the self-consistent solution at filling ν and temperature T continued from the symmetry-broken self-consistent solution at $\nu_{ref} = 0, -1$, or -2 and temperature T, the order parameter $O^{\nu_{ref}}(\nu, T)$ is given by

$$
O^{\nu_{ref}}(\nu, T) = \\
\left\langle \left(\rho_f^0(\nu_{ref}) - \left(\frac{1}{2} + \frac{\nu_{ref}}{8}\right)\mathbf{Id}\right), \left(\rho_f^{\nu_{ref}}(\nu, T)\right) \right\rangle,
\tag{D9}
$$

where $\langle A, B \rangle = \text{trace}(\bar{A}^T \cdot B)$ is the matrix inner product, $\mathbf{Id}$ is the identity, and $\rho_f^0(\nu_{ref})$ is the density matrix of the parent state at ν_{ref}. This definition has the advantage that all types of order (spin polarization, IVC, VP, etc.) are treated on the same footing, so we can plot all three panels in Fig. 2(a) together. The order parameter is constrained to $[0, 1]$ under the reasonable assumption that the self-consistent solution does not flip the sign of the polarization of the parent state.

Appendix E: Finite-temperature Hartree-Fock theory for the THF model

This appendix provides a concise overview of the finite-temperature Hartree-Fock theory as it applies to the THF model, elaborating on the comprehensive discussion found in Ref. [203]. Initially, we revisit the notation set forth in Ref. [203], which treats the f- and c-electrons on equal footing. Subsequently, we derive the Hartree-Fock Hamiltonian for a generic symmetry-broken ground state. In the final section, we adapt the self-consistent Hartree-Fock algorithm to accommodate the partial symmetrization methods delineated in D 1. This adjustment enables a direct comparison between DMFT and finite-temperature Hartree-Fock simulations, as both now incorporate a similar symmetrization approach.

1. Generic notation

Within the THF Hamiltonian from Eq. (A1), the c-fermions are only defined within a limited region around the Γ_M point. Following Ref. [203], we will extend the Λ_c cutoff so that the $c^\dagger_{\mathbf{k}, a, \eta, \sigma}$ fermion covers exactly one Brillouin

zone. Next, we introduce the $\gamma^\dagger_{\mathbf{k},\eta,i,\sigma}$ fermions (for $1 \leq i \leq 6$), which are defined by

$$\gamma^\dagger_{\mathbf{k},\eta,i,\sigma} \equiv \begin{cases} c^\dagger_{\mathbf{k},\eta,i,\sigma}, & \text{for} \quad 1 \leq i \leq 4 \\ f^\dagger_{\mathbf{k},\eta,i-4,\sigma}, & \text{for} \quad 5 \leq i \leq 6 \end{cases}. \tag{E1}$$

The corresponding single-particle Hamiltonian matrix, whose blocks are given by Eq. (A2) and Eq. (A3), reads as

$$h^\eta(\mathbf{k}) = \begin{pmatrix} H^{(c,\eta)}(\mathbf{k}) & H^{\dagger(fc,\eta)}(\mathbf{k}) \\ H^{(fc,\eta)}(\mathbf{k}) & 0_{2\times 2} \end{pmatrix}. \tag{E2}$$

With the new notation at hand, the density matrix of the system is given by

$$\varrho_{i\eta\sigma;i'\eta'\sigma'}(\mathbf{k}) = \left\langle : \gamma^\dagger_{\mathbf{k},i,\eta,\sigma}\gamma_{\mathbf{k},i'\eta'\sigma'} : \right\rangle, \tag{E3}$$

where $\left\langle \hat{\mathcal{O}} \right\rangle$ denotes the expectation value of the operator $\hat{\mathcal{O}}$ in the grand canonical ensemble of the system (at temperature T and chemical potential μ). Throughout this work, we restrict ourselves to states that preserve moiré translation symmetry. The total filling of the f- and c-electrons are related to the traces of the corresponding diagonal blocks of the density matrix,

$$\nu_c = \frac{1}{N_M} \sum_{i=1}^{4} \sum_{\mathbf{k},\eta,\sigma} \varrho_{i\eta\sigma;i\eta\sigma}(\mathbf{k}) \quad \text{and} \quad \nu_f = \frac{1}{N_M} \sum_{i=5}^{6} \sum_{\mathbf{k},\eta,\sigma} \varrho_{i\eta\sigma;i\eta\sigma}(\mathbf{k}), \tag{E4}$$

while the total electron filling is $\nu = \nu_c + \nu_f$.

2. Hartree-Fock Hamiltonian

In this section, we briefly review the finite-temperature Hartree-Fock theory of the THF model [203]. For a given state of the system characterized by the density matrix $\varrho_{i\eta\sigma;i'\eta'\sigma'}(\mathbf{k})$, the interaction Hartree-Fock Hamiltonian of the model can be obtained via the standard decoupling procedure [203] and is given by

$$H_{I,\text{MF}} = \sum_{\substack{i,\eta,\sigma \\ i',\eta',\sigma'}} h^{I,\text{MF}}_{i\eta\sigma;i'\eta'\sigma'}(\mathbf{k})\gamma^\dagger_{\mathbf{k},i,\eta,\sigma}\gamma_{\mathbf{k},i',\eta',\sigma'} + E_0, \tag{E5}$$

where the corresponding Hartree-Fock Hamiltonian matrix reads as

$$\begin{aligned}
h^{I,\text{MF}}_{i\eta\sigma;i'\eta'\sigma'}(\mathbf{k}) = & \sum_{\alpha=1}^{2} \left(U\nu_f + \frac{1}{N_M}\sum_{a=1}^{4} W_a \sum_{\mathbf{k}'}\sum_{\eta'',\sigma''} \varrho_{a\eta''\sigma'';a\eta''\sigma''}(\mathbf{k}') \right) \delta_{(\alpha+4)i}\delta_{(\alpha+4)i'}\delta_{\eta\eta'}\delta_{\sigma\sigma'} \\
& + \sum_{a=1}^{4} (V\nu_c + W_a\nu_f)\delta_{ai}\delta_{ai'}\delta_{\eta\eta'}\delta_{\sigma\sigma'} \\
& - \frac{U}{N_M}\sum_{\alpha,\alpha'=1}^{2} \delta_{(\alpha+4)i}\delta_{(\alpha'+4)i'}\sum_{\mathbf{k}'}\varrho_{i'\eta'\sigma';i\eta\sigma}(\mathbf{k}') \\
& - \sum_{\alpha=1}^{2}\sum_{a'=1}^{4}\frac{W_{a'}}{N_M}\left[\delta_{(\alpha+4)i}\delta_{a'i'} + \delta_{(\alpha+4)i'}\delta_{a'i}\right]\sum_{\mathbf{k}'}\varrho_{i'\eta'\sigma';i\eta\sigma}(\mathbf{k}') \\
& + \frac{1}{N_M}\sum_{\substack{i_1,\eta_1,\sigma_1 \\ i_2,\eta_2,\sigma_2}} (\mathcal{J}_{i_1\eta_1\sigma_1;i_2\eta_2\sigma_2;i\eta\sigma;i'\eta'\sigma'} + \mathcal{J}_{i\eta\sigma;i'\eta'\sigma';i_1\eta_1\sigma_1;i_2\eta_2\sigma_2})\sum_{\mathbf{k}'}\varrho_{i_1\eta_1\sigma_1;i_2\eta_2\sigma_2}(\mathbf{k}') \\
& - \frac{1}{N_M}\sum_{\substack{i_1,\eta_1,\sigma_1 \\ i_2,\eta_2,\sigma_2}} (\mathcal{J}_{i_1\eta_1\sigma_1;i'\eta'\sigma';i\eta\sigma;i_2\eta_2\sigma_2} + \mathcal{J}_{i\eta\sigma;i_2\eta_2\sigma_2;i_1\eta_1\sigma_1i'\eta'\sigma'})\sum_{\mathbf{k}'}\varrho_{i_1\eta_1\sigma_1;i_2\eta_2\sigma_2}(\mathbf{k}'), \tag{E6}
\end{aligned}$$

$$E_0 = -N_M \frac{U\nu_f^2}{2} + \frac{U}{2N_m} \sum_{\mathbf{k},\mathbf{k}'} \sum_{\alpha,\alpha'=1}^{2} \sum_{\substack{\eta,\sigma \\ \eta',\sigma'}} \varrho_{(\alpha'+4)\eta'\sigma';(\alpha+4)\eta\sigma}(\mathbf{k}') \, \varrho_{(\alpha+4)\eta\sigma;(\alpha'+4)\eta'\sigma'}(\mathbf{k})$$

$$- \sum_{a=1}^{4} W_a \nu_f \sum_{\mathbf{k},\eta,\sigma} \varrho_{a\eta\sigma;a\eta\sigma}(\mathbf{k}) + \frac{1}{N_M} \sum_{\mathbf{k}',\mathbf{k}} \sum_{a=1}^{4} W_a \varrho_{a'\eta'\sigma';(a+4)\eta\sigma}(\mathbf{k}') \varrho_{(a+4)\eta\sigma;a'\eta'\sigma'}(\mathbf{k}) - V\frac{\nu_c^2}{2}$$

$$- \frac{1}{2N_M} \sum_{\substack{i_1,\eta_1,\sigma_1 \\ i_2,\eta_2,\sigma_2}} \left(\mathcal{J}_{i_1\eta_1\sigma_1;i_2\eta_2\sigma_2;i\eta\sigma;i'\eta'\sigma'} + \mathcal{J}_{i\eta\sigma;i'\eta'\sigma';i_1\eta_1\sigma_1;i_2\eta_2\sigma_2} \right) \sum_{\mathbf{k}'} \varrho_{i_1\eta_1\sigma_1;i_2\eta_2\sigma_2}(\mathbf{k}') \sum_{\mathbf{k}} \rho_{i\eta\sigma;i'\eta'\sigma'}(\mathbf{k})$$

$$+ \frac{1}{2N_M} \sum_{\substack{i_1,\eta_1,\sigma_1 \\ i_2,\eta_2,\sigma_2}} \left(\mathcal{J}_{i_1\eta_1\sigma_1;i'\eta'\sigma';i\eta\sigma;i_2\eta_2\sigma_2} + \mathcal{J}_{i\eta\sigma;i_2\eta_2\sigma_2;i_1\eta_1\sigma_1 i'\eta'\sigma'} \right) \sum_{\mathbf{k}'} \varrho_{i_1\eta_1\sigma_1;i_2\eta_2\sigma_2}(\mathbf{k}') \sum_{\mathbf{k}} \rho_{i\eta\sigma;i'\eta'\sigma'}(\mathbf{k}). \qquad \text{(E7)}$$

In Eq. (E6) and Eq. (E7), we have introduced the following tensor

$$\mathcal{J}_{i_1\eta_1\sigma_1;i_2\eta_2\sigma_2;i_3\eta_3\sigma_3;i_4\eta_4\sigma_4} = -\frac{J}{2} \sum_{\substack{\alpha,\alpha'=1 \\ \eta,\eta'}}^{2} \left[\eta\eta' + (-1)^{\alpha+\alpha'} \right] \delta_{(\alpha+4)i_1} \delta_{(\alpha'+4)i_2} \delta_{(\alpha'+2)i_3} \delta_{(\alpha+2)i_4} \delta_{\eta\eta_1} \delta_{\eta'\eta_2} \delta_{\eta'\eta_3} \delta_{\eta\eta_4} \delta_{\sigma_1\sigma_4} \delta_{\sigma_2\sigma_3}$$

$$- \frac{J}{4} \sum_{\substack{\alpha,\alpha'=1 \\ \eta,\eta'}}^{2} \left[\eta\eta' - (-1)^{\alpha+\alpha'} \right] \delta_{(\alpha+4)i_1} \delta_{(\alpha'+2)i_2} \delta_{(\alpha'+4)i_3} \delta_{(\alpha+2)i_4} \delta_{\eta\eta_1} \delta_{\eta'\eta_2} \delta_{\eta'\eta_3} \delta_{\eta\eta_4} \delta_{\sigma_1\sigma_4} \delta_{\sigma_2\sigma_3}$$

$$- \frac{J}{4} \sum_{\substack{\alpha,\alpha'=1 \\ \eta,\eta'}}^{2} \left[\eta\eta' - (-1)^{\alpha+\alpha'} \right] \delta_{(\alpha+4)i_2} \delta_{(\alpha'+2)i_1} \delta_{(\alpha'+4)i_4} \delta_{(\alpha+2)i_3} \delta_{\eta\eta_1} \delta_{\eta'\eta_2} \delta_{\eta'\eta_3} \delta_{\eta\eta_4} \delta_{\sigma_1\sigma_4} \delta_{\sigma_2\sigma_3}, \qquad \text{(E8)}$$

which encodes the $\hat{H}_J$ and $\hat{H}_{\tilde{J}}$ interaction terms of the THF Hamiltonian [16]. The mean field Hamiltonian from Eq. (E5) corresponds to the Hartree-Fock decoupling of the $\hat{H}_U$, $\hat{H}_W$, $\hat{H}_J$, and $\hat{H}_{\tilde{J}}$, interaction terms of the THF Hamiltonian (wherein the nearest-neighbor f-electron repulsion U_2 is ignored), as well as to the $\hat{H}_V$ term decoupled only the in Hartree channel. The exclusion of the Fock channel in $\hat{H}_V$ aligns with both Ref. [16] and the methodology used in the DMFT simulations. Finally, the constant term in Eq. E7 simply results in a shift of the Hartree-Fock charge excitation bands. Therefore, it can be disregarded in our subsequent discussions

The *total* mean field Hamiltonian is obtained by summing the single-particle Hamiltonian and the Hartree-Fock interaction one, $H_{\mathrm{MF}} = \hat{H}_0 + H_{I,\mathrm{MF}}$, with the corresponding matrix reading as

$$h_{i\eta\sigma;i'\eta'\sigma'}^{\mathrm{MF}}(\mathbf{k}) = h_{ii'}^{\eta}(\mathbf{k}) \, \delta_{\eta\eta'} \delta_{\sigma\sigma'} + h_{i\eta\sigma;i'\eta'\sigma'}^{I,\mathrm{MF}}(\mathbf{k}), \qquad \text{(E9)}$$

such that

$$H_{\mathrm{MF}} = \sum_{\mathbf{k}} \sum_{\substack{i,\eta,\sigma \\ i',\eta',\sigma'}} h_{i\eta\sigma;i'\eta'\sigma'}^{\mathrm{MF}}(\mathbf{k}) \, \gamma_{\mathbf{k},i,\eta,s}^{\dagger} \gamma_{\mathbf{k},i',\eta',s'}. \qquad \text{(E10)}$$

Finally, we note that at self-consistency, the Hartree-Fock Hamiltonian and the density matrix are related by [203]

$$\varrho^{T}(\mathbf{k}) = \left\{ \exp\left[\beta\left(h^{\mathrm{MF}}(\mathbf{k}) - \mu\mathbb{1} \right) \right] + \mathbb{1} \right\}^{-1} - \frac{1}{2}\mathbb{1}, \qquad \text{(E11)}$$

where $\mathbb{1}$ denotes the identity matrix, $\beta = 1/T$ is the inverse temperature, and μ is the chemical potential of the system.

3. Density matrix symmetrization

In this section, we are interested in obtaining the phase diagrams of the correlated insulators discussed in Eq. (D1) at finite temperature and doping. Similarly to the DMFT simulations, the density matrix away from integer filling

can be obtained by gradually doping the integer-filled self-consistent solution in small increments, as will be explained in section E 4. To ensure the consistency with the partial symmetrization employed in the DMFT simulations, as explained in section D 1, the density matrices of both the doped and undoped correlated insulators will be symmetrized according to the symmetries of the corresponding integer-filled parent states, as will be explained in detail below. In section D 1, a natural basis was constructed for each of the three correlated insulators from Eq. (D1). When computing the self-energy of the doped symmetry-broken phases, a reduced symmetrization was performed on the self-energy, such that the latter is diagonal in the natural basis of the corresponding parent state. In this section, we also offer a justification for this *ad-hoc* symmetrization procedure, and show that it arises naturally if one requires that the doped correlated phases obey the symmetries of the undoped parent states.

We start by analyzing the symmetries of the correlated insulators from Eq. (D1). Before doing so, it is useful to define a number of symmetry operators. The generators of the spin-SU (2) symmetry of the system are given by

$$\hat{S}_\mu = \sum_{\mathbf{k}} \sum_{\substack{i_1,\eta_1,\sigma_1 \\ i_2,\eta_2,\sigma_2}} \left[D\left(\hat{S}_\mu\right)\right]_{i_1\eta_1\sigma_1;i_2\eta_2\sigma_2} \gamma^\dagger_{\mathbf{k},i_1,\eta_1,\sigma_1} \gamma_{\mathbf{k},i_2,\eta_2,\sigma_2}, \quad \text{for} \quad \mu = x,y,z, \tag{E12}$$

with $D\left(\hat{S}_\mu\right) = D^c\left(\hat{S}_\mu\right) \oplus D^f\left(\hat{S}_\mu\right)$ and

$$D^c\left(\hat{S}_\mu\right) = \sigma_0\tau_0\zeta_\mu \oplus \sigma_0\tau_0\zeta_\mu, \quad D^f\left(\hat{S}_\mu\right) = \sigma_0\tau_0\zeta_\mu, \quad \text{for} \quad \mu = x,y,z. \tag{E13}$$

Similarly, the valley U (1) rotation is generated by

$$\hat{V}_{\mathrm{U}(1)} = \sum_{\mathbf{k}} \sum_{\substack{i_1,\eta_1,\sigma_1 \\ i_2,\eta_2,\sigma_2}} \left[D\left(\hat{V}_{\mathrm{U}(1)}\right)\right]_{i_1\eta_1\sigma_1;i_2\eta_2\sigma_2} \gamma^\dagger_{\mathbf{k},i_1,\eta_1,\sigma_1} \gamma_{\mathbf{k},i_2,\eta_2,\sigma_2}, \tag{E14}$$

where $D\left(\hat{V}_{\mathrm{U}(1)}\right) = D^c\left(\hat{V}_{\mathrm{U}(1)}\right) \oplus D^f\left(\hat{V}_{\mathrm{U}(1)}\right)$ and

$$D^c\left(\hat{V}_{\mathrm{U}(1)}\right) = \sigma_0\tau_0\zeta_\mu \oplus \sigma_0\tau_z\zeta_0, \quad D^f\left(\hat{V}_{\mathrm{U}(1)}\right) = \sigma_0\tau_z\zeta_0. \tag{E15}$$

We also define the (spinless) unitary threefold rotation C_{3z}, twofold rotation C_{2z}, as well as the (spinless) antiunitary time-reversal T and Kramers K symmetry operators, such that

$$g\gamma^\dagger_{\mathbf{k},i,\eta,\sigma}g^{-1} = \sum_{i',\eta',\sigma'} \gamma^\dagger_{g\mathbf{k},i',\eta',\sigma'} \left[D\left(g\right)\right]_{i'\eta'\sigma';i\eta\sigma}, \quad \text{for} \quad g = C_{3z}, C_{2z}, T, K, \tag{E16}$$

for which the representation matrices are given by $D\left(g\right) = D^c\left(g\right) \oplus D^f\left(g\right)$, with

$$D^c\left(C_{3z}\right) = e^{\frac{2\pi i}{3}\sigma_z\tau_z\zeta_0} \oplus \sigma_0\tau_0\zeta_0, \qquad D^f\left(C_{3z}\right) = e^{\frac{2\pi i}{3}\sigma_z\tau_z\zeta_0} \tag{E17}$$

$$D^c\left(C_{2z}\right) = \sigma_x\tau_x\zeta_0 \oplus \sigma_x\tau_x\zeta_0, \qquad D^f\left(C_{2z}\right) = \sigma_x\tau_x\zeta_0 \tag{E18}$$

$$D^c\left(T\right) = \sigma_0\tau_x\zeta_0 \oplus \sigma_0\tau_x\zeta_0, \qquad D^f\left(T\right) = \sigma_0\tau_x\zeta_0 \tag{E19}$$

$$D^c\left(K\right) = -i\left(\sigma_0\tau_y\zeta_0 \oplus \sigma_0\tau_y\zeta_0\right), \qquad D^f\left(K\right) = -i\sigma_0\tau_y\zeta_0. \tag{E20}$$

Finally, we introduce five symmetry operations which act in specific spin-valley flavors. We define a Kramers and a twofold rotation symmetry operator acting only in the spin $\sigma =\uparrow$ sector, a time-reversal symmetry operator acting in spin $\sigma =\downarrow$ sector, as well as a $C_{2z}T$ symmetry operator acting only in the spin $\sigma =\downarrow$ and valley $\eta = -$ sector, whose actions on the γ-fermions are given, respectively, by

$$K_\uparrow \gamma^\dagger_{\mathbf{k},i,\eta,\sigma} K_\uparrow^{-1} = \begin{cases} \sum_{i',\eta'} \gamma^\dagger_{-\mathbf{k},i',\eta',\uparrow} \left[D\left(K\right)\right]_{i'\eta'\uparrow;i\eta\uparrow}, & \text{if} \quad \sigma =\uparrow \\ \gamma^\dagger_{\mathbf{k},i,\eta,\sigma}, & \text{if} \quad \sigma =\downarrow \end{cases}, \tag{E21}$$

$$\left[C_{2z}\right]_\uparrow \gamma^\dagger_{\mathbf{k},i,\eta,\sigma} \left[C_{2z}\right]_\uparrow^{-1} = \begin{cases} \sum_{i',\eta'} \gamma^\dagger_{-\mathbf{k},i',\eta',\uparrow} \left[D\left(C_{2z}\right)\right]_{i'\eta'\uparrow;i\eta\uparrow}, & \text{if} \quad \sigma =\uparrow \\ \gamma^\dagger_{\mathbf{k},i,\eta,\sigma}, & \text{if} \quad \sigma =\downarrow \end{cases}, \tag{E22}$$

$$\left[T\right]_\downarrow \gamma^\dagger_{\mathbf{k},i,\eta,\sigma} \left[T\right]_\downarrow^{-1} = \begin{cases} \sum_{i',\eta'} \gamma^\dagger_{-\mathbf{k},i',\eta',\downarrow} \left[D\left(T\right)\right]_{i'\eta'\downarrow;i\eta\downarrow}, & \text{if} \quad \sigma =\downarrow \\ \gamma^\dagger_{\mathbf{k},i,\eta,\sigma}, & \text{if} \quad \sigma =\uparrow \end{cases}, \tag{E23}$$

$$\left[C_{2z}T\right]_{\downarrow,-} \gamma^\dagger_{\mathbf{k},i,\eta,\sigma} \left[C_{2z}T\right]_{\downarrow,-}^{-1} = \begin{cases} \sum_{i'} \gamma^\dagger_{\mathbf{k},i',-,\downarrow} \left[D\left(C_{2z}T\right)\right]_{i'-\downarrow;i-\downarrow}, & \text{if} \quad \sigma =\downarrow \quad \text{and} \quad \eta = - \\ \gamma^\dagger_{\mathbf{k},i,\eta,\sigma}, & \text{otherwise} \end{cases}, \tag{E24}$$

where $D(C_{2z}T) = D(C_{2z})D(T)$. Additionally, we define a valley U(1) rotation operator acting only on the spin $\sigma = \downarrow$ sector

$$\left[\hat{V}_{\mathrm{U}(1)}\right]_{\downarrow} = \sum_{\mathbf{k}} \sum_{\substack{i_1,\eta_1 \\ i_2,\eta_2}} \left[D\left(\hat{V}_{\mathrm{U}(1)}\right)\right]_{i_1\eta_1\downarrow;i_2\eta_2\downarrow} \gamma^{\dagger}_{\mathbf{k},i_1,\eta_1,\downarrow}\gamma_{\mathbf{k},i_2,\eta_2,\downarrow}. \tag{E25}$$

With the symmetry operators at hand, we now consider the symmetry-broken phases of the THF model at the Hartree-Fock level. In analogy with the DMFT simulations, in our finite-temperature Hartree-Fock simulations, we will ignore any correlations between f-electrons belonging to different lattice sites. As a result, for a given correlated phase of the THF model characterized by the density matrix $\varrho_{i\eta\sigma;i'\eta'\sigma'}(\mathbf{k})$, the f-electron block will be $\mathbf{k}$-independent and given by

$$\varrho_{(\alpha+4)\eta\sigma;(\alpha'+4)\eta'\sigma'}(\mathbf{k}) = O^f_{\alpha\eta\sigma;\alpha'\eta'\sigma'}, \quad \text{for} \quad 1 \leq \alpha, \alpha' \leq 2. \tag{E26}$$

Moreover, if we assume that the corresponding correlated phase is symmetric under the crystalline symmetry g or is invariant under a continuous symmetry generated by g, then its density matrix will obey the following constraint

$$\varrho_{i_1\eta_1\sigma_1;i_2\eta_2\sigma_2}(\mathbf{k}) = \sum_{\substack{i_3,\eta_3,\sigma_3 \\ i_4,\eta_4,\sigma_4}} [D(g)]_{i_3\eta_3\sigma_3;i_1\eta_1\sigma_1}\,\varrho^{(*)}_{i_3\eta_3\sigma_3;i_4\eta_4\sigma_4}(g\mathbf{k})\,[D(g)]^{*}_{i_4\eta_4\sigma_4;i_2\eta_2\sigma_2}, \tag{E27}$$

where $g\mathbf{k} = \mathbf{k}$ if g is a continuous symmetry and $^{(*)}$ denotes complex conjugation whenever g is antiunitary.

As will be explained in section E 4, the correlated phases at finite doping can be obtained by doping into the charge-one excitation bands of an integer-filled insulator, then recalculating the self-consistent solution for that particular non-integer filling. We note that each integer-filled correlated insulator state breaks some of the symmetries of the system while retaining others. In principle, as the integer-filled solution is gradually doped, the system can undergo further symmetry-breaking transitions at fractional fillings. To prevent this scenario, our calculations for the doped correlated insulators ensure that the remaining symmetries of the corresponding integer-filled state *persist* even in the doped phase. Practically, this is achieved by imposing the symmetry constraint from Eq. (E27) for every symmetry of the undoped insulator at the level of the f-electron density matrix of the doped phase.

In what follows, we will individually discuss the unbroken symmetries for each of the correlated insulators from Eq. (D1). We will also show that by imposing these symmetries in the corresponding doped phases, the f-electron block of the density matrix both *at* and *away* from integer filling becomes diagonal in the natural bases introduced in section D 1.

a. The $\nu = 0$ K-IVC state

The $\nu = 0$ K-IVC correlated insulator state from Eq. (D1) is symmetric under the C_{3z}, C_{2z}, spin SU(2), and K symmetries. As a result, through Eq. (E27), we will require that the correlated phases obtained by doping it away from integer filling have the following f-electron block in their density matrices

$$O^f = a_1\sigma_0\tau_0\zeta_0 + a_2\sigma_y\tau_y\zeta_0, \quad \text{with} \quad a_1, a_2 \in \mathbb{R}. \tag{E28}$$

We note that if we cast the f-electron density matrix in the natural basis of the $\nu = 0$ K-IVC state introduced in section D 1,

$$\left(\tilde{f}^{\dagger}_{\mathbf{k},1,+,\uparrow}, \tilde{f}^{\dagger}_{\mathbf{k},2,+,\uparrow}, \tilde{f}^{\dagger}_{\mathbf{k},1,+,\downarrow}, \tilde{f}^{\dagger}_{\mathbf{k},2,+,\downarrow}, \tilde{f}^{\dagger}_{\mathbf{k},1,-,\uparrow}, \tilde{f}^{\dagger}_{\mathbf{k},2,-,\uparrow}, \tilde{f}^{\dagger}_{\mathbf{k},1,-,\downarrow}, \tilde{f}^{\dagger}_{\mathbf{k},2,-,\downarrow}\right), \tag{E29}$$

the resulting density matrix has the following form

$$\tilde{O}^f = \mathrm{diag}\left([a'_1, a'_1, a'_1, a'_1, a'_2, a'_2, a'_2, a'_2]\right), \quad \text{with} \quad a'_1, a'_2 \in \mathbb{R}. \tag{E30}$$

By transforming to the natural basis, we enforce the density matrix of the f-electrons to take the form given in Eq. E30, thus ensuring that all the remaining symmetries preserved by the parent $\nu = 0$ K-IVC insulator are also preserved in the non-integer correlated phases obtained by doping it.

b. The $\nu = -1$ K-IVC+VP state

The case of the $\nu = -1$ K-IVC+VP state requires a slightly more involved analysis. We note that the parent state (the $\nu = -1$ K-IVC+VP state) we consider here still has C_{3z} and spin $\hat{S}_z$ symmetries. When computing the self-consistent solutions of the correlated phases obtained by doping it away from integer filling, we will impose these symmetries (C_{3z} and $\hat{S}_z$) to the corresponding density matrices. In doing so, we ensure that the unbroken symmetries of the integer-filled $\nu = -1$ K-IVC+VP insulator persist in the correlated phases obtained by doping it. This then leads to two constraints on the density matrix according to Eq. (E27) and also implies that the density matrix is spin-diagonal. Additionally, the spin $\sigma = \uparrow$ sector has K and C_{2z} symmetry (meaning that the correlated insulator as a whole has $K_\uparrow$ and $[C_{2z}]_\uparrow$ symmetries), which requires that its density matrix obeys

$$\varrho_{i_1\eta_1\uparrow;i_2\eta_2\uparrow}(\mathbf{k}) = \sum_{\substack{i_3,\eta_3 \\ i_4,\eta_4}} [D(K)]_{i_3\eta_3\uparrow;i_1\eta_1\uparrow}\, \varrho^*_{i_3\eta_3\uparrow;i_4\eta_4\uparrow}(-\mathbf{k})\, [D(K)]^*_{i_4\eta_4\uparrow;i_2\eta_2\uparrow}, \tag{E31}$$

$$\varrho_{i_1\eta_1\uparrow;i_2\eta_2\uparrow}(\mathbf{k}) = \sum_{\substack{i_3,\eta_3 \\ i_4,\eta_4}} [D(C_{2z})]_{i_3\eta_3\uparrow;i_1\eta_1\uparrow}\, \varrho_{i_3\eta_3\uparrow;i_4\eta_4\uparrow}(-\mathbf{k})\, [D(C_{2z})]^*_{i_4\eta_4\uparrow;i_2\eta_2\uparrow}. \tag{E32}$$

The spin $\sigma = \downarrow$ sector features valley U(1) symmetry, which implies that the correlated insulator is symmetric under the continuous symmetry generated by the $\left[\hat{V}_{\mathrm{U}(1)}\right]_\downarrow$ operator and that its density matrix obeys

$$\varrho_{i_1\eta_1\downarrow;i_2\eta_2\downarrow}(\mathbf{k}) = \sum_{\substack{i_3,\eta_3 \\ i_4,\eta_4}} \left[D\left(\left[\hat{V}_{\mathrm{U}(1)}\right]_\downarrow\right)\right]_{i_3\eta_3\downarrow;i_1\eta_1\downarrow} \varrho_{i_3\eta_3\downarrow;i_4\eta_4\downarrow}(\mathbf{k})\left[D\left(\left[\hat{V}_{\mathrm{U}(1)}\right]_\downarrow\right)\right]^*_{i_4\eta_4\downarrow;i_2\eta_2\downarrow}, \tag{E33}$$

thus being valley-diagonal in the spin $\sigma = \downarrow$ sector. Finally, the spin-valley sector corresponding to $\sigma = \downarrow$ and $\eta = -$ also features $C_{2z}T$ symmetry. The $\nu = -1$ K-IVC+VP correlated insulator is thus symmetric under $[C_{2z}T]_{\downarrow,-}$, which implies that its density matrix obeys

$$\varrho_{i_1-\downarrow;i_2-\downarrow}(\mathbf{k}) = \sum_{i_3,i_4} \left[D\left([C_{2z}T]_{\downarrow,-}\right)\right]_{i_3-\downarrow;i_1-\downarrow} \varrho^*_{i_3-\downarrow;i_4-\downarrow}(\mathbf{k})\left[D\left([C_{2z}T]_{\downarrow,-}\right)\right]^*_{i_4-\downarrow;i_2-\downarrow}. \tag{E34}$$

In practice, we require that the correlated phases obtained by doping the $\nu = -1$ K-IVC+VP insulator preserve the remaining symmetries of the corresponding integer-filled state. This implies that the constraints from Eq. (E31), Eq. (E32), Eq. (E33), and Eq. (E34) must hold for the density matrices of the doped phases, which will then assume the following form in the f-block

$$O^f_{\alpha\eta\uparrow;\alpha'\eta'\downarrow} = O^f_{\alpha\eta\downarrow;\alpha'\eta'\uparrow} = 0, \tag{E35}$$

$$O^f_{\alpha\eta\uparrow;\alpha'\eta'\uparrow} = [a_1\sigma_0\tau_0 + a_2\sigma_y\tau_y]_{\alpha\eta;\alpha'\eta'}, \tag{E36}$$

$$O^f_{\alpha+\downarrow;\alpha'+\downarrow} = [a_3\sigma_0 + a_4\sigma_z]_{\alpha\eta;\alpha'\eta'}, \tag{E37}$$

$$O^f_{\alpha-\downarrow;\alpha'-\downarrow} = a_5\,[\sigma_0]_{\alpha\eta;\alpha'\eta'}, \tag{E38}$$

$$O^f_{\alpha+\downarrow;\alpha'-\downarrow} = O^f_{\alpha-\downarrow;\alpha'+\downarrow} = 0, \tag{E39}$$

where $a_i \in \mathbb{R}$, $(1 \leq i \leq 5)$. In the natural basis of the $\nu = -1$ K-IVC+VP state introduced in section D 1,

$$\left(\tilde{f}^\dagger_{\mathbf{k},1,+,\uparrow}, \tilde{f}^\dagger_{\mathbf{k},2,+,\uparrow}, \tilde{f}^\dagger_{\mathbf{k},1,-,\uparrow}, \tilde{f}^\dagger_{\mathbf{k},2,-,\uparrow}, f^\dagger_{\mathbf{k},1,+,\downarrow}, f^\dagger_{\mathbf{k},2,+,\downarrow}, f^\dagger_{\mathbf{k},1,-,\downarrow}, f^\dagger_{\mathbf{k},2,-,\downarrow}\right), \tag{E40}$$

the f-electron density matrix of both the $\nu = -1$ K-IVC+VP insulator and of the phases obtained by doping it will have the following form

$$\tilde{O}^f = \mathrm{diag}\left([a_1', a_1', a_2', a_2', a_3', a_4', a_5', a_5']\right), \quad \text{with} \quad a_i' \in \mathbb{R}, \quad \text{for} \quad 1 \leq i \leq 5. \tag{E41}$$

c. The $\nu = -2$ K-IVC+VP state

Similarly to the $\nu = -1$ K-IVC+VP state, the $\nu = -2$ K-IVC state features C_{3z} and spin-$\hat{S}_z$ symmetries, thus being spin-diagonal. The latter also features C_{2z} symmetry in both spin sectors. These three symmetries constrain

the density matrix according to Eq. (E27). Additionally, the $\nu = -2$ K-IVC state features $\left[\hat{V}_{\mathrm{U(1)}}\right]_\downarrow$ and $T_\downarrow$ symmetries which imply that

$$\varrho_{i_1\eta_1\downarrow;i_2\eta_2\downarrow}\left(\mathbf{k}\right) = \sum_{\substack{i_3,\eta_3 \\ i_4,\eta_4}} \left[D\left(\left[\hat{V}_{\mathrm{U(1)}}\right]_\downarrow\right)\right]_{i_3\eta_3\downarrow;i_1\eta_1\downarrow} \varrho_{i_3\eta_3\downarrow;i_4\eta_4\downarrow}\left(\mathbf{k}\right)\left[D\left(\left[\hat{V}_{\mathrm{U(1)}}\right]_\downarrow\right)\right]^*_{i_4\eta_4\downarrow;i_2\eta_2\downarrow}, \tag{E42}$$

$$\varrho_{i_1\eta_1\downarrow;i_2\eta_2\downarrow}\left(\mathbf{k}\right) = \sum_{\substack{i_3,\eta_3 \\ i_4,\eta_4}} \left[D\left(T_\downarrow\right)\right]_{i_3\eta_3\downarrow;i_1\eta_1\downarrow} \varrho^*_{i_3\eta_3\downarrow;i_4\eta_4\downarrow}\left(-\mathbf{k}\right)\left[D\left(T_\downarrow\right)\right]^*_{i_4\eta_4\downarrow;i_2\eta_2\downarrow}. \tag{E43}$$

As a result, the density matrix of the $\nu = -2$ K-IVC state, as well as of the correlated phases obtained by doping it away from integer fillings must have the following parameterization of their f-electron block

$$O^f_{\alpha\eta\uparrow;\alpha'\eta'\downarrow} = O^f_{\alpha\eta\downarrow;\alpha'\eta'\uparrow} = 0, \tag{E44}$$

$$O^f_{\alpha\eta\uparrow;\alpha'\eta'\uparrow} = \left[a_1\sigma_0\tau_0 + a_2\sigma_y\tau_y\right]_{\alpha\eta;\alpha'\eta'}, \tag{E45}$$

$$O^f_{\alpha\eta\downarrow;\alpha'\eta'\downarrow} = a_3\left[\sigma_0\tau_0\right]_{\alpha\eta;\alpha'\eta'}, \tag{E46}$$

for $a_1, a_2, a_3 \in \mathbb{R}$. In the natural basis of the $\nu = -2$ K-IVC state from D 1,

$$\left(\tilde{f}^\dagger_{\mathbf{k},1,+,\uparrow}, \tilde{f}^\dagger_{\mathbf{k},2,+,\uparrow}, \tilde{f}^\dagger_{\mathbf{k},1,-,\uparrow}, \tilde{f}^\dagger_{\mathbf{k},2,-,\uparrow}, f^\dagger_{\mathbf{k},1,+,\downarrow}, f^\dagger_{\mathbf{k},2,+,\downarrow}, f^\dagger_{\mathbf{k},1,-,\downarrow}, f^\dagger_{\mathbf{k},2,-,\downarrow}\right), \tag{E47}$$

the f-electron density matrix is given by

$$\tilde{O}^f = \mathrm{diag}\left(\left[a'_1, a'_1, a'_2, a'_2, a'_3, a'_3, a'_3, a'_3\right]\right), \quad \text{with} \quad a'_1, a'_2, a'_3 \in \mathbb{R}. \tag{E48}$$

4. Self-consistent solution

To obtain the self-consistent density matrix for a given correlated insulator at integer filling ν_0, we start from an initial guess of the density matrix

$$\varrho^{(0)}_{i\eta\sigma;i'\eta'\sigma'}\left(\mathbf{k}\right) = \begin{cases} \rho^0_{(i-4)\eta\sigma;(i'-4)\eta'\sigma'} - \frac{1}{2}\delta_{ii'}\delta_{\eta\eta'}\delta_{\sigma\sigma'} & \text{if} \quad 5 \leq i, i' \leq 6 \\ 0 & \text{otherwise} \end{cases}. \tag{E49}$$

For the correlated phases obtained by doping the integer-filled insulator, we use a pre-computed density matrix at a nearby integer filling, as will be explained below. Starting from the initial condition, we iterate the following Hartree-Fock algorithm whereby a new density matrix $\varrho^{(n+1)}_{i\eta\sigma;i'\eta'\sigma'}\left(\mathbf{k}\right)$ can be obtained from the density matrix at the n-th step, $\varrho^{(n)}_{i\eta\sigma;i'\eta'\sigma'}\left(\mathbf{k}\right)$. The Hartree-Fock self-consistent loop can be summarized as follows:

1. Using $\varrho^{(n)}_{i\eta\sigma;i'\eta'\sigma'}\left(\mathbf{k}\right)$, we construct the Hartree-Fock Hamiltonian at the n-th step according to Eq. (E9).

2. The Hartree-Fock Hamiltonian is diagonalized as

$$\sum_{i',\eta',\sigma'} h^{\mathrm{MF}}_{i\eta\sigma;i'\eta'\sigma'}\left(\mathbf{k}\right)\varphi_{m;i'\eta'\sigma'}\left(\mathbf{k}\right) = \epsilon_m\left(\mathbf{k}\right)\varphi_{m;i\eta\sigma}\left(\mathbf{k}\right), \tag{E50}$$

with $\epsilon_m\left(\mathbf{k}\right)$ and $\varphi_{m;i'\eta'\sigma'}\left(\mathbf{k}\right)$ denoting the m-th Hartree-Fock energy and eigenvector. A new density matrix is then constructed according to

$$\varrho'_{i\eta s;i'\eta's'}\left(\mathbf{k}\right) = \sum_m \frac{1}{e^{\beta(\epsilon_m(\mathbf{k})-\mu)} + 1}\varphi^*_{m;i\eta s}\left(\mathbf{k}\right)\varphi_{m;i'\eta's'}\left(\mathbf{k}\right), \tag{E51}$$

where the chemical potential μ is fixed by requiring that the total filling of the system ν equals the desired value.

3. The new density matrix $\varrho'_{i\eta s;i'\eta's'}(\mathbf{k})$ will not generically have a $\mathbf{k}$-independent f-electron block with the correct parameterization, as derived in section E 3. This is because the f-c hybridization of the single-particle THF Hamiltonian is $\mathbf{k}$-dependent. We seek solutions where the f-electrons at different sites are uncorrelated, meaning that the f-electron block of the corresponding density matrix is $\mathbf{k}$-independent. To drop the $\mathbf{k}$-dependency of the density matrix in the f-block, we now replace the f-electron density matrix at different $\mathbf{k}$ points by its average across the BZ

$$O'^f_{\alpha\eta\sigma;\alpha'\eta'\sigma'} \equiv \left[\frac{1}{N_M} \sum_{\mathbf{k}'} \varrho'_{(\alpha+4)\eta s;(\alpha'+4)\eta's'}(\mathbf{k}') \right], \quad \text{for} \quad 1 \leq \alpha, \alpha' \leq 2 \tag{E52}$$

$$\varrho'_{(\alpha+4)\eta\sigma;(\alpha'+4)\eta'\sigma'}(\mathbf{k}) \to O'^f_{\alpha\eta\sigma;\alpha'\eta'\sigma'}, \quad \text{for} \quad 1 \leq \alpha, \alpha' \leq 2, \quad \text{and any} \quad \mathbf{k}. \tag{E53}$$

4. Although $\mathbf{k}$-independent, the f-electron block of the new density matrix, $O'^f_{\alpha\eta\sigma;\alpha'\eta'\sigma'}$, will not generically obey the remaining symmetries of the correlated phase from which it was obtained. For example, the correlated phase at $\nu = -0.1$ is obtained by doping the $\nu = 0$ K-IVC state and, per our assumptions around Eq. (E27), should obey the remaining symmetries of the K-IVC state discussed in section E 3 a. With infinite precision arithmetic, if the density matrix at the beginning of the self-consistent step $\varrho^{(n)}(\mathbf{k})$ obeys some of the symmetries of the THF model, then the corresponding mean field Hamiltonian $h^{\text{MF}}(\mathbf{k})$ and, consequently, the new density matrix $\varrho'(\mathbf{k})$ should obey the same symmetries. However, in finite precision arithmetic, $\varrho'(\mathbf{k})$ will only obey these symmetries *approximately*. Over the course of many iterations, these small errors would grow leading to the self-consistent solution for $\nu = -0.1$ *not* obeying the symmetries of the $\nu = 0$ K-IVC state.

To prevent these numerical instabilities, we will require that $O'^f_{\alpha\eta\sigma;\alpha'\eta'\sigma'}$ has the correct symmetry-enforced parameterization at every Hartree-Fock step. For example, when computing the order parameter of the $\nu = -0.1$ correlated phase, we impose the parameterization in Eq. (E28) as follows

$$a_1 \equiv \frac{1}{8} \text{Tr} \left[\sigma_0 \tau_0 \zeta_0 O'^f \right], \quad a_2 \equiv \frac{1}{8} \text{Tr} \left[\sigma_y \tau_y \zeta_0 O'^f \right], \tag{E54}$$

$$O'^f \to a_1 \sigma_0 \tau_0 \zeta_0 + a_2 \sigma_y \tau_y \zeta_0, \tag{E55}$$

which then leads to the new density matrix

$$\varrho^{(n+1)}_{i\eta\sigma;i'\eta'\sigma'}(\mathbf{k}) = \begin{cases} O'^f_{\alpha\eta\sigma;\alpha'\eta'\sigma'} & \text{if} \quad 5 \leq i, i' \leq 6 \\ \varrho'_{i\eta s;i'\eta's'}(\mathbf{k}) & \text{otherwise} \end{cases}. \tag{E56}$$

Similar types of symmetrization are performed for the correlated phases obtained by doping the $\nu = -1$ K-IVC+VP and $\nu = -2$ K-IVC correlated insulator by imposing the corresponding parameterizations derived in sections E 3 b and E 3 c, respectively.

To mitigate fluctuations in the self-consistent iterative algorithm, we use a two-pronged approach for improved convergence. Initially, we employ linear mixing to smooth out oscillations when the algorithm is far from convergence (implying that $\rho^{(n+1)}(\mathbf{k}) \to \frac{1}{2}\rho^{(n)}(\mathbf{k}) + \frac{1}{2}\rho^{(n+1)}(\mathbf{k})$ is performed at the end of each self-consistent step). As the density matrix changes become smaller, we switch to the DIIS convergence acceleration method, as described in Ref. [204]. Convergence is determined by the criterion that the Hartree-Fock Hamiltonian and the density matrix should commute (i.e., $\left[\varrho^T(\mathbf{k}), h^{\text{MF}}(\mathbf{k}) \right] = 0$, up to numerical accuracy), a condition implied by Eq. (E11).

To generate the Hartree-Fock phase diagrams depicted in Fig. 2, we first calculate the self-consistent density matrix for integer-filled correlated insulators at a specific temperature T. Once the self-consistent solution is obtained for an insulator at an integer filling ν_0 and temperature T, we can obtain the symmetry-broken phases in the vicinity of ν_0 by incrementally doping the system and requiring the doped states have the same symmetries as the state at integer filling ν_0. Specifically, we examine fillings of $\nu_0 + n\delta\nu$, where $n \in \mathbb{Z}$ and $|n| \leq \frac{1}{2\delta\nu}$. This means that we incrementally dope the integer-filled correlated insulator by at most $1/2$, using $\delta\nu$ as the step size. To solve for each new filling $\nu_0 + n\delta\nu$, we use the previously computed self-consistent density matrix $\varrho(\mathbf{k})$ at $\nu_0 + (n-1)\delta\nu$ (if $n > 0$) or $\nu_0 + (n+1)\delta\nu$ (if $n < 0$) as initial conditions. In our calculations, we set $\delta\nu = 1/50$.

Finally, we note that for each iteration of the algorithm outlined above, we enforce that the f-electron density matrix, when expressed in the natural basis of the doped correlated insulator, must be proportional to the identity matrix within each set of degenerate elements. These sets are defined as per Eq. (D8). This procedure is equivalent to enforcing that the self-consistent solutions have the same symmetry as our initial parent state or, in other words, have the same symmetry as the correlated state at the corresponding integer filling ν_0. Our numerical checks also confirm that this constraint leads to a self-consistent density matrix that respects the symmetries of its correlated
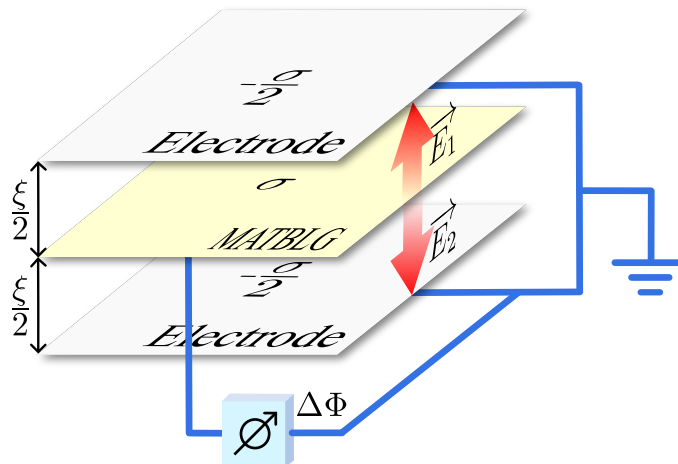
FIG. G.1. Sketch of the MATBLG realization assumed in the Song-Bernevig model, assumed MATBLG in between two capacitor plates.

insulator parent state. This, according to Eq. (E11), ensures that the Hartree-Fock Hamiltonian also adheres to these symmetries.

Specifically, the f-electron component of the Hartree-Fock Hamiltonian, when expressed in the natural basis of the parent correlated insulator, will also be proportional to the identity matrix within each degenerate set, as outlined in Eq. (D8). Furthermore, Eq. (E6) dictates that this Hartree-Fock Hamiltonian will exhibit $\mathbf{k}$-independence in the f-electron block. Consequently, the f-electron block of the self-energy is $\mathbf{k}$-independent, and, when expressed in the natural basis of the parent correlated insulator, is proportional to the identity matrix within each set of degenerate elements. Since the Hartree-Fock Hamiltonian is precisely the static part of the electron self-energy, this implies that within the natural basis, the f-electron static self-energy is proportional to the identity matrix within each degenerate set. This mirrors the partial symmetrization used in the DMFT calculations and outlined in section D 1 which requires that the entire f-electron self-energy (i.e., both the *dynamic* and the *static* parts) are diagonal in the natural basis and proportional to the identity within each set of degenerate elements.

Appendix F: Quasiparticle analysis

The first step in the quasiparticle analysis is to find the zeros of $\hat{H}_{aux}$ defined in (4). We do this using an iterative inflation scheme. We start by evaluating the eigenvalues of $\hat{H}_{aux}$ on the regular centered sampling of the first Brillouin zone as defined in C with `sample_len=20`. We filter the k-points by their smallest eigenvalue, i.e. we sort the k-points by their smallest eigenvalue and keep a fraction of the them. We determine this fraction heuristically. Then we inflate the k-mesh around the selected k-points. This new set of k-points is a finer sampling of a subset of the Brillouin zone within which the zeros are contained. We perform the filtering and inflation procedure iteratively until the smallest eigenvalue of all the filtered k-points falls below a threshold, which we chose to be 0.1 meV.

Appendix G: Chemical potential definition and geometric capacitance

Interacting electron models can contain terms which relate to what is referred to as *geometric capacitance* in experimental contexts. (See for instance the capacitor circuit model detailed in the SI of [175].) Hence, special care has to be taken when comparing chemical potentials, compressibilities or related quantities between different theoretical models and different experimental setups, since geometric capacitance effects have to be consistently treated or consistently cancelled. We explain in the following how to avoid the geometric capacitance contributions in our calculations.

We base our calculations on the Song-Bernevig model from Ref. [16]. The interaction terms in the Song-Bernevig model derive from Coulomb integrals, where TBLG is assumed to be placed in a double gate structure (see Sec. 3A in the SI of [16]), which also contains a geometric capacitance contribution. Specifically, the Coulomb integrals correspond to a geometry, where the TBLG layer is sandwiched by two capacitor plates (see Fig. G.1) and where the total system is charge neutral. The two plates are assumed to be equivalent and equally spaced from the TBLG
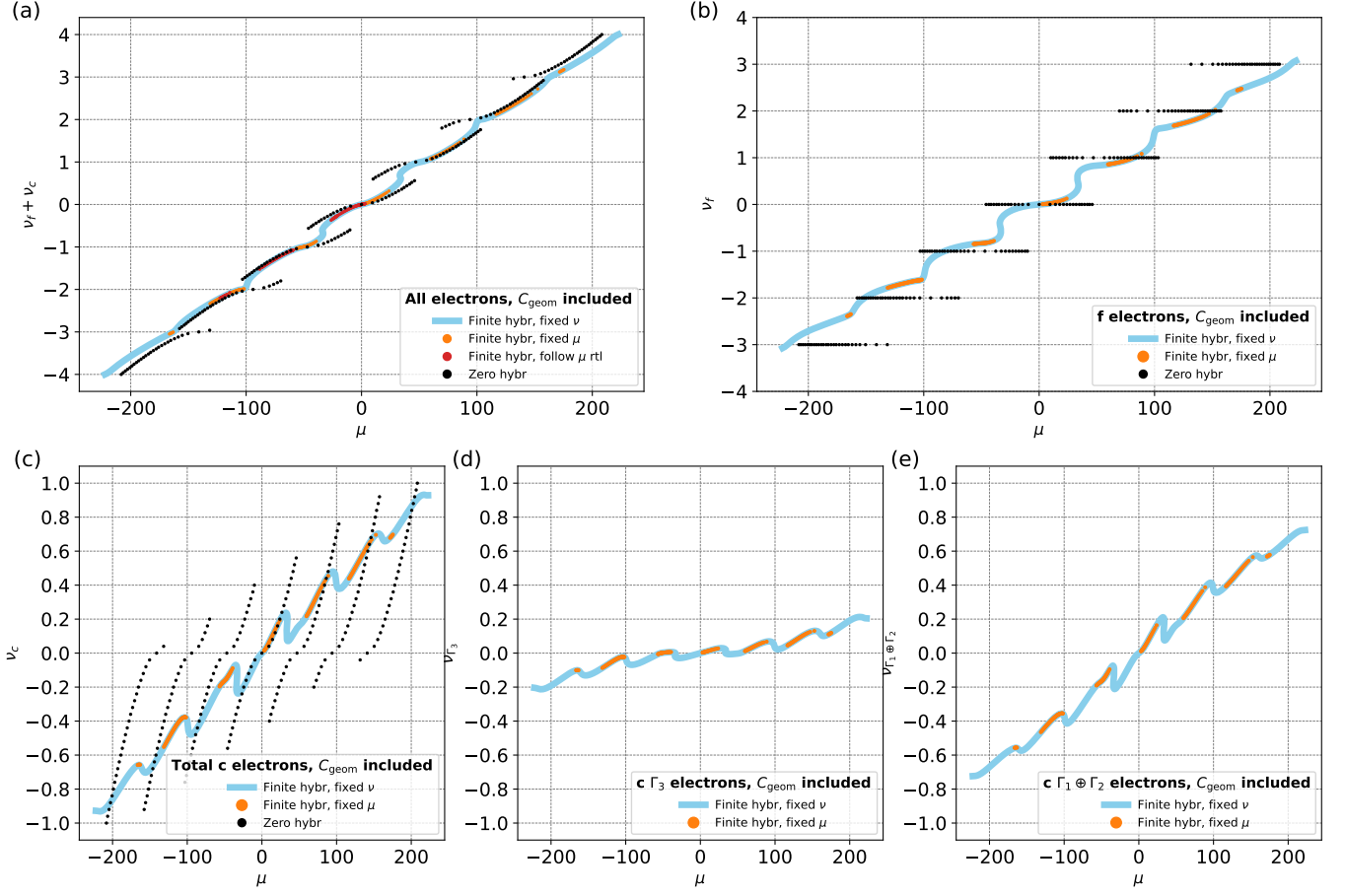
FIG. G.2. Occupation with respect to CNP as a function of the chemical potential, total value (a) and orbital-valley resolved (b-c), for T=11.6 K. The blue curves refer to DMFT simulations tuning the chemical potential to obtain the requested (total) occupation value. The orange curves refer to DMFT simulations performed at fixed chemical potential. The red curve follows the fixed-chemical-potential solution for decreasing value of μ (right-to-left). The black data refer to the zero-hybridization model, solved in [180]. In these plots, the geometrical capacitance contribution is *included* in the value of μ, contrary to Fig. 6 of the main text. It is clear how, the presence of this geometrical term was the cause of the wide negative compressibility regions displayed by the $\nu_f + \nu_c$ curve throughout most of the parameter range. Remarkably, a small region of negative compressibility is however still present around ± 0.6.

layer by a distance of $\xi/2$. If the arbitrarily doped TBLG layer has surface charge σ, each plate possesses charge $-\sigma/2$. The surface charge density corresponding to the filling ν_{tot} is $\frac{\nu e}{\Omega_0}$, where Ω_0 is the area of the moiré unit cell. The voltage between the top plate and the TBLG layer $\Delta\Phi$ is given by $\frac{\sigma}{2\epsilon_0\epsilon_r}\frac{\xi}{2} = \nu_{\text{tot}}\frac{e\xi}{4\Omega_0\epsilon_0\epsilon_r}$ where ϵ_0 and ϵ_r are the vacuum permittivity and the relative permittivity. Ref. [16] assumes $\epsilon_r = 6$ stemming from the hBN encapsulation and $\xi = 10$ nm. The contribution from the geometric capacitance to be subtracted is then

$$e\Delta\Phi = \nu_{\text{tot}}\frac{e^2\xi}{4\Omega_0\epsilon_0\epsilon_r} = \nu_{\text{tot}} \cdot 47\,\text{meV}. \tag{G1}$$

We explain in the following how we have approximately cancelled the geometric contribution according to Eq. G1 in our theoretical framework. In order to apply DMFT to solve the Song-Bernevig model [16], we have split the interaction terms in three categories: the first (H_{U1} term) is dynamically treated, the second (H_W, H_V, H_J terms) is accounted for at the mean-field level and the third (H_{U2} term) is small enough to be neglected. Let us for simplicity restrict ourself to the symmetric case, where $H_{\text{MF}} = H_W + H_V$: since H_W and H_V are density-density terms, apart from constant energy shifts and omitting the indices,

$$H_W = W\left[\nu_f\left(\sum c^\dagger c\right) + \nu_c\left(\sum f^\dagger f\right)\right] \tag{G2}$$
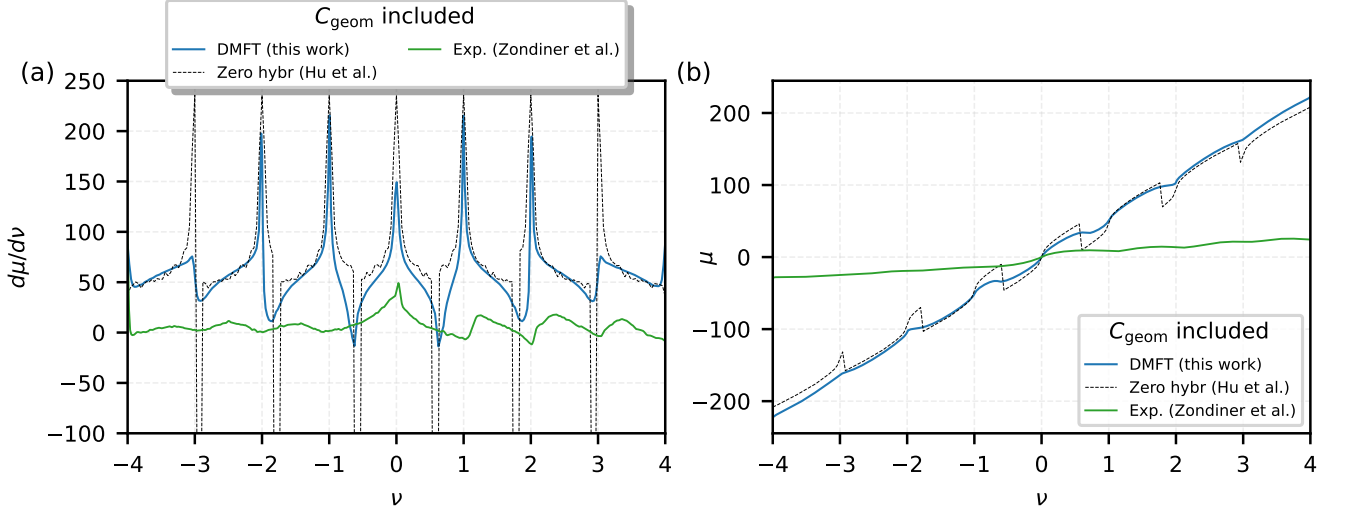
FIG. G.3. (a) Inverse compressibility obtained from the fixed-occupation DMFT simulations for $T = 11.6K$, compared with the experimental data of [175], for $B_{||} = 0$, $T = 4K$ and $\theta = 1.13°$. Here, the geometric capacitance contribution has been taken into account, causing a positive shift of the compressibility values. While the negative spikes of the zero-hybridization solution are still present, such shift is enough make $d\mu/d\nu$ positive except for the small regions around ± 0.6. (b) Chemical potential for DMFT simulations at $T = 11.6K$ compared with [175] data. Again, this scenario is relative to the convention according to which the contributions of the geometric capacitance of the plane-plate capacitor have not been subtracted out. This bad agreement with the green curve from experiments confirms the choice made in the main text with the geometric capacitance contributions to the chemical potential.

$$H_V = V\left[\nu_c\left(\sum c^\dagger c\right)\right] \tag{G3}$$

H_{MF} can equivalently be decomposed in the two following terms

$$H_{\mathrm{tot}} = \left(W\nu_f + V\nu_c\right)\left(\sum f^\dagger f + \sum c^\dagger c\right) = \left(W\nu_f + V\nu_c\right)\hat{N} \tag{G4}$$

$$H_{\mathrm{f}} = \left(W(\nu_f - \nu_c) - V\nu_c\right)\left(\sum f^\dagger f\right) = \left(W(\nu_f - \nu_c) - V\nu_c\right)\hat{n}_f \tag{G5}$$

where $\hat{N}$ and $\hat{n}_f$ are the total and f-subspace occupation number operators respectively.

Remembering that $W \approx V \approx 47 \pm 1$ meV and comparing H_{tot} to the geometric capacitance contribution from Eq. G1, we notice that discarding H_{tot} is equivalent, within 1meV (and hence generating an error smaller than, for example, the exclusion of the H_{U2} interaction term) to cancelling the geometrical capacitance contribution. Hence, we discard H_{tot} and impose $H_{\mathrm{MF}} = H_{\mathrm{f}}$. We refer to the chemical potential derived within this convention as μ. All data show in the manuscript refer to this definition of the chemical potential μ, which can also be directly compared to experiments like [175].

The addition of symmetry-breaking terms such as H_J does not alter this picture, since the total and f-subspace shifts only couple to diagonal entries in the system density matrix.

We could relate μ to the chemical potential μ_1, which would be obtained from treating the Song-Bernevig model without geometric capacitance subtraction. In this case, H_{tot} is to be included leading to

$$\mu_1 = \mu + W\nu_f + V\nu_c. \tag{G6}$$

When the DMFT simulations are performed at fixed density, the chemical potential μ is not set *a priori* as a parameter, but iteratively adjusted as to obtain the desired total occupation.

As stated above, the expression of the mean-field interaction terms via Eq. G4 and G5 has, as a first benefit, the peculiarity of isolating a term (H_{tot}) which is to all intents and purposes equivalent to the geometric capacitance $e\Delta\Phi$. It also comes with a relevant computational advantage: instead of dealing with two different energy shifts for the f- and c-subspaces, to be self-consistently determined at every DMFT loop, we now effectively consider

only one shift restricted to the f-subspace, and hence analogous to the usual double-counting corrections typical of DFT+DMFT calculations [205–207]. Moreover, the overall energy shift is calculated in one single operation upon self-consistently adjusting μ, without calculating H_{tot}. This avoids convergence instabilities due to the oscillations of ν_f and ν_c.

It is instructive to look at the filling-vs-μ and inverse compressibilty data when the geometrical capacitance contribution is not subtracted out (see Figs. G.2 and G.3). Regarding the inverse compressibilities (cfr. Fig.7 in the main text), while the huge negative spikes of the zero-hybridization solution are obviously hardly affected, the negative inverse compressibility regions in the DMFT curve have almost disappeared. Relatedly, the filling data of Fig. G.2 acquire a sizable horizontal offset, with the value of μ now varying in a range roughly ten times bigger than the one in Fig. 6 in the main text. The f orbitals get filled up in an almost-staircase fashion, and the c orbitals display a clearer saw-tooth behavior, as shown in Fig. G.2(c). It is interesting to note how the zero-hybridization data, which in Fig. 6(c) travel multiple times along the same curve, here move along a set of shifted disconnected branches, each one corresponding to a f-electron plateau of Fig. G.2(b).

The data points in orange and red refer to two other sets of DMFT simulations run using an alternative procedure: instead of fixing the overall occupation, we required the converged solution to have a specific chemical potential, letting the occupation value freely adjust as a consequence. The orange data thus obtained are in agreement with a portion the positive-slope branches of the total filling curve in Fig. 6(a) of the main text. We can access a larger section of the fixed-ν curve (red data) by converging each μ-point and using the resulting self-energy as the starting point of the next simulation, in a decreasing μ direction. In both cases, however, the negative-slope branches of Fig. 6(a) remain out of reach.

Even including the geometric contribution, a small region of negative compressibility still persists in the range $\nu_f + \nu_c \in [0, \pm 1]$, as apparent from Fig. G.3, suggesting perhaps the tendency of the full TBLG system towards intrinsic (electronic) phase separation around ν values close to ± 0.6. A larger separation between the screened Coulomb interaction gates of the interaction Hamiltonian would however strech out the $\nu_f + \nu_c$ vs. μ curves further and stabilize the system eventually at all dopings.

Appendix H: Experimental data comparison

The experimental data of Fig.7 in the main text have been extracted from work by Zondiner et al. (in the following denoted as Z, [175]), Pierce et al. (P, [173]) and Saito et al. (S, [150]). In the two panels of the figure, the plotted quantities are related by derivative/integration. Hence, for each experimental source only one set of data has been considered, and the other has been numerically obtained. For Z, this is the chemical potential, while for P and S it is the inverse compressibility. An important point to notice is the difference between charge carrier density (denoted in Z and P as n) and filling factor ν, which is analogous to the one used in our work. The two are related via $\nu = n\Omega_0$, where Ω_0 is the area of the moiré unit cell, and depends on the twist angle θ via $\Omega_0 = 8\pi^2/3\sqrt{3}k_\theta^2$ where $k_\theta = 2|\mathbf{K}|\sin\theta/2$ and $\mathbf{K}$ is the Dirac point of one graphene layer. This conversion factor, dependent on the twist angle, has to be applied to data from Z (which provides μ as a function of n) and P (which provides $d\mu/dn$ as a function of ν). When the $\mu(\nu)$ data are obtained through integration, an offset given by the value $\mu(0)$ is subtracted.